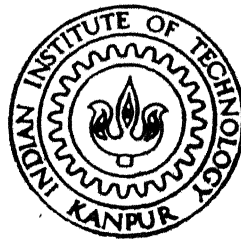# Processing and Characterization of AlN/Al base Composites via Directed Melt Nitridation

By

B S S DANIEL

DEPARTMENT OF MATERIALS AND METALLURGICAL ENGINEERING

INDIAN INSTITUTE OF TECHNOLOGY KANPUR

JULY, 1997

Processing and Characterization of AlN/Al base Composites via Directed Melt Nitridation

A Thesis Submitted

in Partial Fulfillment of the Requirements

for the Degree of

Doctor of Philosophy

by

B S S Daniel

to the

DEPARTMENT OF
MATERIALS AND METALLURGICAL ENGINEERING
INDIAN INSTITUTE OF TECHNOLOGY, KANPUR

July, 1997.
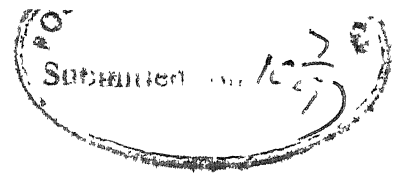
CERTIFICATE

This is to certify that the work contained in the thesis entitled **Processing and Characterization of AlN/Al base Composites via Directed Melt Nitridation** by B. S. S. Daniel, has been carried out under our supervision and that this work has not been submitted elsewhere for a degree.

Dr. V S R Murthy
Associate Professor
Dept. of Materials & Metallurgical Eng.
Indian Institute of Technology,
Kanpur.

Dr. G S Murty
Professor (Retd.)
Dept. of Materials & Metallurgical Eng.
Indian Institute of Technology,
Kanpur.

Date: July 10, 1997

Synopsis

The constant demand for materials with improved performance has led to the development of *in situ* composites. *In situ* composites embody a class of materials, wherein the reinforcement phase is formed within the parent phase by controlled melt growth, chemical reaction, transformation and/or deformation. This single stage process is cost effective and avoids additional steps such as sorting, alignment, pressure infiltration and sintering. Additionally, impressive mechanical properties are envisaged in some of these composites as reinforcements with clean matrix-reinforcement interface are produced within the matrix. The reaction based *in situ* composites are classified as liquid-gas (Directed Melt Oxidation and Nitridation), liquid-liquid (Sol-gel), liquid-solid (Reaction Metal Penetration), solid-gas (Reduction of Oxides) and solid-solid (Self-propagating High-temperature Synthesis, Reduction Reaction) reactions.

The present study concerns the processing and characterization of *in situ* composites based on liquid–gas reactions. The Directed Melt Nitridation process involves the reaction of an aluminum rich alloy in Nitrogen atmosphere to form an AlN/Al reaction product consisting of interpenetrated networks of Al and AlN. Additionally, when a porous ceramic preform is placed in conjunction with the molten alloy, the reaction product fills up the void space forming a nearly dense composite. For nitridation purposes, the aluminum alloy is placed in a recrystallized alumina crucible and heated above the liquidus temperature in a tubular furnace by maintaining very low Oxygen partial pressure in the reaction gas. For infiltration experiments, loose or sintered preforms were placed on top of the alloy billet. Spontaneous infiltration occurs when the preform material is wetted by the molten alloy. The infiltrated composites, after furnace cooling, were found to be nearly dense. Microstructural characterization was undertaken using X-ray, Optical microscopy, Scanning and Transmission electron microscopy techniques. Flexural strength and notch Fracture toughness were measured using a four-point loading fixture.

In the first phase of the experimental work, microstructural development in several binary and

ternary Al alloys was examined. Al rich binary alloys without Si, result in surface nitridation with the reaction essentially confined to the subsurface layer of the alloys. But with small additions of Si, the nitridation mechanism in Al-Mg alloys translates to a bulk nitridation forming an interconnected network structure of AlN and Al. Simple weight gain and TGA experiments carried out on various Si containing alloys indicate larger conversion to AlN in alloys containing higher Mg/Si ratio Further, the growth patterns observed can be divided into various stages. After an initial incubation period, when there is loss of volatile solute elements (indicated by formation of MgO on the crucible walls and furnace tube), black surface nitride is formed on the surface of the alloy. The alloy below wicks through micro-discontinuities of the AlN surface layer and small globules begin to form. As the process continues, the wicking dominates at various locations and small colonies of globules are formed. The micropore channels within these nodules are interconnected and fresh metal keeps coming through these capillaries sustaining the outward growth of the AlN/Al composite. The composite formation in Al-Si-Mg alloy is dependent on processing temperature At lower temperature (900^oC), only surface nitridation occurs. With increase in processing temperature (1000^oC), bulk nitridation occurs with the composite consisting of an interconnected network structure of AlN and Al. At still higher temperatures, nitridation dominates and AlN columnar crystal growth occurs. The liquid metal wicks through the pores to arrive at the surface. The AlN formation is also sensitive to solute atoms present in the alloy. While hexagonal AlN was found in several binary and ternary alloys, cubic nitride growth is reported in Al-Si-Mg-Zn alloys for the first time in the present study.

Though Al-0.5Si-8Mg alloy had the best nitridation characteristics, Al-2Si-8Mg alloy was selected for infiltration studies because of its consistency in infiltrating SiC preforms. Various SiC filler materials such as fibres, platelets and particulates were infiltrated to obtain SiC/AlN/Al composites. For comparison, AlN particulate reinforced AlN/Al composites were also produced. The surface chemistry of the filler material affects the wetting behaviour and has a greater influence on the infiltration process. Distinct heterogeneous nucleation of AlN is seen on Nicalon fibre. On the other hand, AVCO SiC monofilaments containing a surface carbon rich layer deter such nucleation.

The effect of temperature and particle size is investigated using SiC particulates. Infiltration experiments with three different SiC particle size ranges were performed at 1050^oC for 6 hours to study the sensitivity of particulate size on infiltration kinetics The infiltration rate improves with increase in minimum pore radius, which is in agreement with existing theoretical models. Secondly, the nitride formation rate is enhanced with increase in the mean preform particulate

surface area. This is because the particle surface offers sites for AlN nucleation. Lastly, larger shrinkage cavities (microporosities) are seen in coarse particulate reinforced composites due to large interparticle spacing, lower conversion to AlN and larger shrinkage within the bulk liquid.

To study the sensitivity of process temperature on infiltration kinetics, sintered SiC particulate preforms of different sizes were infiltrated in the temperature range of 950 to $1100^{o}C$. While the weight gain data exhibit higher AlN formation at higher temperatures, the porosity levels also increased with temperature. TGA studies in SiC preforms indicate higher weight gain compared to the base alloy. The activation energy for infiltration process was estimated to be $\sim$25 kJ/mol.

Maximum flexural strength and fracture toughness of 250 MPa and 7 $MPa\sqrt{m}$, respectively, are measured for SiC particulate reinforced composites. The property values decrease with increase in processing temperature due to enhanced porosity levels. The major drawbacks in SiC reinforced AlN/Al composites are the residual aluminum within the matrix and the interfacial reaction which forms moisture sensitive Al_4C_3. The former restricts the usage of these composites to temperatures below $500^{o}C$. By converting the residual aluminum to a high temperature phase, such as an intermetallic, the high-temperature limit of their application can be extended. To explore the conversion of residual Al to aluminide, Nickel aluminide powder preforms were infiltrated in the temperature range 750–$1050^{o}C$ and the resultant microstructures were analysed. A higher conversion of Al to AlN was observed at all temperatures compared to SiC particulate infiltration. At lower processing temperatures ($750^{o}C$), Ni_2Al_3 phase is retained and finer AlN crystals are present throughout the matrix, whereas at higher temperatures ($>950^{o}C$), Ni_2Al_3 phase is completely consumed by dissolution and reprecipitation of $NiAl_3$ occurs. The mechanical properties of intermetallic reinforced composites improve with decrease in processing temperature due to retention of Ni_2Al_3 phase. Maximum flexural strength and fracture toughness of 255 MPa and 10.4 $MPa\sqrt{m}$, respectively, were measured for composites processed at $750^{o}C$. Finally, various possibilities to prevent formation of moisture sensitive Al_4C_3 via interfacial reaction are discussed AlN or Si_3N_4 coating through precursor route are suggested to be a possible solution.

The composite growth in preform is modelled based on the fluid flow phenomenon. Previous modelling efforts for the liquid metal infiltration through porous preforms were based on a *flow through bundle of capillary tubes* phenomenon. In contrast, for the first time, a *flow through porous-bed* approach combining Navier-Stoke's and Darcy's equations has been attempted in the present study. To this end, a transient, 2-dimensional, laminar flow model in cylindrical coordinate system has been developed.

Three different modelling approaches based on an implicit scheme were considered to predict the flow behaviour within the liquid metal reservoir and porous preform. These are: (1) Enhanced viscosity model, (2) Superimposed porous media model and (3) Modified momentum model. For an enhanced viscosity value of 12 Poise within the preform domain, Model 1 could accurately predict the infiltration rate during the early stages of composite growth, whereas Model 2 resulted in an overestimate of infiltration heights beyond $2000s$ Of the three modelling approaches considered, Model 3 was preferred due to its faster convergence and relative numerical stability. The permeability of the preform was estimated to be $\sim 7\times10^{12}m^2$ for the present experimental conditions.

To validate the model, the sensitivity of infiltration height predictions to various numerical approximations such as, depth immersed in liquid, grid size distribution and the time step were tested computationally. After establishing the reliability of the model, the sensitivity of predicted results to process parameters were also examined. Infiltration through preforms of three different packing fractions and particulate size were numerically computed. The trend in computed results are in accordance with experimental observations and predictions of the capillary bundle model. The numerically predicted activation energy of 18 kJ/mol for a surface tension force dominated system is consistent with the experimentally obtained value.

In summary, the nitridation characteristics in several aluminum rich alloys was studied under various processing conditions. Temperature and Mg/Si ratio are effective variables to control nitridation kinetics. Various forms of SiC reinforced AlN/Al composites were developed using Al-2Si-8Mg alloy as the infiltrant. While the nitride formation and infiltration kinetics improve with increasing SiC particle size and temperature, the mechanical properties show a decreasing trend. Nickel aluminide reinforced AlN/Al composites were processed at temperatures as low as 750^oC. The intermetallic reactions are diffusion controlled at low temperatures, but follow a dissolution-reprecipitation mechanism at temperatures above the peritectic. Improved mechanical properties are attained at low processing temperatures due to retention of high temperature phase and particle morphology. Finally, a mathematical model based on flow through porous-bed phenomenon was developed to predict composite growth rate. The model predictions are consistent with experimental observations for variation in particle size and preform packing fraction.

Acknowledgement

to Cuckoo

Contents

Results and Discussion

List of Figures

List of Tables

Chapter 1

Introduction

The constant endeavour to produce materials with specific combinations of properties has exhausted the capability of conventional materials. Moreover, with rapid advance in several technological areas, there is an increased demand for materials of improved performance. In the quest to satisfy this demand, different classes of materials have been developed. Composite materials represent a separate category of materials, bringing together often extreme, but desired properties. Generally, a *composite* is defined as a material consisting of two or more physically and/or chemically distinct, suitably arranged or distributed phases with a separating interface, whose characteristics are not depicted by any of the components in isolation [1][1]. Palm leaf, wood and bone are some of the naturally occurring composites, where flexibility and strength are perfectly balanced. In recent times, man-made composites are found in everyday use. Some common examples are reinforced concrete, steel reinforced rubber tyre, glass fibre reinforced plastic, etc.

Generally, composite materials constitute a continuous matrix phase and a reinforcement phase. The reinforcement can be in the form of fibres, whiskers, platelets or particulates. Depending on the matrix phase, composites are classified as Polymer matrix composites (PMCs), Metal matrix composites (MMCs), Ceramic matrix composites (CMCs) and Intermetallic matrix composites (IMCs). Examples of composites formed by combining different materials are illustrated in Figure 1.1. A wide variation in properties can be achieved by

---

[1]references listed at the end of each chapter

controlling the proportion of the phases and their distribution during processing. Currently, in processing of composite materials, synthesis is the key step, where different phases are combined to develop a spectrum of new materials with a wide range of properties. The focus of this thesis is on processing of composites which are in the domain of MMC and CMC materials.
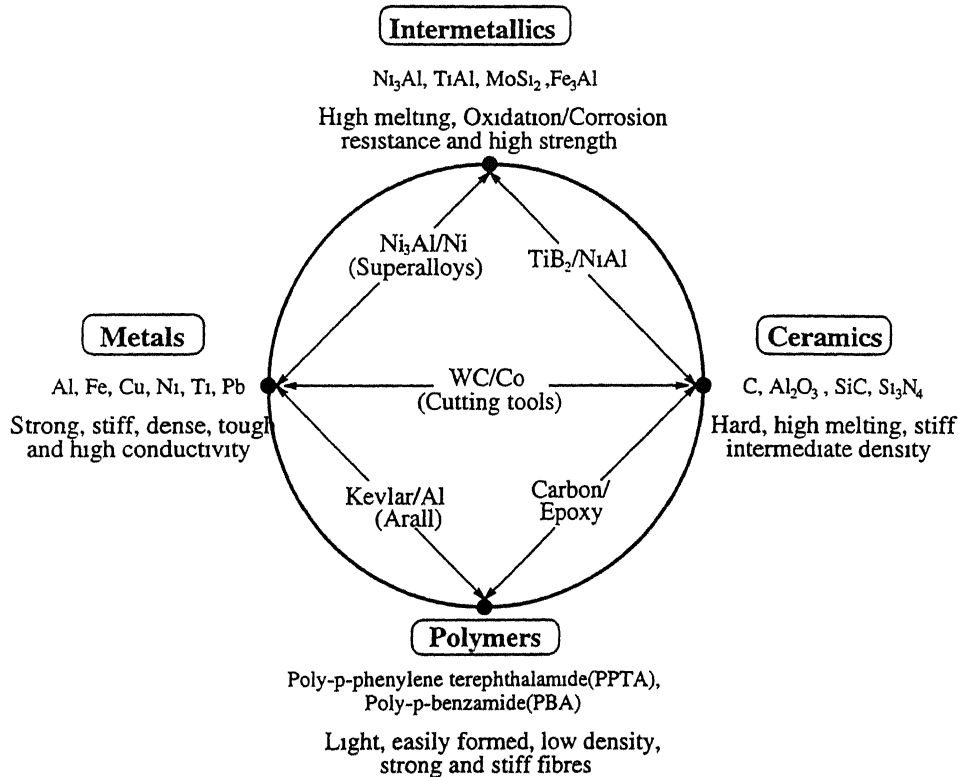
Figure 1.1: A representative figure showing different classes of materials with examples of composites formed thereof.

The most common CMC processing routes are Hot Pressing and Hot Isostatic Pressing (HIP) [2]. They are expensive because of the high temperature and pressure needed to consolidate ceramic powders. An optimization of temperature and pressure is required to eliminate porosity, fibre damage and interfacial reactions. Alternatively, Chemical Vapour Infiltration (CVI) or Chemical Vapour Deposition (CVD) are used to infiltrate porous preforms [2]. In these processes. a solid material is deposited from gaseous reactants onto a heated substrate (preform) under isothermal conditions. In the case of CVI, a temperature and/or pressure gradient is applied to improve the deposition rate. The drawbacks in these methods are: slow processing rate, high cost and residual porosity. Additional ceramic processing routes

which can be modified to produce CMCs are Sol-gel synthesis and Self-propagating High-temperature Synthesis (SHS). These processes will be discussed in the following chapter.

MMCs are conventionally produced by solid-state or liquid-state processing routes. Among the former, Powder Metallurgy techniques are commonly used to produce composites with particulate, whisker or fibre reinforcements. Metal powder and reinforcements are blended together, and sintered to attain theoretical density of the matrix. Alternatively, MMCs can be produced by Plasma Spray, Chemical or Physical Vapour Deposition followed by Hot Pressing/HIPing [3,4]. Among the liquid state MMC fabrication methods, Vortex method, Rheocasting and Squeeze casting are prominent [5]. Rheocasting (or Compocasting) involves the addition of particulate or whisker reinforcements into a semi-solid metal in the agitated state. Continuous agitation breaks down the solidifying dendrites into fine spheroidal particles. The composite mixture with relatively low viscosity can then be cast into a single billet (Rheocasting). Alternatively, the semisolid mixture can be reheated above the liquidus and die cast along with the reinforcements to near-net shape (Compocasting). On the other hand, a larger fraction of reinforcement can be incorporated *via* Squeeze Casting. In this process, a porous preform is placed in a preheated die, into which molten metal is forced by a hydraulic press.

The conventional composite processing techniques involve several expensive processing steps. Economic considerations have restricted their use to high performance applications, where cost is not the primary concern. *In situ Composite* is a term applied to a relatively small, but fast growing category of materials, wherein the reinforcing phase is formed within the parent phase by controlled melt growth, chemical reaction, transformation and/or deformation. Composite manufacturing *via in situ* process is confined to the thermodynamic and kinetic space, through control of composition and process variables to arrive at duplex or multiphase structures. This single stage synthesis route has considerable advantage over conventional processes described earlier. Complicated additional steps, such as sorting, alignment, pressure infiltration and sintering are eliminated. Hence, these composites are cost effective. In addition, strengths of some of these composites are better, because an impurity free reinforcement with clean matrix-reinforcement interface is produced within the

parent phase.

The term *in situ* with reference to composites was first used to describe directionally so-lidified alloys. Controlled heat flow during solidification in certain binary alloys results in extended directionality of the microconstituents to give impressive mechanical properties. Many eutectic and monotectic systems offer such aligned, faceted or non-faceted two phase structures [6, 7]. The last ten years have seen the advent of many novel *in situ* processes, which are developed to meet specific property requirements. Several of these new materials have the potential to replace conventional materials. The processing, properties and process modelling of one such process, namely Directed Melt Nitridation and Infiltration through porous ceramic preforms is examined in this thesis. The process involves the reaction of an aluminum alloy in Nitrogen atmosphere to form an AlN/Al reaction product. Additionally, when a porous ceramic preform is placed in conjunction with the molten alloy, the reaction product fills up the void space, forming a nearly dense composite.

In the present work, various aluminum rich alloys are examined to optimize their nitridation and infiltration characteristics. Using the selected alloy, the influence of various processing variables on infiltration through porous ceramic (SiC, AlN) and intermetallic (Nickel alu-minide) preforms are studied. Lastly, a mathematical model is developed to simulate the infiltration phenomena and predict the composite growth. The organization of the thesis is as follows. Following this introductory chapter, a literature review on *in situ* composites is presented in chapter 2. The review consists of the processing and properties of *in situ* processed composites, with special reference to pressureless, reactive infiltration in Nitro-gen and Oxygen atmospheres. Models for the strengthening and toughening mechanisms in such metal–ceramic composites are also described. Chapter 3 illustrates the experimental procedures concerning the aluminum alloy nitridation and preform infiltration in Nitrogen atmosphere. The microstructural and mechanical property characterization techniques em-ployed are described. The results of nitridation kinetics of various aluminum rich binary and Si containing complex alloys are presented in chapter 4. In chapter 5, the results of infiltration into SiC, AlN and nickel aluminide preforms under various processing conditions are elucidated. These results are discussed in the light of processing parameters, microstruc-

tural development and mechanical property variations. Chapter 6 consists of a mathematical model developed based on flow through porous-bed phenomena, to predict the infiltration kinetics in terms of the processing variables experimentally studied in chapter 5. Chapter 7 consists of the conclusions arising from the present work. Finally, in chapter 8 the scope for further work is presented.

References

[1] K. K. Chawla, *Composite Materials: Science and Engineering*, Springer-Verlag, New York, U.S.A. (1987) 5.

[2] K. K. Chawla, *Ceramic Matrix Composites*, University Press, Cambridge, U.K. (1993).

[3] R. K. Everett, Deposition Technologies for MMC Fabrication, In *Metal Matrix Composites: Processing and Interfaces*, ed. R. K. Everett and R. J. Arsenault, Academic Press, San Diego, U.S.A. (1991) 103–119.

[4] S. Suresh, A. Mortensen and N. Needleman, *Fundamentals of Metal Matrix Composites*, Butterworth-Heinemaann, MA, U.S.A. (1993).

[5] R. B. Bhagat, Casting Fibre-reinforced Metal Matrix Composites, In *Metal Matrix Composites: Processing and Interfaces*, Ed. R. K. Everett and R. J. Arsenault, Academic Press, San Diego, U.S.A. (1991) 43–82.

[6] F. D. Lemkey, Advanced insitu composites, In *Industrial Materials Science & Engineering*, ed. L. E. Murr, Dekker, New York, U.S.A. (1984) 441–469.

[7] F. D. Lemkey and S. G. Fishman, Insitu composites: Fabrication, In *Concise Encyclopedia of Composite Materials*, ed. A. Kelly, Pergamon press, Oxford, U.K. (1989) 147–150.

Chapter 2

In situ Composites

2.1   Introduction

To overcome some of the inherent problems associated with conventional materials processing, several *in situ* methods have been developed to obtain metal/ceramic composite materials. In this chapter, recently developed processes are reviewed with special emphasis on directed melt oxidation and nitridation. Composites processed *via in situ* methods offer microstructures with varying metal/ceramic combinations. In some processes, metal matrix composites dispersed with controlled quantities of ceramic phase(s) are possible; whereas in others, ceramic composites with isolated/interconnected metallic dispersions are obtained. Further, the volume fraction and distribution of the phases could be tailored to specific property requirements by controlling the processing variables, namely processing temperature, time, reactant phases and filler materials. The properties of *in situ* processed materials primarily depend on the matrix and the volume fraction of the dispersed phase. In the later part of this chapter, the mechanical properties, strengthening and toughening mechanisms and potential applications of *in situ* processed composites are also presented.

2.2 Synthesis of *In situ* Composites

The first directionally solidified *in situ* composites were non-structural in application [1,2], but later the process was proven to be successful in the development of new materials that replaced conventional superalloys [3,4]. The principal motivation was to control the grain morphology (low boundary energy) and texture with a preferred crystallographic orientation parallel to the direction of solidification [5–7]. Thompson *et al.* [8], while studying the directional solidification of Co-Cr-C monovariant eutectic alloys, reported that the hexagonal $(Cr,Co)_7C_3$ fibrous carbide phase grows in the [0001] direction and the Co-Cr solid-solution matrix has its [211] axis aligned to the growth direction. Further, the interfaces produced in these materials have strong and stable bonding which cannot be easily achieved in other synthetic composites. Additionally, they offer high-temperature strength and excellent creep resistance [9–11]. Over the years, directional solidification has evolved into a viable commercial process leading to substantial advances in component performance.

In materials where controlled solidification is not feasible, there are other methods to develop composite microstructures. If the alloy contains two ductile phases, they can initially be produced by casting or powder metallurgy technique, and subsequently deformed by mechanical means (e.g. swaging, extrusion, rolling or drawing) to obtain filamentary type composites with exceptionally high strength [12–15]. This family of materials are now commonly known as Heavily Deformed Insitu Composites (HDISC). A number of alloys, such as Ag–Cu, Ag–Ni, Cu–Cr, Cu–Fe, Cu–Ta and Cu-Mo are processed by subjecting them to extensive deformation. Nb_3Sn/Cu composites used for superconductor solenoids are processed using HDISC technique. Similarly, Nb–Ti/Cu alloys processed by 'bundle and draw' technique are used in high-speed trains, Nuclear Magnetic Resonance (NMR) and Magnetic Resonance Imaging (MRI) systems. The properties and strengthening mechanisms of various *deformed* composites are summarized by Courtney [16]. Although the property improvement in HDISC materials is substantial, the process is yet to be fully exploited for commercial applications.

Another approach for producing high-strength *in situ* composites is based on the principle

of *dispersion strengthening*. In this case, the metal matrix is strengthened by a fine (10–100 *nm*) dispersion of second phase particles such as oxides, carbides or intermetallics. Particulate dispersion can be achieved by a number of ways, namely surface oxidation of ultrafine powder followed by compaction, sintering and extrusion of fine powders, mechanical alloying, co-precipitation, internal oxidation, decomposition of inorganic compounds and electrolytic methods [17–21]. The strengthening mechanisms of dispersion hardened alloys are similar to that of conventional precipitation hardened alloys in the over-aged condition. The dispersoids hinder the movement of dislocation. The strength enhancement due to interaction between the particles and dislocations was earlier explained by Orowan [22] and Martin [23]. Additional strengthening arising from grain size refinement (Hall-Petch strengthening) also contributes to the overall property improvement. Contrarily, at higher temperatures, grain growth may have the opposite effect. Moreover, thermal energy aids the climb of dislocations over particles providing additional freedom of motion to the dislocations. Several models have been proposed to explain the climb of dislocations over dispersoids and relate the phenomenon to the observed mechanical properties [24–29].
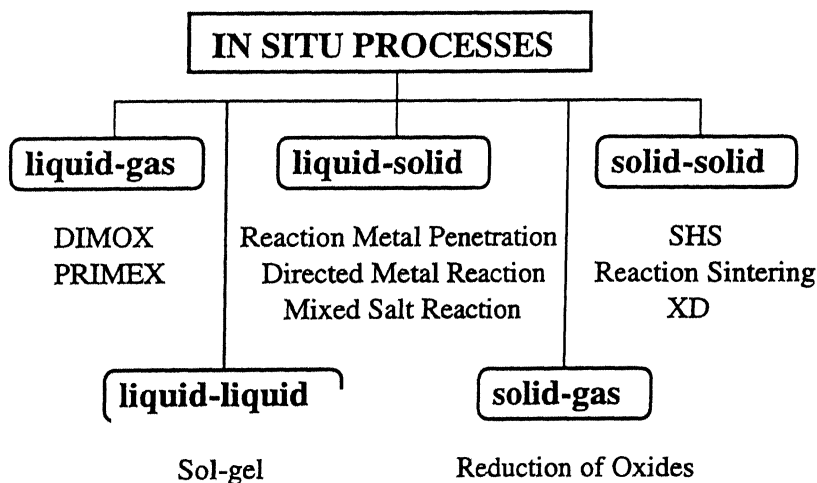
Figure 2.1: Composite processing *via in situ* methods.

The earlier described processes are based on either deformation or controlled solidification to acquire desired phases. Several processes have been developed in the recent past which involve selective *in situ* reactions to form ceramic/metallic phase(s) within the parent matrix. Many of these processes are yet to find commercial application and are still in developmental

stages in various laboratories. In the following sections, the processing and properties of recently developed *in situ* composites are reviewed. For the sake of clarity, the processing methods are classified based on the reactant phases, namely liquid–gas, liquid–liquid, liquid–solid, solid–gas and solid–solid reactions (Figure 2.1).

2.2.1   Liquid-gas reactions

(a) Blowing of reactive gases into liquid melts

An economical way of synthesizing metal-ceramic composites is by bubbling the reaction gas into molten metal, containing various reactive elements. Fine dispersoids of thermo-dynamically stable refractory compounds are produced by the direct interaction between the liquid metal (with alloying elements) and the gaseous species. The matrix is usually a non-ferrous metal, such as Al, Cu, Mg, Ni or Ti, while the reinforcement phase could be carbides, nitrides or a good admixture of both. Since the reaction takes place *in situ* at a pre-determined temperature, the reinforcement phase is chemically clean and the interface is beneficial from mechanical property viewpoint. The final microstructure consists of fine dispersoids of ceramic phase in a metal matrix. Some examples are:

1. Al-Ti(l) or Al-Si(l) reacts with carbon (from a gas) to form thermodynamically stable (e.g. SiC) or unstable carbides (e.g. Al_4C_3).

2. Ti-Al(l) reacts with Nitrogen to precipitate one or more nitrides (e.g. TiN, AlN) within the matrix.

3. Controlled melt reaction of Al-Ti(l) with ammonia-methane gas mixture to arrive at mixed carbide/nitride phases, e.g. (TiC+AlN), Ti(CN)+Al(CN).

The main advantage of the process is its amenability to continuous casting and to near net shape manufacturing [30, 31]. However, the the process has the following drawbacks: (i) the volume fraction of the reinforcing phase is low and limited to only those systems that react rapidly with the gaseous species, (ii) the dispersoids tend to segregate and (iii) high

temperatures are required to enhance kinetics. Literature on this topic is available in the form of reports or patents [32]. However, no information is available on the commercial success of this process.

(b) Directed melt oxidation (DIMOX) process

(i) Principle of controlled oxidation

When pure aluminum is oxidized, a thin oxide (γ-Al_2O_3) layer forms on the surface which effectively prevents further oxidation of the underlying metal. The oxidation behaviour of pure aluminum drastically changes with small additions of volatile elements, such as Mg, Zn and Li. Such microstructural changes in the case of Al-Mg alloys were extensively studied [33–37]. Cochran *et al.* [37] examined the oxidation kinetics by varying the atmosphere and reported continuous oxidation of the alloy (termed as *break-away oxidation*) with increment in temperature as well as Mg concentration of the alloy. Similarly, Zn addition delayed Al_2O_3 nucleation and promoted the pore formation in the surface oxide. Earlier, some of these investigations were carried out with an intent to suppress oxidation during melting or heat-treatment. After a decade or so, resurgence of the same break-away oxidation process from another viewpoint led to the development of a novel process for the production of metal/ceramic matrix composites. In this technique, Mg (or other volatile species which form a non-protective oxide) containing aluminum alloy is treated at high temperatures (much above the liquidus) to give rise to interconnected and interpenetrating Al_2O_3/Al composite structures. This *in situ* synthesis route developed by Lanxide Corporation, USA is currently known as Directed Metal Oxidation (DIMOX) process [38–40].

The directed metal oxidation of aluminum alloys involves the reaction of a bulk molten alloy with a gaseous oxidant to produce a solid body via a directed growth process. The reaction product forms initially on the exposed surface of a pool of molten alloy and then grows outward by *wicking* of additional metal through the ceramic product of the oxidation reaction (Figure 2.2). The resulting microstructural constituents are three dimensionally interconnected and are different from conventionally processed powder metallurgy products. The
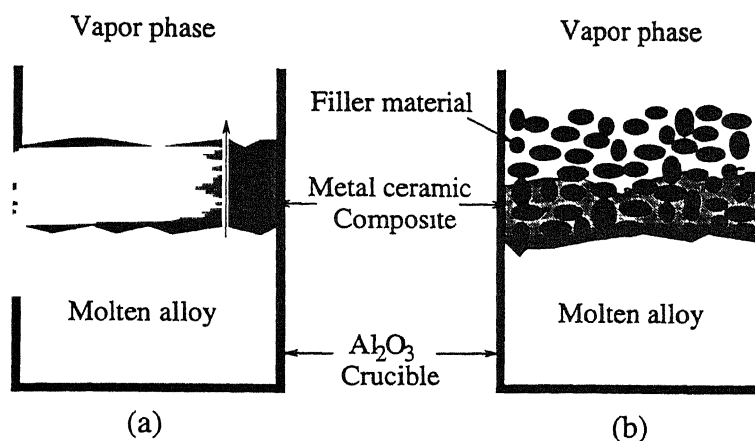
Figure 2.2: Schematic of the outward growth of metal/ceramic reaction product (a) into free space and (b) through filler material

residual metal content in the composite can be varied by altering the processing conditions and the composition of the base alloy. These metal containing composites are expected to have good stiffness, fracture toughness, thermal shock resistance and excellent wear resistance. The potential advantages of DIMOX process are its simplicity, low processing cost, flexibility in filler material selection, near net shapes and desired mechanical properties by tailoring the microstructure. Currently, the process is being successfully used to produce a number of engineering components [40–43]. The same process can be modified by placing filler materials (e.g. fibres, whiskers, particulates, platelets, etc.) in the path of the outward growing oxidation product to obtain 'multiphase' materials with a wide range of properties [44, 45]. A schematic diagram of the crucible configuration with and without preform is shown in Figure 2.2. Some examples of multiphase composites obtained *via* infiltration are Al_2O_3/Al, $SiC/Al_2O_3/Al$, etc. However, the condition for favourable infiltration is that the filler material must be compatible with the oxidizing atmosphere at the processing temperature and that the filler material must be wetted by the alloy. The infiltration process is discussed in greater detail in the subsequent sections.

(ii) Process variables

Several investigators have examined various aspects of directed melt oxidation in binary, ternary and even in complex alloys [46–53]. From these studies, it is evident that addition

of volatile solute elements, such as Mg, Na, Li and Zn, singularly or in combination (up to 10 $wt.\%$) are essential for continuous growth of the composite. These elements primarily alter the wettability of the liquid alloy besides forming a thermodynamically unstable, non-protective surface oxide layer. Further, these elements diffuse at a rapid rate to form an oxide on the surface and dissociate under specific conditions during the process. In addition to volatile solute atoms, other elements, such as Si, Ge, Sn and Pb (group IVB elements) may also be added to control the reaction kinetics and wettability [54]. These elements could be introduced externally in the form of elemental or oxide powders to accelerate the oxidation process [37, 46, 52, 55–57]. Moreover, the external surface oxide dopants reduce initial incubation period.

In addition to chemistry of the melt, growth rates are also controlled by oxidation temperature, process duration, and to a certain extent by the partial pressure of Oxygen. Oxidation temperatures below 950^oC result in selective conversion of Mg to MgO or $MgAl_2O_4$; whereas temperatures above 1400^oC lead to the formation of a porous material. Hence, the processing temperature is restricted between $1000–1350^oC$ when Mg additions are made. However, the temperature range changes marginally depending on the type and concentration of solute atoms. Similarly, the residual metal volume fraction was shown to decrease with increasing holding time [43]. Further, many investigators have suggested that the growth rates are sensitive to the partial pressure of Oxygen [51, 53]. Nagelberg [49] cited a $(p_{O_2})^{1/4}$ dependence for the oxidation of Al-10Si-3Mg alloy where a normalized weight gain of 0.2 g/cm^2 was reported. Contrarily, no significant influence of Oxygen partial pressure was observed in the case of a more complex alloy (Al-8.8Si-2.8Zn-3.1Cu-1.1Fe-0.25Mg) [46].

(iii) Thermogravimetric studies on the oxidation of different alloys

Thermogravimetric analysis (TGA) was performed on various alloys to understand the growth kinetics. A typical TGA curve of an Al–Si–Mg alloy oxidized at 1250^oC is shown in Figure 2.3. The general features for Al–Mg and Al–Si–Mg alloys are essentially the same except that the incubation period is noticeably shorter in the later case. The oxidation process can be divided into four distinct stages. Initially, during the incubation period, there is
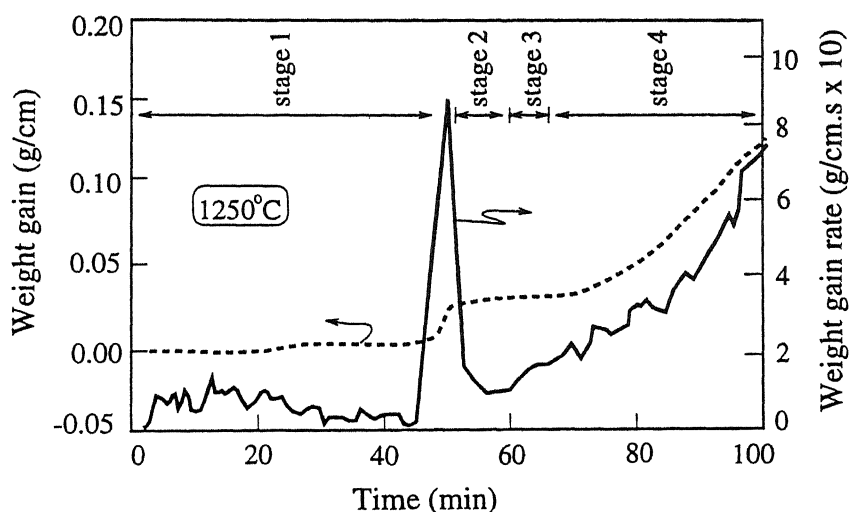
Figure 2.3: TGA analysis of Al-2Mg-10Si alloy showing various stages of oxidation[51].

little or no weight change (stage 1). As the process continues, a sharp momentary increment in weight is noticed (stage 2), followed by a steady state where a continuous increase in weight is observed (stage 3). Finally, saturation is reached when little or no further weight gain occurs (stage 4). The small weight loss observed in some alloys during the initial incubation period is attributed to the rapid vapourization of Mg [53]. Subsequently, the sharp weight gain in stage 2 is due to the formation of spinel ($MgAl_2O_4$) layer on the surface. The oxidation rate decreases to a minimum (0.03–0.05 g/cm^2) following the spinel formation, which is indicative of the thickening of the duplex layer [51]. After approximately 10 hours (depending on the alloy and temperature), a gradual increase in weight is observed, when an uninterrupted growth of Al_2O_3 takes place. Finally, the curve drops due to the exhaustion of the liquid metal in the reservoir as well as in the micro-channels.

The activation energy for composite growth calculated for different alloys vary from 89–400 kJ/mol, depending on the composition of the alloy (Table 2.1). Typical growth rates reported in the literature are in the range of 5–8 mm/day, with maximum rates as high as 30 mm/day [40].

Table 2.1: Activation energies of oxidation for different alloys.

Author	Alloy composition (wt.%)	Activation energy (kJ/mol)
Jayaram [39]	Al–Mg	180-400
Nagelberg [46]	Al-8.8Si-2.8Zn-3.1Cu-1.1Fe-0.25Mg	89
Nagelberg et al. [50]	Al-10Si-3Mg + trace Fe	370
Vlach et al. [53]	Al-2.85Mg-5.4Si	270
Dhandapani et al. [63]	Al-10Si-3Zn-1Mg with SiC particulates	258

(iv) Composite growth reaction mechanism

During the initial period, when the liquid alloy is heated to elevated temperatures, a dull gray *non-protective* MgO layer is formed on the surface (Figure 2.4). This layer undergoes microcracking and buckling due to stresses generated by volumetric expansion. At the same time, the underlying aluminum reacts with MgO to form $MgAl_2O_4$ below the MgO layer formed earlier. The spinel layer begins to coarsen with time, as the oxidation progresses. It is porous and contains interconnected micro-channels containing metal. Salas *et al.* [52] have indicated that the formation and coarsening of channels is due to: (i) some form of morphological instability at the spinal/metal interface or (ii) entrapment of liquid metal in a fast moving oxidation front in the early stages of oxidation. The faster diffusion of Mg^{2+} relative to Al^{3+} through the spinal layer causes MgO to continuously form on the surface. In the initial stages, the oxidation event is completely dominated by the formation and growth of the duplex layer ($MgO+MgAl_2O_4$). The details of spinel layer formation were reported by several investigators [50–53].

In the next stage, the liquid metal from the alloy reservoir wicks through the micro-discontinuities of the duplex layer and emerges as small nodules on the surface of MgO (Figure 2.4). Mg in the liquid alloy is believed to aid the wicking process by modifying the wetting characteristics of the alloy. As the alloy climbs to the surface, it gets oxidized and once again the duplex layer covers the nodules. Such nodules nucleated from the surface layer

(1) Duplex layer formation

(2) Wicking through the Duplex layer

(3) Planar front formation and initiation of Al_2O_3 in nodules

(4) Bulk growth of Al_2O_3/Al and dissociation of underneath Oxides

$$MgO \longrightarrow Mg^{2+} + 2\bar{e} + \underline{O}$$
$$MgAl_2O_4 \longrightarrow Mg^{2+} + 2Al^{3+} + 8\bar{e} + 4\underline{O}$$
(under Oxygen partial pressure gradient)
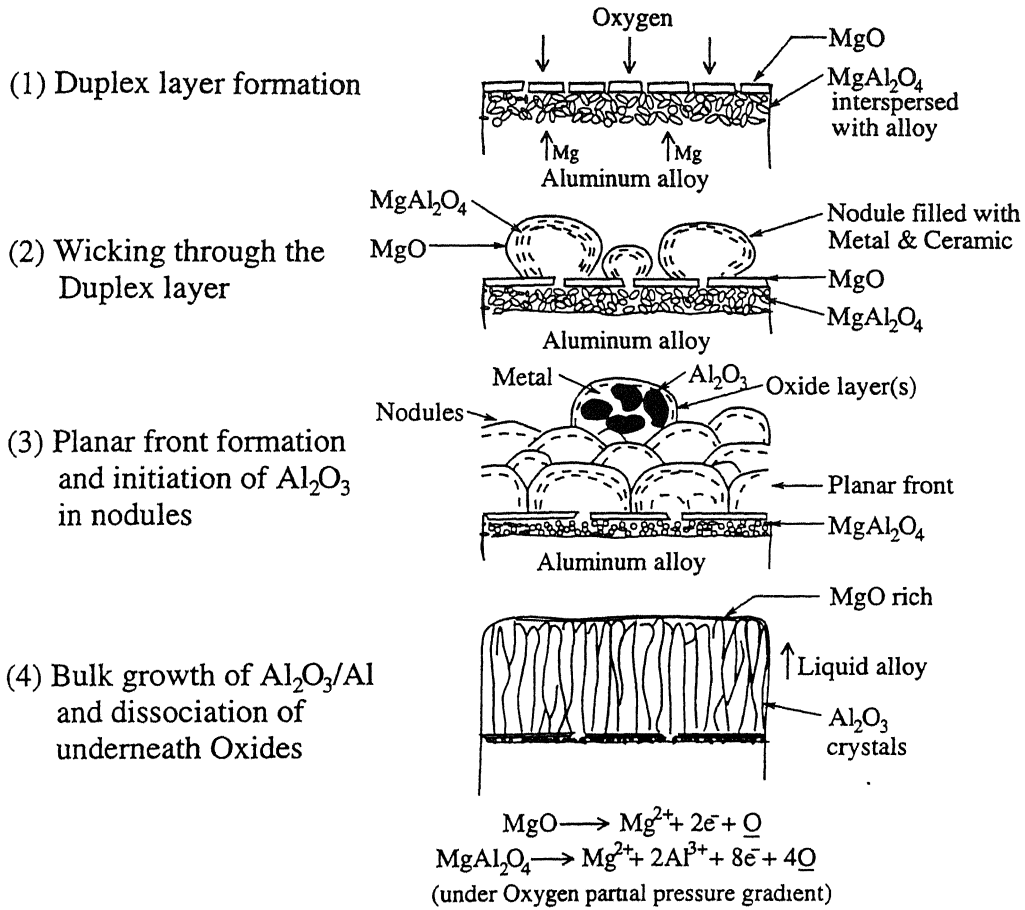
Figure 2.4: Schematic diagram illustrating the various surface microstructural changes occurring during oxidation of Al–Mg and Al–Si–Mg alloys.

eventually coalesce to form a 'cauliflower' type of colony and several such colonies join to develop a planar growth front. The liquid in the nodules maintain contact with the alloy reservoir and further wicking continues uninhibitedly to feed metal to the reaction interface.

The most interesting microstructural development in DIMOX process is the transition from $MgAl_2O_4$ formation to Al_2O_3. For the initiation of Al_2O_3 formation, Mg concentration in the liquid alloy is critical. When Mg concentration in the alloy shifts to the (Al,Mg) + Al_2O_3 + $MgAl_2O_4$ tertiary phase field in the Al-Mg-O ternary diagram, Al_2O_3 nucleation occurs. But a duplex layer continues to exist on the surface of the nodules [47]. It is estimated that when the Mg concentration drops below 0.3 *wt.%*, Al_2O_3 formation completely dominates the growth. At this stage, only a thin layer of MgO is seen at the oxidation front (Figure 2.4) [51,52]. Although Al_2O_3 appears isolated in a cross-section, it is interconnected

three dimensionally and grows continuously for several tens of microns due to constant supply of liquid alloy and Oxygen [47,49]. Back reflection X-ray and TEM studies documented that α-Al_2O_3 grows epitaxially, parallel to its c-axis of Al_2O_3, consisting of a large number of low angle grain boundaries [46,52,58]. However, no crystallographic orientation was detected in the metallic phase. Based on TGA runs carried out in Argon/air, Debroy *et al.* [59] are of the opinion that the wicking process is not rate controlling for the growth of Al_2O_3. They concluded that the rate of oxidation is influenced by the rate of transport of ions through the oxide matrix.

The bulk growth of such Al_2O_3/Al generates an Oxygen gradient across the underneath composite layers (MgO + $MgAl_2O_4$), which dissociate to give Mg^{2+}, Al^{3+} and O^{2-} ions. Mg^{2+} ions diffuse towards the surface and help in maintaining a non-protective MgO layer on the surface, whereas Al^{3+} and O^{2-} contribute to the growth of Al_2O_3 in the bulk composite [51,52,60]. A similar sequence of microstructural features was reported in Al-Zn and Al-Mg-Zn alloys [47,49], although there were some differences in the morphology of oxide formed, diffusion and dissociation rates of the elemental species.

(c) Al_2O_3/Al growth into ceramic preforms

A direct extension of the DIMOX process is the directed melt infiltration (DMI). Herein, the Al_2O_3/Al reaction product is grown into cavities of a porous preform [38,44]. The oxidation growth is restricted or channeled within the cavities of the filler material resulting in near net-shape, avoiding expensive composite machining to a large extent. The preforms used are made to the shape of the final product, using ceramic particulates, whiskers or fibres. Loose powder or fibre preform can also be used, and the shape obtained is roughly that of the container within which the composite growth is restricted. Reinforcement varying between 30–80 *vol.%* is feasible. Thus, a wide range of 'multiphase' materials with tailored mechanical properties can be processed using different volume fractions of various types of fillers. The literature search reveals that SiC and Al_2O_3 particulates are commonly used as filler material, while infiltration was also possible in a number of other oxide and non-oxide

systems [38,42,44,61]. Some examples of preform/alloy combinations, and their growth rates are given in Table 2.2.

Table 2.2: Growth rates for different alloy and preform combinations.

Authors	Alloy composition (*wt.%*)	Preform material	Growth rate
Newkirk *et al.* [38]	Al–Mg + (Si, Ge, Sn & Pb)	Al_2O_3, SiC, $BaTiO_3$	2.5–3.8 *cm/day*
Manor *et al.* [45]	Al-5.1Zn-0.17Mg-9.1Si-3.2Cu-1.1Fe-0.23Mn-0.08Ni-0.05Sn	SiC	16 $\mu g/cm^2/s$
Pickard *et al.* [157]	Al-3.5Cu-8.5Si-1.3Fe-3.0Zn-0.1Mg	SiC	–
Muralidhar *et al.* [64]	Al-5Zn(0.3Mg)	Al_2O_3	5 $\mu g/cm^2/s$
Dhandapani *et al.* [63]	Al-10Si-3Zn-1Mg	SiC	3–6 $\mu g/cm^2/s$

The criteria for selecting a filler material are as follows. Firstly, the alloy should necessarily wet the preform material, i.e. a low contact angle ($>90^o$) is essential. Few selected preform/alloy combinations exhibit favourable response. The wetting characteristics are generally improved by alloying with volatile species, *viz* Mg, Zn, Li, etc. Further, these solute atoms form an oxide coating on the surface of preform particles and modify the wetting behaviour. Secondly, preform material should be compatible with the alloy and the reaction atmosphere (in this case Oxygen). A limited reaction (reactive infiltration) between the preform and liquid alloys is desirable to increase the infiltration rates. However, such interfacial interactions should not be detrimental in achieving optimum mechanical response. In extreme cases, where the interfacial reaction is intense, alloy modification, barrier coatings or both become necessary. For instance, Nicalon SiC fibre preforms are coated with a protective layer to prevent surface oxidation and alloy-fibre reactions [44].

The microstructural features of infiltrated Al_2O_3/Al composites are similar to the composites obtained by directed melt oxidation of various aluminum alloys. However, reinforcements tend to refine the microstructure to a certain degree and the relative proportion of Al_2O_3/Al content varies marginally (Figure 2.5). The microstructures can be further refined by additives, such as Ni [45,62]. Composites with filler material exhibited higher weight gain rates, indicating enhanced growth rates compared to the base alloy. Also, oxidation rates were
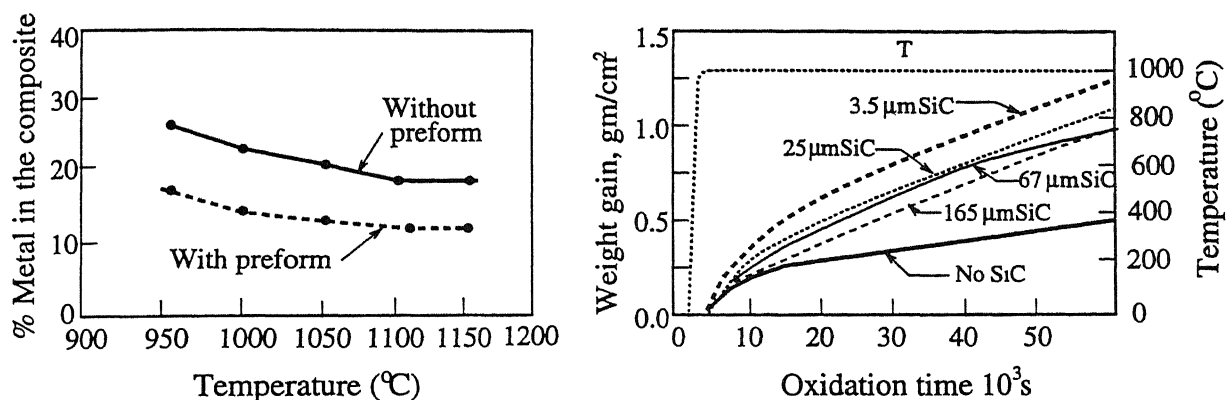
Figure 2.5: (a) Volume fraction of metal retained in composites processed at various temperatures, with and without preform. (b) Weight gain plot for SiC preforms of different particle size. ($T=1000^\circ C$)[45]

found to increase with decreasing particle size [45,63]. Manor *et al.* [45] suggested that the increment is at least by a factor of two. This is attributed to the decrease in free energy at the liquid alloy/preform interface due to vapour phase deposition of oxide layers ahead of the oxidation front. In alloys, such as Al-5.1Zn-0.17Mg-9.1Si-3.2Cu-1.1Fe-0.23Mn-0.08Ni-0.05Sn, although very high infiltration rates could be achieved, segregation of Fe and Si rich phases and brittle intermetallics undermined the overall toughness of the composite.

As the liquid climbs through the preform, occasionally the oxidation front is blocked, resulting in large size pores (macro-porosity); whereas local solidification shrinkage of metal in Al_2O_3/Al composite results in microporosity. The porosity was claimed to increase with Mg content in the alloy, oxidation temperature and reinforcing particle size, although data available in the literature are sometimes contradictory [48]. Both micro and macro-porosities can be controlled to a limited extent either by isothermal holding between the oxidation temperature and the liquidus of the alloy before solidification, or by suitably altering the alloy composition [45].

(i) Infiltration into SiC preforms

SiC inherently consists of an oxide (SiO_2) layer of a few nanometers. When SiC powder is sintered in air to make the preform, the surface oxide layer thickens with increasing time and temperature. In order to infiltrate aluminum alloys into SiC preforms, high Si containing

alloys (at least 8-10 wt%) are preferred because they suppress the formation of Al_4C_3 [39]. The silica layer on the surface of the SiC is reduced by the advancing aluminum and causes reactive wetting[1] through the following reaction:

$$3SiO_2 + 4Al \longrightarrow 3Si + 2Al_2O_3 \qquad (2.1)$$
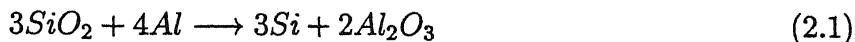
Such reaction induced wetting is sensitive to both alloy composition and the substrate. Si released by reduction of silica occupies a significant portion of the channel space and in some instances, solid Si in the channels inhibit further growth by 'choking' the micro-channels. Further, redissolution of Si into the liquid aluminum can alter the oxidation kinetics [63]. Simultaneously, Al_2O_3 nucleating on the SiC particles, competes with the epitaxially growing Al_2O_3 in the liquid. From theoretical calculations, Al_2O_3 generated via secondary nucleation was found to be between 25–30 *vol.%* of the total alumina present in the Al_2O_3/Al composite [48]. Thus, the secondary nucleation of alumina not only refines the grain size in a limited way, but also results in a randomly oriented structure in the infiltrated Al_2O_3/Al composite. However, alumina crystals maintain preferred crystallographic orientation along [0001] for a larger distance with low angle grain boundaries [45, 48, 49, 58]. In some composites, large angle boundaries were also reported [48].

SiC preforms are infiltrated by a large number of aluminum alloys. Mg and Zn are the important alloying additives which exhibit influence over the composite growth. Especially, when Zn is present in the alloy, the particulates and the crucible wall above the liquid metal are coated with ZnO, but the growth principle is similar to that of the base alloy discussed previously. It is believed that Oxygen is partially transferred to the aluminum by continuous reaction of ZnO layer formed above the molten aluminum according to the reaction:

$$3ZnO + 2Al \longrightarrow Al_2O_3 + 3Zn \qquad (2.2)$$
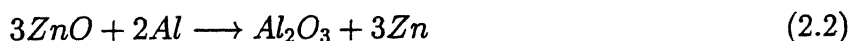
giving rise to secondary Al_2O_3 nucleation on the surface of SiC particulates [45].

---

[1]This was verified by infiltrating through silica free SiC (acid washed) where no infiltration could be achieved.

(ii) Infiltration into Al_2O_3 preforms

Unlike SiC, Al_2O_3 is stable up to higher temperatures and does not degenerate in the presence of an aluminum alloy at the oxidation temperatures. In the case of Al–Mg and Al–Si–Mg alloys, Mg reacts with Al_2O_3 to form spinel at the interface. The degree of conversion from Al_2O_3 to $MgAl_2O_4$ depends on the concentration of Mg and reaction temperature. When Al-5Zn alloy was used for infiltration, the normalized growth rates increased by a factor of four as compared to oxidation into free space [48]. A ZnO layer was formed on the preform particulates giving rise to a reduction induced wetting. But the fast growth rates tend to result in an undulated growth front and non-uniform infiltration, leaving behind macro-porosities within the composite. The former could also be due to uneven coating of the Al_2O_3 particulates, as the ZnO vapour chooses 'preferred' path for vapour transport and deposition. This problem is partially overcome by addition of small amounts of Mg, which stabilizes the growth front. Although there are similarities in the role of Mg and Zn in DIMOX, the differences in their individual contributions are not fully understood.

In Al–Si–Mg alloy infiltrated SiC composite, there was no evidence for any crystallographic orientation relationship between the oxidation product (Al_2O_3) and the particles of the preform. On the other hand, in Al-5Zn alloy infiltrated Al_2O_3 composites, secondary nucleation of Al_2O_3 are reported to exhibit epitaxial growth on the preform particles [48].

(d) Nitridation of liquid alloys

When pure aluminum is held in Nitrogen atmosphere above its melting point, it forms a passivating nitride layer on the surface which is stable and prevents further reaction. But, in the presence of alloying additions, such as Mg and Si, the passivating layer becomes unstable and exposes the underlying metal to the atmosphere resulting in continuous nitride formation. The process is analogous to that observed in oxidation [58], where the phenomenon is understood to a large extent. An interconnected and interpenetrating Al_2O_3/Al composite is formed by the diffusion of Oxygen through a magnesia and spinel layer into the underlying aluminum alloy. Similar microstructures of AlN/Al are evolved by the adsorbed Nitrogen

being precipitated as AlN within the aluminum matrix [65].

Directed melt nitridation is in some ways a more attractive process, as the process variables cover a wide range of microstructures and consequently, a spectrum of properties. The activation energy for nitride formation (AlN ≈ 100 kJ/mol) [65] is by far less compared to oxidation (Al$_2$O$_3$ ≈ 400 kJ/mol). Moreover, the nitride growth rates (3×10^{-2} $g/cm^2/s$) are higher compared to oxidation by a factor of three [66].

In the initial stages, understanding of the nitridation process was made difficult by several processes that are taking place simultaneously, namely (i) nitride formation, (ii) wicking of metal through the reaction product and (iii) growth of composite through the preform void space (when a preform is in use). The dominant variables which effectively control the process are (i) the alloying additions, (ii) reaction atmosphere, (iii) processing temperature, (iv) time and (v) the preform material being used. These variables influence one or more of the above mentioned processes and make the identification of their individual roles complex in the overall process. But such an effort is necessary to have a better understanding of the reaction mechanism. In the following sections, an analysis of the role of individual variables and their collective influence on microstructure development are elucidated.

(i) Role of atmosphere

A necessary but not sufficient condition for nitride formation is an Oxygen and moisture free atmosphere [67,68]. For aluminum to nitride rather than oxidize, the Oxygen partial pressure has to be maintained below a threshold value. The Gibbs free energy for the reaction:

$$Al_2O_3 + N_2 \longrightarrow 2AlN + \frac{3}{2}O_2 \qquad (2.3)$$
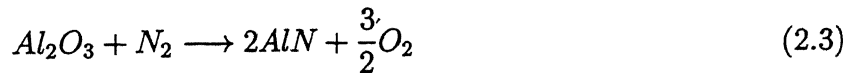
at 1000^oC is $\Delta G_f^o = +908$ kJ/mol. For AlN to be the stable phase, the equilibrium has to shift to the right. The equilibrium partial pressure of Oxygen is given as:

$$p_{O_2} = \left[\frac{a_{Al_2O_3}}{a_{AlN}} exp \left(-\frac{\Delta G_f^o}{RT} \right) \right]^{2/3} \qquad (2.4)$$

Assuming $p_{N_2} = 1$, the critical Oxygen partial pressure for nitride formation is $<10^{-20}$ Pa. But nitride formation is observed much before such gas purity levels are obtained as reaction

kinetics overrules. Moreover, when there is sufficient Mg in the alloy, it forms a vapour cloud just above the alloy surface [66]. From Pourbaix diagram (Figure 2.6), it is known that Mg oxidizes down to very low partial pressures of Oxygen ($p_{O_2} = 10^{-30}$ Pa). In this way, Mg serves as an Oxygen getter, such that the molten metal is able to 'see' a reducing atmosphere, which is favourable for nitride formation.
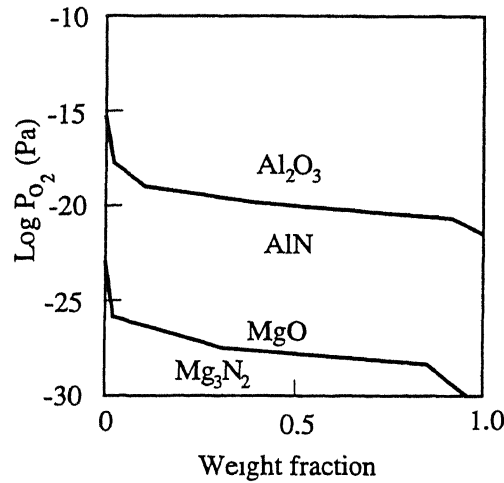
Figure 2.6: Isothermal Pourbaix diagram at $1000^{\circ}C$ for the condensed phase mixtures of Al-N-O and Mg-N-O systems[66].

Scholz and Greil [66] have done thermodynamic computations to find the equilibrium phases for the Al–Si–Mg alloy system, under various Oxygen partial pressures for static and flowing Nitrogen gas conditions. The Oxygen gettering by Mg proved very effective under static conditions, whereas under flowing gas conditions, to achieve similar results, a lower partial pressure of Oxygen is required. This is because the gas flow continuously depletes the Mg vapour cloud which is present just above the alloy surface. It was also observed that the Oxygen content in the gas (along with Mg in the alloy), strongly affects the nitride phase formation in the matrix and serves as an effective variable to control the process kinetics. When the Oxygen content was increased from 3×10^{-4} to 3.1 *vol.%* O_2 with 0.7 *vol.%* H_2, the amount of AlN formed decreased and a solid layer of MgO was deposited on the sample surface [66]. For AlN/Al composite formation, it is desirable to maintain the Oxygen content in the atmosphere to a minimum. Additionally, forming gas (N_2-4%H_2) further decreases the Oxygen partial pressure in the gas [66].

(ii) Alloying additions

The role of alloying additions, such as Mg, Li and Si was examined by examined by several groups [68–70]. Some of the alloys that were used contained small quantities of other alloying additions/impurities, such as Fe, Zn, Cu and Ni. Mg was found to be an essential dopant, as in its absence the passivating surface nitride layer becomes stable. and no composite development was possible [67]. The specific volume of the nitride layer is larger than unity ($V_{AlN}/V_{Al} = 1.26$), resulting in a protective nitride surface layer. Scholz and Greil [66] report that Mg has a catalytic effect on nitride formation, such that it helps transfer the surface reaction into a volume reaction. Thus, with the other alloying elements remaining fixed, by varying the Mg content in the alloy, three domains of reaction mechanism were proposed, namely (i) formation of dense passivating surface nitride, (ii) volume reaction where the AlN is dispersed throughout the aluminum matrix and (iii) heterogeneous combustion with complete conversion of Al to AlN.
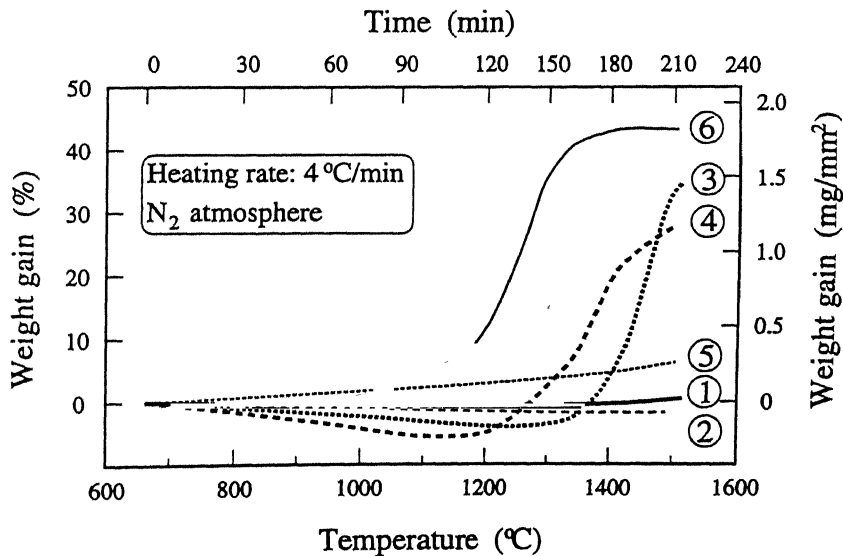
Figure 2.7: Weight gain curves showing the effect of alloying additives (Mg and Si) on heating in Nitrogen atmosphere[69]. (1) Pure Al (99.999%), (2) Al-10Si, (3) Al-10Si-5Mg, (4) Al-10Si-10Mg, (5) Al-5Mg, and (6) Al-3Mg-5Si.

LeHuy and Dallaire [69] are of the opinion that both Si and Mg are indispensable in the alloy. Using constant heating rate experiments with a TGA arrangement, they confirmed that Al-Mg and Al-Si binary alloys do not result in substantial growth rate even at 1450^oC; whereas

ternary alloys of Al–Si–Mg showed accelerated weight gains beyond $1200°C$, resulting in complete conversion to AlN (Figure 2.7). The above work has also confirmed that there is a Mg loss from the alloy surface due to volatilization, but the Si concentration in the alloy remains constant. More recently, Kagawa *et al.* [68] have concluded that due to Mg loss and conversion of Al to AlN, the concentration of Si increases resulting in an increase in the viscosity of the melt at the surface. This could cause a decrease in the diffusion flux of aluminum to the reaction front, and in turn leads to suppression of growth rates near the end of the process.
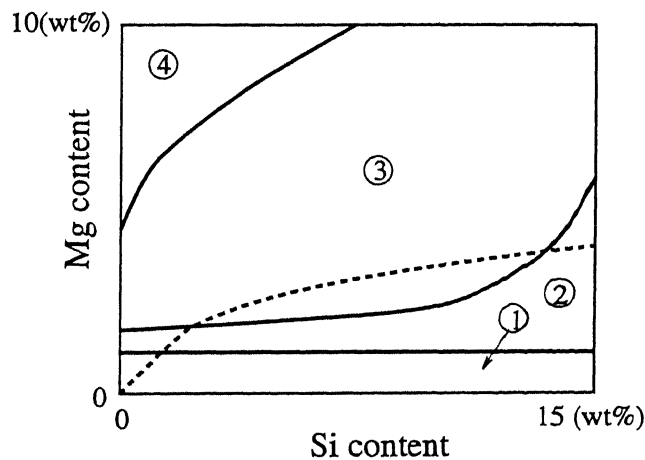
Figure 2.8: Al-(Mg,Si) reaction map showing (1) passivating surface nitridation, (2) diffusion controlled volume nitridation, (3) volume nitridation involving outward growth of AlN/Al and (4) break-away nitridation domains[66].

Scholz and Greil [66] have distinguished three reaction mechanism domains based on the alloy composition (Figure 2.8). (1) When the Mg/Si ratio is less than 0.5 and Mg ≤ 1 *wt.%*, the nitridation is only a surface phenomenon with less than 10% of the aluminum converted to AlN. (2) With Mg between 2–4 *wt.%* and Si ≤ 5 *wt.%*, an interconnected AlN/Al composite grows outward with up to 50% conversion. (3) With Mg ≥ 4 *wt.%* and Mg/Si ratio >10, there is a heterogeneous combustion resulting in break-away nitridation with complete conversion of aluminum to AlN. From the above arguments, it is supposed that Mg serves as an initiator with an accelerating influence on nitride formation, whereas Si has an inhibiting effect.

(iii) Temperature and pressure

Temperature is an important variable in nitridation, as previously seen in conjunction with atmosphere and alloying additions. The reaction between Nitrogen and aluminum occurs at temperatures above $700^{\circ}C$. While pure aluminum forms a stable nitride surface layer which is passivating, depending on the atmosphere and temperature, alloys containing Mg show a tendency to continuously nitride. It is observed that by increasing the temperature from 800 to $1050^{\circ}C$, the resultant microstructure becomes progressively finer and excessively ceramic dominant. This provides the needed flexibility to produce both metal-matrix and ceramic-matrix composites. By varying the temperature, Kúdela and Schweighofer [71] determined the critical temperature at which the reaction rate changes suddenly, corresponding to a change in the reaction mechanism. In Figure 2.9, T_2 corresponds to the transition temper-
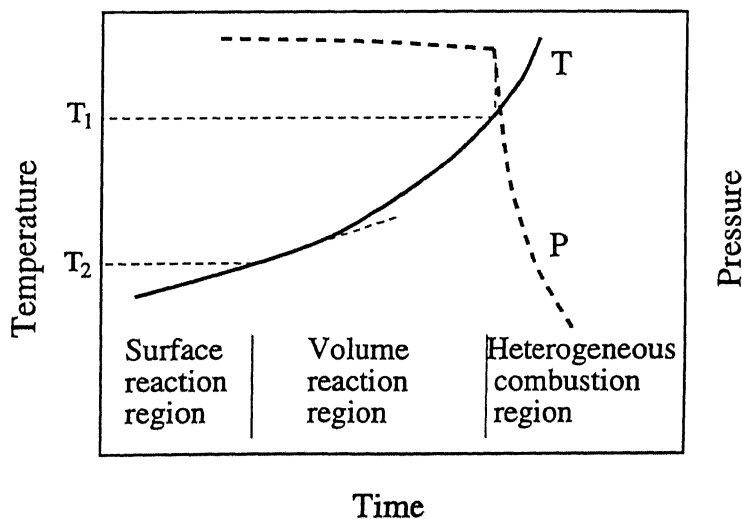
Figure 2.9: Temperature and pressure curves delineating reaction domains as a function of time. The initiation of heterogeneous combustion reaction is marked by a sudden drop in Nitrogen pressure due to rapid conversion of Al to AlN[71].

ature, which is characterized by a rapid generation of reaction heat, when the mechanism changes from a surface to a volume reaction. An acceleration of volume reaction takes place above T_1, such that the reaction is no longer thermodynamically stable and follows the principle of heterogeneous combustion synthesis. The change in reaction is distinguished by a sudden decrease in Nitrogen pressure.

Schweighofer and Kúdela [72] have reported that the temperature at which the reaction
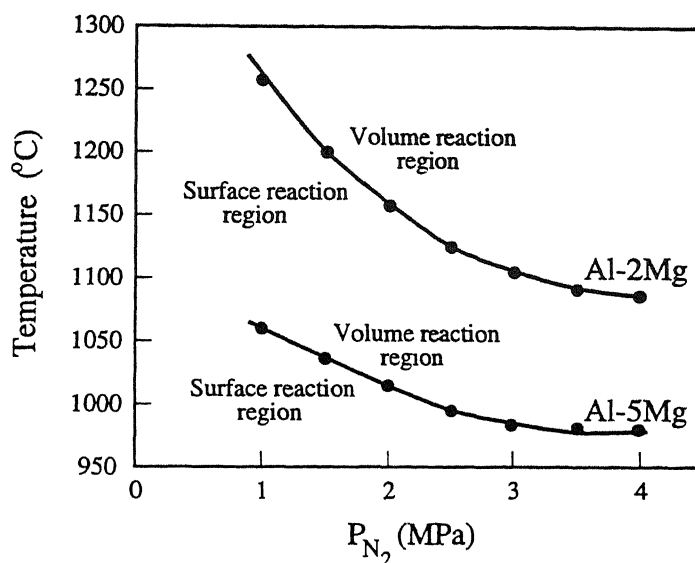
Figure 2.10: Temperature vs. Nitrogen pressure curves separating surface reaction and volume reaction domains for Al-2Mg and Al-5Mg alloys[72].

changes from a surface phenomenon to a volume reaction, decreases with increase in Nitrogen pressure. According to Figure 2.10, when the Mg content is increased from 2–5 *wt.*%, the temperature for complete nitride formation drops by 200°C at 1 MPa. Further, LeHuy and Dallaire [69] have drawn Arrhenius plots for nitride formation in the absence of a preform. The calculated activation energy for nitride formation was found to vary between 110–190 kJ/mol, depending on the alloy composition.

(e) Multiphase composites *via* melt nitridation

(i) Preform influence

The preform is an as-poured or loose sintered porous ceramic body, which the liquid metal fills up resulting in a fully dense composite. Thus, the ceramic reinforcing phase and the matrix are 3-dimensionally connected augmenting each others performance. The preform material is an important variable, both from the processing viewpoint and the final mechanical properties achieved by the composite. The preform serves to contain the composite growth within itself resulting in near net-shape of the component. Several filler materials have been successfully utilized in nitridation experiments, namely Al_2O_3, SiC, B_4C_3, TiB_2

and AlN. Lanxide Corporation, U.S.A. have designated the trade name PRIMEX for this process.
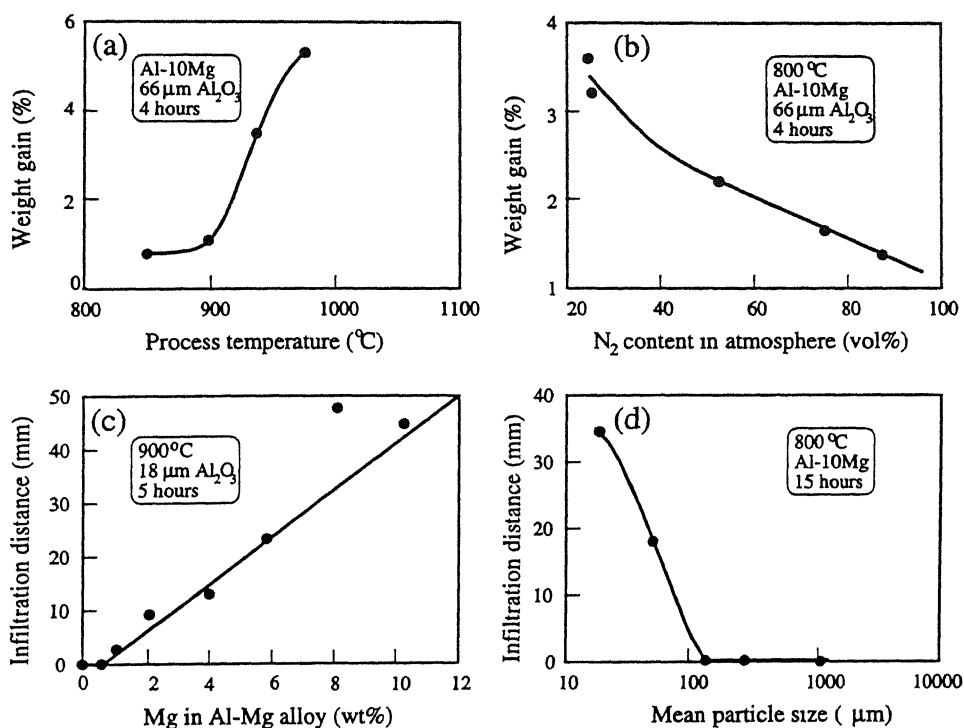
Figure 2.11: Weight gain vs. (a) process temperature[67] and (b) Nitrogen content in N_2/Ar atmosphere. Infiltration distance vs. (c) Mg content in aluminum alloy and (d) mean particle size[83].

It was noted earlier that a binary Al-Mg alloy only results in surface nitride formation. But, when infiltrate into fused Al_2O_3 preform, the matrix has a fine distribution of AlN. The infiltration distance is dependent on the reinforcement size, which increases with decrease in the preform particle size (Figure 2.11). Thus, the initial obstacle to be overcome is that the metal should wet the preform to facilitate spontaneous infiltration. While there is ample data on the wetting of ceramic substrates by aluminum alloys in air or inert atmosphere [73–78], there is a paucity of information on wetting in Nitrogen atmosphere. The experimental data available is often unreliable and contradictory, as contact angle values are very sensitive to impurities in the alloy and atmosphere. For this reason, the contact angle values are specific to the experimental conditions. But Mg presence in the alloy is found to decrease the contact angle [80,81].

Alternatively, the infiltration can be improved by inducing a reaction between the alloy and the filler material. In certain cases, the metal tends to climb on the filler material ahead of the composite growth front [82]. Both Al_2O_3 and SiC react with Mg containing aluminum alloys, culminating in spontaneous spreading of the alloy over the substrate material. Al_2O_3 particles form a spinel layer by reacting with Mg which is available in the alloy. Similarly, SiO_2 surface layer on SiC reacts with aluminum. In extreme cases, shattered SiC particles were found in the matrix [82]. This is due to aluminum reacting with SiC particulates along particular crystallographic directions to form carbide according to the reaction:

$$3SiC + 4Al \longrightarrow Al_4C_3 + 3Si \tag{2.5}$$
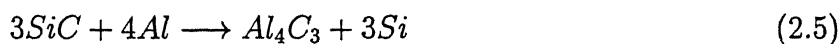
The formation of undesirable carbide phases is detrimental to mechanical properties. The above reaction can be suppressed by incorporating a higher Si content in the alloy [79].

(ii) Alloying additions

In the previous section, the wetting between molten alloy and the filler material was emphasized. The contact angle can be modified by altering the alloy composition. Several groups have reported enhanced wetting due to the presence of Mg in the alloy [80–85]. Banerji *et al.* [86] concluded that an alloying element can enhance wetting of a solid substrate in three ways, namely (i) by reducing the surface tension of the alloy, (ii) by decreasing the solid-liquid interfacial energy and (iii) by promoting a chemical reaction at the solid-liquid interface. Oh *et al.* [81] are of the opinion that Mg enhances wetting of ceramic substrates by promoting interfacial reaction.

Aghajanian *et al.* [83] carried out infiltration experiments in fused 18 μm Al_2O_3 particulate preform with aluminum alloys having varying amounts of Mg. They observed that a critical amount of Mg (0.5–1.0 *wt.%*) was required for infiltration to occur. Further, the infiltration distance increases linearly with Mg content (Figure 2.11). Moreover, the critical amount of Mg for infiltration increases with decrease in process temperature.

While Mg is the dominant variable among the alloying additives, Si in conjunction with Mg is believed to enhance infiltration by modifying the viscosity of the melt. Cu additions increase

the viscosity of the melt and retard infiltration kinetics. Fe as a minor alloying addition appears to aid wetting of the preform and facilitate infiltration at lower temperatures [65, 67, 83]. However, no explanation is offered in the literature for such behaviour.

(iii) Role of atmosphere

It is well established that for infiltration to occur, apart from the critical amount of Mg, the atmosphere must be Oxygen and moisture free. This criterion is satisfied by ensuring that the gas is Oxygen free and use of a local gettering agent, such as Mg, in sufficient quantity in the alloy. Pure Nitrogen causes a decrease in the surface tension of the alloy and enhances wetting of the ceramic filler material [83]. Creber *et al.* [65] in the course of their experiments found that pure Nitrogen, Nitrogen-Argon mixed gas (with N_2 as low as 10%) or forming gas (N_2-4%H_2) could be used as the reaction gas without extra purification as long as the Oxygen and moisture levels were maintained at a minimum.

To understand the influence of Nitrogen on infiltration, Ahajanian *et al.* [67] diluted the gas with varying amounts of Argon and studied the infiltration kinetics of Al-10Mg alloy into 220 grit Al_2O_3 preform, over a period of 4 hours at $800^{o}C$. They noted an absence of infiltration in a 100% Argon atmosphere, partial infiltration in a 90%Ar-10%N_2 atmosphere and complete infiltration in atmospheres containing more than 25%N_2. Furthermore, microstructural control within the matrix could also be achieved by varying the partial pressure of Nitrogen in the atmosphere. Figure 2.11 shows that the amount of nitride present in the matrix increases with decrease in the partial pressure of Nitrogen. With regard to infiltration kinetics, it becomes clear that at higher partial pressures of Nitrogen, the infiltration rate is high. In such a situation, the growth front is not stationary, allowing less time for the atmosphere to react with the liquid metal under identical conditions of temperature and total gas pressure. The converse is also true at low partial pressures of Nitrogen. On the other hand, Creber *et al.* [65] have reported that the growth rate decreases as the partial pressure of Nitrogen in the atmosphere decreases. It is generally understood that forming gas improves wetting of the filler material and promotes infiltration at lower temperatures [67]. Moreover, it appears that there are similarities between nitridation of Si and aluminum. They respond in a similar

manner in the presence of Fe and Hydrogen [87]. However, in both cases the mechanism is not fully understood.

(iv) Temperature and time

Unlike in oxidation experiments, variation in temperature causes drastic changes in the microstructural evolution of AlN/Al composites. At 900^oC, the SiC reinforced composite appear as a metal matrix composite with fine dispersoids of AlN within the matrix. On the other hand, composites grown at 1100^oC were predominantly ceramic with fine metal channels within an AlN matrix [82]. Aghajanian *et al.* [83] have weight gain *vs* temperature curves for the Al-10Mg alloy infiltrated into 66 μm fused Al_2O_3. They observed that the amount of AlN formed increases exponentially with process temperature (Figure 2.11). The same group also found that for a given set of processing conditions, a critical temperature is required to induce spontaneous infiltration [67]. For example, under similar conditions, an Al-8Mg alloy did not infiltrate a 18 μm fused Al_2O_3 preform at 750^oC, whereas at 800^oC, a 19 mm composite growth was observed. Secondly, the interface reaction taking place between the filler material and the alloy are diffusion controlled [88]. Increasing the reaction time leads to parabolic growth of the $MgAl_2O_4$ interface layer in Al_2O_3 fibre infiltrated composites. The strength and toughness of these composites show considerable improvement with increasing spinel layer thickness.

2.2.2 Liquid-liquid reactions

(a) Sol-gel synthesis

Sol-gel processing involves the hydrolysis and condensation of a molecular precursor, such as a metal alkoxide [90]. The hydrolysis reaction, which involves the addition of water molecules to the alkoxide, produces reactive monomers. During condensation, these monomers link-up to form a solution of inorganic polymers (sol). As condensation proceeds, the viscosity of the sol increases due to formation of an extended network of chemical bonds throughout the sol (gelation). The resulting sol is dried and heated at relatively low temperatures to yield

fully dense ceramic.

To synthesize metal-ceramic composites, both metal and ceramic sources must be incorporated during synthesis [91,92]. This has been achieved in two ways, namely polymeric route and colloidal route. In the case of Al_2O_3/Ni composite formation *via* the polymeric route, the metal precursor ($Ni(CHOO)_2$) is introduced during the hydrolysis and condensation of the ceramic precursor [92]. On the other hand, the colloidal route involves the precipitation of $Ni(OH)_2$ onto a colloidal suspension of α-Al_2O_3 particles. The transformation to Al_2O_3/Ni composite was accomplished by calcination of the colloidal suspension in a reducing atmosphere, followed by hot-pressing at $1400^\circ C$ at an Oxygen partial pressure of 10^{-12} *atm*. While it is possible to synthesize Al_2O_3/Ni composites with ceramic content varying from 33–95 *vol.%*, composites with >20 *vol.%*Ni exhibit microstructure composed of continuous Ni and Al_2O_3 network. The composites display enhanced fracture toughness ($\sim$8.5 $MPa\sqrt{m}$) compared to sintered alumina.

Recently, Chakravorty *et al.* [93] have used sol-gel synthesis to process nanocomposites containing metal particles of a few micron thickness in a ceramic matrix. The process involves an ion exchange reaction followed by a reduction treatment to precipitate a narrow size range of metal particles (Fe, Cr, Ni, Cu, etc.) in a glass or polymer matrix [94,95]. The drawback of this process is the composite microstructure is limited to a few micron thickness at the surface of the glass-ceramic concerned.

2.2.3 Liquid-solid reactions

(a) Reactive Metal Penetration (RMP)

Reactive Metal Penetration, also known as Co-Continuous Ceramic Composite (C^4) technology is used to produce composite materials by liquid–solid displacement reactions. This novel technique differs from physical infiltration since the initial preform is fully dense. Similar to infiltration, RMP is a net-shape process with very little change in preform and final composite volume.

The RMP process uses a redox reaction to convert silica/mullite to Al_2O_3. When silica tubes are immersed in molten aluminum at temperatures above $1000°C$, an exchange reaction takes place between the molten metal and preform according to the general reaction [96,97]:

$$3 \ SiO_2 + (4+x) \ Al \longrightarrow 2 \ Al_2O_3 + 3 \ \underline{Si} + x \ Al \qquad (2.6)$$
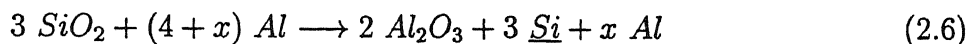
When $x > 0$, aluminum is retained in the composite along with other reaction products. An analogous phenomenon is observed when mullite preforms are reacted with molten aluminum in vacuum or flowing Ar atmosphere. The general reaction is expressed as [98,99]:

$$3 \ Al_6Si_2O_{13} + (8+x) \ Al \longrightarrow 13 \ Al_2O_3 + 6 \ \underline{Si} + x \ Al \qquad (2.7)$$
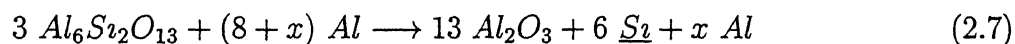
Experiments with commercial mullite containing a silicate grain boundary phase averaging $<2 \ vol.\%$ were carried out. The reactive metal penetration produces a fine grained alumina network with an interpenetrating metal phase. Though the final microstructures are similar, the reaction mechanisms for penetration of amorphous silica and (ceramic) mullite peforms are different. Breslin *et al.* [97] are of the opinion that the reaction layer between aluminum and amorphous SiO_2 has a lower molar volume causing crack formation in silica, which continuously expose unreacted SiO_2 to the molten aluminum. On the other hand, TEM examination of partially reacted mullite samples suggest that the process is sustained by the diffusion of Al along mullite grain boundaries, followed by a redox reaction that converts mullite to Al_2O_3 [100]. Flexural strength of 250–320 MPa and enhanced fracture toughness of 5–9 $MPa\sqrt{m}$ are reported for mullite infiltrated composites [98]. Hardness and Young's modulus approach that of alumina.

(b) Directed Metal Reaction (DMR)

Recently, a new class of composite material has been prepared by the directed reaction of liquid Zr with B_4C to form Zr containing ceramic composites. The process is flexible to produce microstructure composed of ZrB_2 platelets in a zirconium carbide matrix, with a controlled amount of residual Zr metal. The DMR process is akin to directed melt infiltration in an oxidizing or nitriding atmosphere, except that there is no gaseous phase reactant. In

both processes, the residual metal retained in the composite microstructure is expected to improve fracture toughness. However, liquid melt oxidation/nitridation reactions lead to a relatively higher proportion of interconnected metal.

$$(2.2+x)Zr+0.6B_4C \longrightarrow 1.2ZrB_2+ZrC_{0.6}+xZr$$
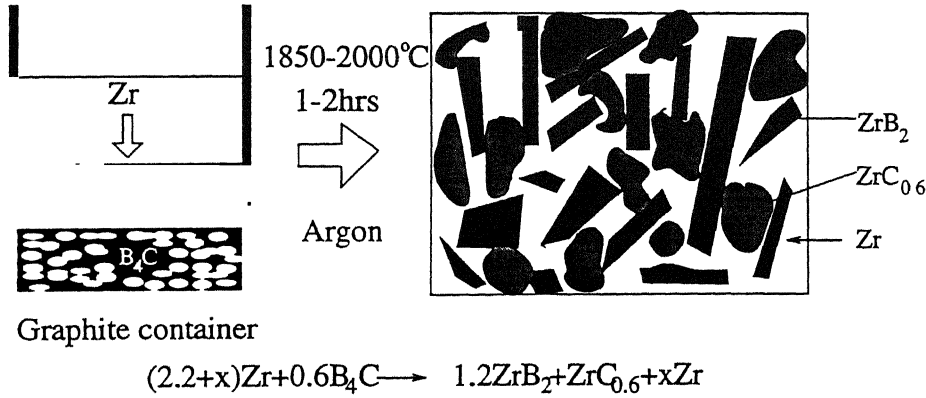
Figure 2.12: Processing and microstructure (schematic) of ZrB_2 platelet reinforced $ZrC_{0.6}$/Zr composite[102].

In this process, Zr metal powder is kept on top of a B_4C (typically 7–8 μm) bed, which is placed in a graphite crucible and heated to 1900^oC in an Argon atmosphere (Figure 2.12). The reaction between Zr and B_4C is exothermic with the temperature reaching above 2300^oC during infiltration. The reaction rate is parabolic with time and the parabolic constant varies between 1.6×10^{-2}–3.9×10^{-2} cm/s [101]. Composite microstructures are formed according to the general reaction:

$$(2.2 + x)Zr + 0.6B_4C \longrightarrow 1.2ZrB_2 + ZrC_{0.6} + xZr \qquad (2.8)$$
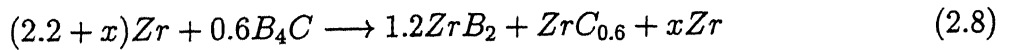
where x is the excess moles of Zr added to the reactant. When $x = 0$, there is no free Zr in the body; whereas with $x = 0.5$, 18 $vol.\%$ of residual Zr is retained in the composite. The properties of the composite material largely depend on the residual metal content. For instance, the fracture toughness increases from 11 to 22 $MPa\sqrt{m}$ when the residual metal is augmented from 2 to 30 $vol.\%$, respectively [102,103].

The three phases present in the composite microstructure are ZrB_2, a carbon deficient ZrC_x ($x = 0.6$) and α-Zr. Bravel and Johnson [101] have observed the crystallographic orientation relationship between the constituent phases to be random. The reaction mechanism proposed by Johnson *et al.* [102] suggests that when the molten Zr comes in contact with B_4C, they

react exothermically to form a boron-rich liquid. Further reaction is sustained by continuous dissolution of B_4C, as the boron-rich liquid is drawn into B_4C. The $ZrB_2/ZrC/Zr$ composite homogenizes rapidly to give rise to uniform microstructure without micro or macro-porosities [104].

(c) Mixed Salt Reaction

The grain refinement technology of aluminum alloys has been modified by the London Scandinavian Metallurgical Company to produce metal matrix composites [105]. Mixed salts of titanium and boron react in molten aluminum to form TiB_2. The by-products are decanted and the remaining melt is cast into ingots. A 2014 aluminum alloy with very fine particle dispersion of TiB_2 (1–2 μm) was claimed to improve yield strength up to 500 MPa with an elongation of 5%. However, the interface cleanliness is questionable due to the usage of salts. It is argued that the contamination by salts would offset the property enhancement brought about by the boride particles [30].

2.2.4   Solid-gas reactions

(a) Reduction reaction synthesis

Metal-ceramic composite structures are produced by selective reduction of an oxide to a metal. Such reduction reactions were earlier effectively used by Handwerker *et al.* [106] for obtaining Na_2O_3-Cr_2O_3-Cr composites and Qi *et al.* [107] for making rare earth containing magnetic alloys. The reduction synthesis has been successfully demonstrated in the Fe–Mn–O and Ni–Al–O systems, by judicious control of the process variables, namely oxide composition, partial pressure of Oxygen, annealing temperature and time. In these systems, the nucleation and growth of the metallic phase can be controlled to obtain different microstructures [108,109]. In the case of Fe–Mn–O reduction synthesis, ceramic grains with controlled thickness of metallic phase at the boundaries or ceramic grains containing fine distribution of metallic particles (ductile phase toughened ceramics) are possible. On the other hand,

reduction synthesis of Ni–Al–O resulted in equiaxed metallic crystals (<0.5 μm) dispersed within a ceramic matrix or rod-like metallic particles within a defect spinel. However, for effective control of the reduction reactions in metal containing ceramics, a knowledge of the phase diagram with respect to the partial pressure of Oxygen and temperature is essential.
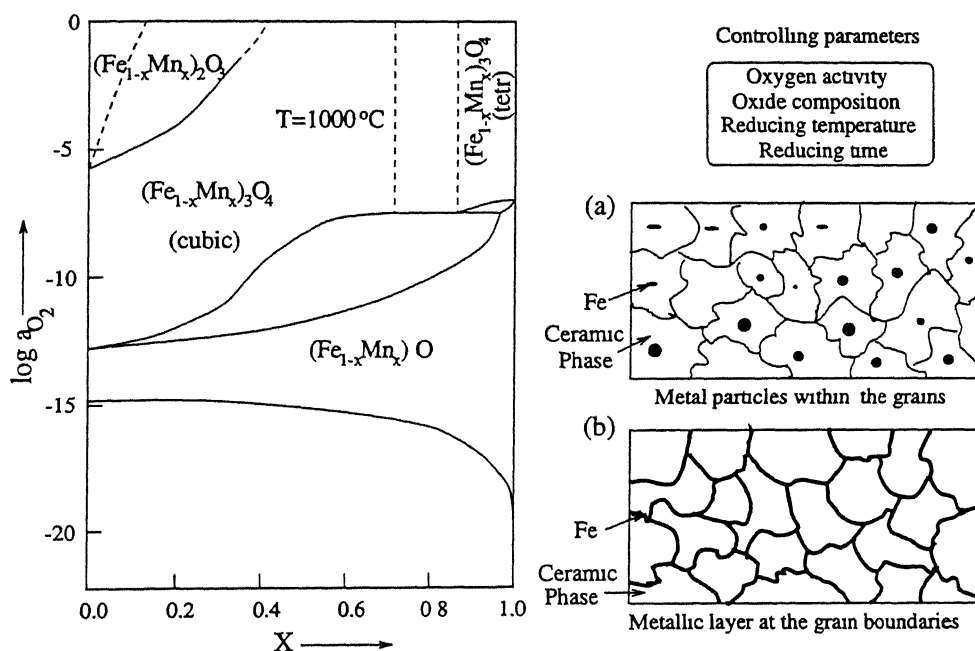
Figure 2.13: Oxygen partial pressure phase diagram of Fe–Mn–O at $1000°C$[110] and schematic microstructure observed in $(Fe_{0.6}Mn_{0.4})O$ reduced in 5% CO/N_2 atmosphere at (a) $900°C$, showing Fe particles within the ceramic grains and (b) $800°C$, producing metallic Fe at the grain boundary

For example, the reduction reaction synthesis in the Fe–Mn–O system is illustrated in Figure 2.13. When the partial pressure of Oxygen was decreased below 1.25×10^{-5} atmospheres ($\log a_{O_2} = -15.1$), a metallic alloy of almost pure iron (with inclusions of manganese) formed within the mixed oxide phase. For instance, when $(Fe_{0.6}Mn_{0.4})O$ was reduced for 4 hours at $800°C$ in 5% CO containing N_2 gas, the final microstructure exhibited a 400 nm thick iron boundary enveloping the grains. The metallic phase at the grain boundary thickens into a separate phase with increased annealing time; whereas when annealing temperature was increased to $900°C$, the metallic phase nucleates at several locations within the grain (Figure 2.13). Similar effects were observed with variation of Oxygen partial pressure. A fracture toughness increment of 0.6 to 0.7 $MPa\sqrt{m}$ was reported for these ductile phase toughened structures depending on the volume fraction of the metallic dispersion. Similar

studies were carried out in the Ni–Al–O system, where an improved indentation fracture toughness was observed for the Ni–Al_2O_3 two phase mixture compared to $NiAl_2O_4$.

The current limitations of reduction reaction synthesis are (i) lack of phase diagrams for various oxide systems with variation of Oxygen partial pressure and temperature, (ii) properties of these composite structures are not entirely known and (iii) synthesis is confined to only laboratory studies and commercial feasibility of the process is yet to be explored.

2.2.5   Solid-solid reactions

(a) Self-propagating High-temperature Synthesis (SHS)

Combustion synthesis or SHS is an innovative technique to produce metal, ceramic and intermetallic composites. The key principle of the process is the conversion of chemical energy to thermal energy. A large enthalpy release sustains the propagation of a dynamic combustion wave through the reactant. For a reaction to become self-sustaining, (i) the reaction must be highly exothermic, (ii) one of the reactants should be a liquid or a vapour to enhance transport to the reaction front and (iii) the rate of heat dissipation must be less than the rate of heat generation, to ensure that the reaction is not extinguished.

Initially, the reactant materials are mixed together in the powder form and compacted in the green state. The combustion wave initiated by an external source, moves through the compact with a high velocity when the adiabatic temperature is very high. Control over the process is established by partially diluting the reactants with the product phase. If the combustion temperature is low, pre-heating the sample prior to the combustion can be resorted to (thermal explosion). Sometimes, chemical reaction can also be initiated by shock-compression (shock-induced reaction synthesis). This process effectively takes the advantage of high pressure and temperature that are simultaneously generated during the passage of the shock-wave. The main advantages of the combustion process are: efficient utilization of the reaction energy, quick synthesis and purification due to volatilization of impurities. The main drawback of the process is high porosity in the final product, which can be eliminated by

post synthesis treatment, such as hot pressing, HIPing, etc. The processing aspects, general characteristics, theoretical aspects and limitations are reported in the literature [111–115].

Several investigators have prepared intermetallic and metal-ceramic composites using SHS. However, in all these systems the reinforcing phase is added externally. Lebrat *et al.* [116] synthesized dense Ni_3Al with low porosity levels ($\leq 5\%$) by controlling the porosity in green compacts. Similarly, SiC fibre reinforced aluminum was processed by Choi *et al.* [117]. However, only limited studies have been done on *in situ* formation of reinforcements. Using elemental Ti, B and Cu, TiB_2 whisker reinforced copper composites were produced. These composites exhibited a fracture toughness of 9.9 $MPa\sqrt{m}$ due to ductile phase (Cu) toughening, although brittle phases like TiB_2, Ti_2Cu, Ti_3Cu_4 and porosity inhibited further toughness increment. A correlation between mechanical properties and the combustion temperature was also established in this study [118]. Multiphase composites like $TiC+Al_2O_3$ reinforced with aluminum were processed by the combustion synthesis of TiO_2, C and Al [119]. When there is an excess of aluminum, the reaction is expressed as:

$$3TiO_2 + 3C + (4+x)Al \longrightarrow 3TiC + 2Al_2O_3 + xAl \qquad (2.9)$$
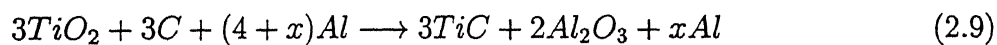
The residual aluminum fills up the void space in the $TiC+Al_2O_3$ mixture. Care should be taken to control the temperature, so that it does not exceed the boiling point of liquid aluminum. On similar lines, it is possible to obtain TiC dispersed AlNi [120]. Efforts are on to produce highly complex, multiphase composites using SHS.

(b) Reaction Sintering

Reaction sintering essentially differs from the SHS process due to the absence of thermal run-away effects. Two processes are identified under this section, namely Reaction Bonded Aluminum Oxide (RBAO) and Alumina-Aluminide Alloys (3A). RBAO process enables fabrication of low shrinkage, high strength Al_2O_3-based composites [121]. Attrition milled Al_2O_3/Al powder mixtures are hot-pressed (100–300 MPa) in the temperature range 300–1000$^{\circ}C$. Aluminum oxidizes to form small Al_2O_3 crystallites, which sinter below 1200$^{\circ}C$. The volume change associated with sintering is compensated for by the volume expansion

associated with oxidation. Additionally, the process is flexible to the incorporation of metallic or ceramic reinforcements (Zr, Cr, Ti, Nb, SiC, etc.) during the attrition step. The initial Al_2O_3/Al volume fraction is so adjusted, such that the volume expansion associated with oxidation of reinforcement particles compensate for sintering shrinkage.

3A (read as triple A) composites are prepared by reaction sintering of intensely milled mixtures of oxide and aluminide powder according to the general reaction scheme [122,123]:

$$Me_aO_b + Al \longrightarrow Me_xAl_y + Al_2O_3 \qquad (2.10)$$
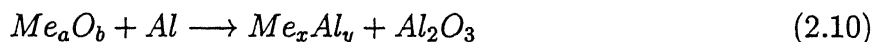
where Me_aO_b refers to any metal oxide which has a favourable Gibb's free energy for the above reaction. Although such reactions were known for long, until recently successful densification could not be achieved. A prerequisite for the 3A process is that the starting powder must be of a very fine grain size (<1 μm) and uniformly mixed. Such conditions are easily achieved by Attritor milling the source powder and compacting in a CIP. On heating the compact in vacuum or Ar atmosphere, due to the short diffusional paths involved, reaction takes place in the solid state itself, well below the melting point of aluminum ($\sim 550^oC$). In cases where the reaction is highly exothermic, excess quantity of alumina is admixed to exercise control over the reaction. Densification is achieved by sintering the reaction product (with or without admixed Al_2O_3) at temperatures higher than 1000^oC to form dense homogeneous network of ceramic and intermetallic. Composite materials, such as Al_2O_3 with TiAl, $ZrAl_3$, $NiAl_3$, FeAl, $NbAl_3$, etc., were successfully produced using this method. The main advantages of this process are the fabrication steps are technologically simple and the ceramic/intermetallic ratio together with the microstructural scale can be tailored by altering the initial powder size.

(c) XD process

This process was developed by Martin Marietta and Co., USA, and only limited information is available on process details. In this solvent assisted diffusion process, the ceramic phase is precipitated in a metallic or intermetallic matrix with the exothermic heat liberated by the self propagating reaction aiding in accelerating diffusion of the elemental species. The

accelerated chemical reaction that takes place to precipitate the reinforcement phase within the matrix, makes the process attractive [124].

Elemental or alloy powders (Al–Ti and Al–B) are mixed and heated until a molten aluminum medium forms where the elements diffuse and precipitate as compounds (TiB_2). This master alloy with a high volume fraction of sponge is further diluted with matrix metal to arrive at the desired volume fraction of reinforcement. The reinforcements are usually carbides, borides, nitrides and silicides and the matrix metal could be Al, Ti, Cu, Ni or an intermetallic, such as TiAl, Ti_3Al or NiAl. The material is further mechanically worked to break the cast structure. When the XD processed composites are subjected to thermo-mechanical treatment, the elements exhibit higher diffusivities at elevated temperatures leading to Ostwald ripening. Further, increase in the interparticle spacing results in reduced yield strength. Heat treatment of Al-TiC composites above $540^\circ C$ results in enhanced kinetics of formation of Al_3Ti and Al_4C_3, but leads to decreased ductility with increasing heat-treatment time [125]. Hence, proper care should be taken to optimize processing conditions to achieve good properties and microstructure control.

The reinforcement particles in XD processed materials are very fine and usually in the range of 0.1–0.3 μm. But the main advantage of processing *in situ* is that the interface between the particle and the matrix is clean resulting in improved toughness and modulus. High resolution electron microscopy studies reveal that the interface between TiC and Al is abrupt with no segregation of impurities. The TiC particles are faceted with their surfaces in the composite lying parallel to the new index planes of Al, namely {111} and {100}. Further, the interface bond between TiC and Al is metallic in nature due to electron transfer and intimate contact at the atomic scale [126, 127]. Similarly, studies on TiB_2/NiAl composites show that NiAl forms excellent bonds with TiB_2 and α-Al_2O_3 particulates but there appears to be no crystallographic orientation relationship [128]. No coherent or semi-coherent interface was observed between TiB_2 and NiAl, but a thin layer of Si was evident.

The microstructure produced by the various *in situ* processes discussed thus far are summarized in Table 2.3. The microstructural constituents, range of microstructural scale and

metal/ceramic ratio show wide variation in different processes. Depending on the application, a particular process can be selected and microstructurally tailored to meet specific property requirements. In the following section, the mechanical properties of *in situ* composites are highlighted. Later in the chapter, the strengthening and toughening mechanisms operating in these metal containing composites are also presented.

2.3 Mechanical properties of *in situ* composites

Although a number of techniques were developed to obtain metal dispersed ceramic matrix composites, the mechanical property data generated is confined to a limited number of materials which could be produced in bulk quantity, namely XD, PRIMEX and DIMOX materials. Some information on the other materials is available in the form of reports which are inaccessible to the author. However, the properties that are reported in the literature are summarized here. For example, in the family of XD materials, the properties of TiB_2 reinforced $Ti_3Al+TiAl$ and NiAl were listed in Table 2.4. TiB_2 dispersed ($Ti_3Al+TiAl$) with a minimum tensile strength of 860 MPa and elastic modulus of 430 GPa exhibited superior high temperature properties when compared to their counterparts (Ti alloys and superalloys) [124]. At temperatures exceeding 1000^oC, TiB_2 dispersed NiAl showed at least three fold increment over the matrix tensile strength.

In XD materials the dispersions of ceramic phase usually do not exceed 30-40 *vol.%*. On the contrary, in Al_2O_3/Al and AlN/Al materials, a wide variation in the metal/ceramic ratio is feasible. On one hand, completely ceramic matrix with some residual porosity can be achieved by treating at higher temperatures or at medium temperatures for prolonged periods. On the other hand, ceramic matrix with metal dispersions as high as 30–35 *vol.%* (in nitridation even more) is possible by proper control over temperature, time and alloy composition. The four important variables identified, namely alloy composition, process temperature, Oxygen partial pressure and time, the first two exhibit pronounced effect on the

Table 2.3: Compilation of microstructural details of *in situ* composites.

Sr. No.	Process Name	Morphology	Microstructural scale (μm)	Metal content (*vol.%*)	Example system	Remarks
1.	DIMOX	interconnected Al_2O_3 & Al	1–3	20–30	Al_2O_3/Al, SiC/Al_2O_3/Al	External reinforcement can be added.
2.	PRIMEX	interconnected AlN & Al	<2	10–80	AlN/Al, Al_2O_3/AlN/Al	External reinforcement & microstructural flexibility
3.	Sol-gel	continuous network	<1	5–70	Al_2O_3/Ni	Low temperature synthesis
4.	Reactive Metal Penetration	interconnected Al_2O_3 & (Al,Si)	1–3	5–30	Al_2O_3/(Al,Si)	Microstructure similar to DIMOX
5.	Directed Melt Reaction	interconnected Zr + ZrB_2 + ZrC	~10	5–25	ZrB_2/$ZrC_{0.6}$/Zr	Exothermic reaction between Zr & B_4C
6.	Mixed Salt Reaction	dispersed particles	1–2	>95	TiB_2/Al	Possibility of contamination from salts
7.	Reduction Reaction Synthesis	grain boundary phase or isolated particles	~0.5	<5	Fe/($Fe_{0.6}Mn_{0.4}$)O	Need Temperature vs. pO_2 phase diagram
8.	SHS	whisker or particulates	5–10	5–20	TiB_2/Cu, TiC/Al_2O_3/Al	Secondary processes needed for consolidation
9.	Reaction sintering	continuous oxide phase	<1	<10	Al_2O_3/Zr/Al	External reinforcement & low temperature synthesis
10.	XD	fine dispersoids	0.1–0.3	~70	TiC/Al	Aging treatment desirable

Table 2.4: Selected properties of XD processed materials[124].

1. Ti$_3$Al + TiAl + TiB$_2$ (30 vol% dispersions)	
Density (kg/m^3)	3990
Coef. of thermal expansion ($10^{-6}/K$)	10 at 300 K 17 at 1100 K
Elastic modulus (GPa)	430 at 300 K 380 at 800 K
Yield strength (MPa)	790 at 300 K 430 at 1073 K
Ultimate tensile strength (MPa)	860 at 300 K 600 at 1073 K
2. NiAl + TiB$_2$ (30 vol% dispersions)	
Elastic modulus (GPa)	270 at 300 K 220 at 1273 K
Fracture toughness ($MPa\sqrt{m}$)	6–7 at 300 K

oxidation kinetics [50,53,58]. In case of nitridation, processing temperature and partial pressure of Nitrogen play an important role. Newkirk *et al.* [38] reported a gradual increase in the bend strength and a drastic decrease in the fracture toughness of SiC/Al$_2$O$_3$/Al composites by increasing the oxidation temperature. Aghajanian *et al.* [129] produced composite materials with varying metal content by changing the thermal treatment. The properties of this spectrum of materials are summarized in Table 2.5. The variation in properties (mainly toughness) is attributed to the degree of plastic deformation of the metal phase behind the crack tip before complete failure. The corresponding work of fracture varies from 70–350 Jm^{-2}. All mechanical properties decline at temperatures above 700°C, due to softening of the metallic phase. Swartz *et al.* [43] have determined the dielectric constants of Al$_2$O$_3$/Al composites parallel and perpendicular to the c-axis of alumina as 8.4 and 6.4, respectively.

The properties of Al$_2$O$_3$/Al composites are further influenced by the presence of filler material although the influence of particulates is not pronounced (Table 2.5). Incorporation of SiC and

Table 2.5: Mechanical properties of DIMOX composites[41–44,67,124,130].

Property	Al_2O_3/Al composite without preform[†]	$Al_2O_{3p}/$ Al_2O_3/Al	$SiC_p/$ Al_2O_3/Al	$SiC_f/Al_2O_3/Al$ uniaxial	$SiC_f/Al_2O_3/Al$ 2D, 12HSW	$ZrC+ZrB_2$ $+1$-30% Zr
Density, kg/m^3	2890-3610	3560	3380	-	-	
Youngs Modulus, GPa	88-304	301	324	-	-	
Shear Modulus, GPa	41-123	-	-			
Flexural strength (4 point) MPa	45-525 (3 pt bend test)	312 (WM§ 20)	334 (WM 22)	720±150 (Max 880)	540±60 (Max 620)	800-1000
Fracture toughness $MPa\sqrt{m}$	2.9-9.5	5.9	6.9	27±3 (max 29)	15±1 (max 16)	16-23
Compressive strength MPa	414-2100	-	-	-	-	
Poisson's ratio	0.137-0.312	-	-			
Vickers Hardness, GPa at 700°C	1.41-15.0	8.3 4.9	6.4 3.7	-	-	78-75 (R_A Scale) 50
Thermal conductivity $Wm^{-1}K^{-1}$	11.8-39.6	36	82			
Coeff. of thermal expn. $\times10^6/K$	9.3-11.0	9.0	7.5			7
Dielectric constant ‖ to c-axis of Al_2O_3 ⊥ to c-axis of Al_2O_3	8.0 6.4					

† with variation in residual metal content
§ Weibull Modulus

Al$_2$O$_3$ particulates alter the properties marginally, whereas SiC continuous fibre reinforcements double the flexural strength and triple the fracture toughness values [41, 42, 44, 130]. For SiC or Al$_2$O$_3$ particulate reinforced composite, a weibull modulus of 20 is noteworthy. Additionally, retainment of hardness at elevated temperatures encourages select applications in diesel engine, such as valve seat insert [42]. AlN has several useful properties that are attractive from the application point of view. They include, low density, high Young's modulus, low thermal expansion coefficient (half that of Al$_2$O$_3$), good thermal shock resistance and favourable dielectric properties. Thus, the thermal and dielectric properties of AlN/Al composites are much superior compared to Al$_2$O$_3$/Al materials. AlN/Al composites obtained by nitridation of Al-10Mg alloy exhibit an elastic modulus between 180–240 GPa, flexural strength of 400 GPa and fracture toughness of 9.5 $MPa\sqrt{m}$ (Table 2.6). These properties are much higher compared to fully sintered AlN [65]. Al$_2$O$_3$ particulate reinforced AlN/Al has a modulus of 240 GPa, flexural strength of 340 MPa and a fracture toughness of 5.9 $MPa\sqrt{m}$. Further improvement in property can be achieved by decreasing the particle size and optimum aging of the residual metallic (alloy) matrix [83]. Al$_2$O$_3$ fibre reinforced composites are superior to particulate systems. However, as pointed out by Scholz *et al.*, the properties are strongly dependent on interfacial reaction layer thickness [88]. Furthermore, TiB$_2$ (55 *vol.*%) reinforced composites exhibit the same modulus as of AlN/Al materials but the properties, such as flexural strength and toughness are much higher. Compared to DI-MOX composites, the work that was carried out on mechanical properties of nitride systems is limited and more interest is envisaged in the near future.

Heredia *et al.* [131] measured the tensile and shear properties of an 8-harness satin weave Nicalon SiC fibre reinforced Al$_2$O$_3$/Al composite. The composite exhibited appreciable inelastic strain prior to failure caused by debonding and interfacial sliding. Due to the stress redistribution effect provided by the inelastic strains, the composite appears to be notch insensitive. Lin and Breder [132] studied the creep behaviour of SiC particulate reinforced alumina composites and found them to be comparable to SiC whisker reinforced composites

Table 2.6: Properties of AlN/Al composites[65,83,88,89,124].

Composite material	Flexural strength (MPa)	Fracture toughness ($MPa\sqrt{m}$)	Tensile strength (MPa)	Young's modulus (GPa)	Shear modulus (GPa)	Poisson's ratio	Thermal expansion ($10^{-6}K^{-1}$)	Thermal conductivity ($Wm^{-1}K^{-1}$)	Knoop hardness ($kgmm^{-2}$)
AlN/Al	366-400	9.5-11.1		180-240			8-11	~100	223-1124
AlN$_p$/AlN/Al	340	5.9		240					
TiB$_2{}_p$/AlN/Al	540	13.5		240					
Al$_2$O$_3$ $_P$/AlN/Al	340	9.5	242-457 286-506[†]	165-180	65-72	0.26-0.54			
Al$_2$O$_3{}_f$/AlN/Al	275±50[‡] 523±54[§]	8±1[‡] 10.74±2.1[§]							
SiC$_p$/AlN/Al							9.2-9.4		
Sintered AlN	280-350	3.3							1200

[†] naturally aged
[‡] with 0.4 μm reaction layer
[§] with 1.5 μm reaction layer

at $1200^{\circ}C$. The creep behaviour in these composites is attributed to grain boundary sliding accommodated by diffusional processes. Creep damage was initiated at multiphase grain junctions. Composites containing ZrB_2 platelets in a matrix of ZrC (with residual Zr varying between 1–20 $vol.\%$) offer excellent flexural strength (1 GPa) and fracture toughness (23 $MPa\sqrt{m}$). These properties are comparable with that of SiC fibre reinforced Al_2O_3/Al composites (Table 2.5). The residual unreacted Zr coupled with poor oxidation resistance of ZrC and ZrB_2 restrict high temperature application of these novel materials. However, components made out of these composite structures were successfully tested at temperatures up to $800^{\circ}C$ [41, 130].

Al_2O_3/Al and AlN/Al composites with predominantly a ceramic matrix are expected to exhibit superior tribological properties. To prevent the Al_2O_3 matrix from fracturing due to frictional loading, a larger volume fraction of Al_2O_3 is preferred. With increased metal content, the wear rate increases abruptly accompanied by fracture of the Al_2O_3 matrix [133]. Moreover, the friction coefficient of SiC particulate reinforced Al_2O_3/Al composite was superior to those of Al_2O_3 and Si_3N_4, and comparable to that of zirconia toughened alumina [134]. Apparently, wear begins to occur in these composites when the strain near in the subsurface due to frictional loading, exceeds the fracture strain of the alumina matrix.

2.4   Strengthening mechanisms

The processing aspects of both metal and ceramic matrix composites obtained *via in situ* reactions were discussed earlier. In this section, the strengthening mechanisms in these composites are briefly reviewed. Ceramic materials are inherently strong and have a high elastic modulus (E) due to the predominantly covalent bonding between atoms. Griffith [135] established the condition for fracture strength (σ_f) of a brittle material in plane stress condition as:

$$\sigma_f = \left(\frac{2E\gamma}{\pi c}\right)^{\frac{1}{2}} \tag{2.11}$$

where c is the half-length of the largest internal crack and γ is the free surface energy. By decreasing the flaw size, a higher strength can be achieved. For this reason, the objective of

ceramic processing for structural application is always to reduce flaw size. Due to its brittle failure behaviour, the resistance to crack propagation, i.e. the fracture toughness (K_{1C}) is a significant parameter. On the contrary, both strength and fracture toughness are relevant parameters in the case of MMSc.

The strength of MMCs is a very structure sensitive property. Processing induced thermal stresses and/or chemical reactions at the interface and matrix, make it impossible to predict the composite strength by any simple rule of mixture. The maximum strength attainable in fibre and whisker reinforced composites can be explained by the modified shear-lag theory. On the other hand, in the case of particulate reinforced composites, it appears that the matrix alloy (if age hardenable) and the processing induced substructural changes within the matrix (dislocation density increase) will have a greater influence on determining composite strength. Additionally, smaller increments in strength can be anticipated from grain size refinement, and texture. The final composite strength is usually the net contribution from several of the above mentioned points. The predominant strengthening mechanisms in MMCs are briefly discussed below as strengthening arising from the reinforcement and the matrix phase.

2.4.1   Reinforcement strengthening mechanisms

(a) Dispersion strengthening

The strengthening due to interaction of dislocations with small precipitate particles has been described as the Orowan strengthening effect. In case of hard incoherent precipitates within a ductile matrix, the stress (τ) required for a dislocation to circumvent a particle leaving behind a dislocation loop surrounding the particle is given by the modified Orowan relation [136]:

$$\tau = \frac{0.83G\mathbf{b}}{2\pi\sqrt{1-\nu}}\frac{1+l/\lambda}{\lambda}\ln\left(\frac{d}{r_o}\right) \qquad (2.12)$$

where $\mathbf{b}$ is the burgers vector, G is the shear modulus, ν is the poisson ratio of the matrix, l is the particle length, λ is the inter-particle spacing, d is the spacing between dislocations and r_o ($\approx 4\mathbf{b}$) is the inner cut-off radius of the dislocation. The dislocation loop surrounding

the dispersoid, further increases the stress required for the next dislocation to circumvent the particle. The predicted strength enhancement is usually less than an order of magnitude of the experimentally observed yield strength values.

(b) Modified shear-lag theory

The modified shear-lag theory [137] was developed to explain the similarity in proportionality limit between the composite and matrix alloy, and the anisotropic behaviour in whisker reinforced composites. The theory takes into account the transfer of load from the matrix to the reinforcement by shearing, such that a larger fraction of the load is borne by the fibre. For short fibre lengths and particulate reinforcements, the tensile transfer of load at the ends cannot be ignored, since it significantly affects the predicted composite strength. The composite yield strength is expressed in terms of the matrix and fibre volume fraction V_m and V_f, respectively as:

$$\sigma_{cy} = \sigma_{my} \left[\frac{1}{2} V_f (S + 2) + V_m \right] \tag{2.13}$$

where S is the fibre aspect ratio. When the composite load exceeds that of the matrix yield strength (σ_{my}), the matrix phase far from the reinforcement begins to plastically deform. Thus, the composite has a proportionality limit similar to that of the matrix alloy. The model has been successfully used to predict yield stress, ultimate tensile strength and creep strain rate in fibre and whisker reinforced composites. The model fails when the aspect ratio of the reinforcement is small or the fibres are misoriented.

2.4.2 Matrix strengthening mechanisms

(a) Residual elastic stress

The theoretical model for thermal residual stress of an unidirectionally aligned ellipsoidal reinforcement dispersed composite is based on continuum mechanics [138]. The difference in coefficient of thermal expansion (CTE) between the matrix and the reinforcement causes residual tensile stress within the matrix phase surrounding the reinforcement. For this reason

the model predicts a higher compressive yield stress than tensile yield stress. Additionally, the longitudinal residual stress is greater than the transverse residual stress. Experimental results (based on X-ray and Neutron diffraction) obtained from SiC whisker reinforced Al have confirmed the presence of such stresses. The predicted tensile and compressive yield strength are less than the experimentally obtained values by $\sim 10\ MPa$. This is because the model does not take into account the matrix strengthening due to dislocation punching. Finally, for a spherical SiC reinforcement, a difference in compressive and tensile yield strength of $\sim 13\ MPa$ was observed, while the model predicts them to be equal.

(b) High dislocation density

The strengthening model based on dislocation density assumes that the matrix material is strengthened above that of annealed wrought alloy by the presence of SiC fibres or particulates within the composite. The relatively large difference in CTE between SiC and Al (1:10) would result in substantial stresses during cooling and lead to dislocation generation at the particle–matrix interface [139]. Arsenault and Shi [140] were able to predict an increase in dislocation density (ρ) according to:

$$\Delta\rho = \frac{\Delta\alpha\Delta TNA}{\mathbf{b}} \tag{2.14}$$

where $(\Delta\alpha\Delta T)$ is the thermal misfit strain, $\mathbf{b}$ is the burgers vector, N is the number of particles and A is the total surface area of the particles. The matrix strength increment due to dislocation density (ρ) is governed by the relation [141]:

$$\Delta\sigma_{my} = \alpha G\mathbf{b}\sqrt{\rho} \tag{2.15}$$

where α is a constant (0.5–1.0) and G is the matrix shear modulus. Experimental evidence for dislocation generation has been observed by $in\ situ$ high voltage electron microscopy on cooling an SiC/Al composite foil from 500^oC to room temperature [142]. The model successfully predicts the strength and elastic modulus of the composite but fails to explain the anisotropic behaviour of whisker reinforced composites.

(c) Strengthening from grain size refinement

The presence of reinforcement particles was found to refine the grain size of the matrix alloy, by increasing the nucleation sites and inhibiting grain growth. The matrix strengthening due to grain size refinement can be estimated using Hall–Petch relation [143,144]:

$$\Delta\sigma_{ym} \approx \beta/\sqrt{D} \qquad (2.16)$$

where D is the grain size and β is a constant. In practice, the increase is only of a few tens of MPa.

2.5 Toughening mechanisms

Alloys processed *via* any one of the *in situ* processes finally yield a composite structure, wherein the metal and ceramic phases are uniformly dispersed. In some composites, interconnected metal ligaments (usually of 1–4 μm diameter) are present even when a third phase is present as a filler material. Fracture toughness is a material property, physically represented as a measure of resistance to crack propagation. Such measurements have been carried out with some success in many brittle composites. In the following sections, the toughening mechanisms in metal and ceramic matrix composites are briefly reviewed.

2.5.1 Toughening in metal-dispersed ceramic composites

Recent work on toughening mechanisms is focused on composites with dispersion of isolated metallic particles [145–151]. In these systems, the toughness increment is from moderate to very high (approximately 30–60 *vol.%* of the matrix), depending on the system and processing conditions [148–150]. Although there is limited information on toughness of oxide/nitride systems, there exists a consensus that the toughness is due to the dispersed metal ligaments within the ceramic matrix. The clamping force exerted by the metal ligaments bridge the crack faces and contribute to the toughness increment of the composites [152–154].
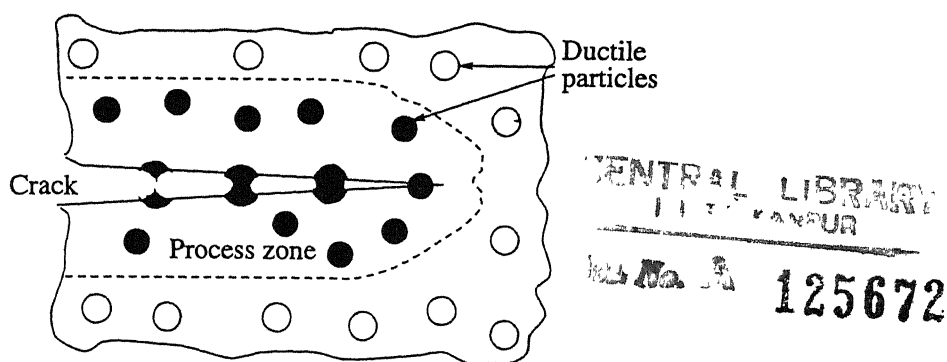
Figure 2.14: Schematic diagram showing crack bridging mechanism in metal dispersed ceramic composite. The work of stretching contributes to the toughness of the composite[151].

In these systems, the metal particles remain elastic until a crack approaches. As the crack advances, the particle surface is subjected to plastic deformation, but the particle itself remains intact by bridging the material even after the crack circumvents the particle (Figure 2.14). Subsequently, stretching of the metal occurs by plastic flow, ultimately resulting in total failure of the particle. The extensive plastic deformation of the bridging particles before fracture contributes to substantial toughening. To improve the overall toughness of the composites, ductile reinforcements of high strength are desirable [152–154]. Further, if the particles are weakly bonded to the matrix, there is a tendency to pull-out as the crack approaches with minimum increment in toughness. Alternatively, if the interface is strong, the crack passes through by stretching the particles. Depending on the degree of bonding between matrix and reinforcement, the toughness varies drastically. Furthermore, toughness also appears to depend on the particle size [155]. These criteria have been extensively analyzed taking model systems into consideration [151–153, 155]. In brief, a ductile reinforcement in a ceramic matrix contributes to toughening in two ways, namely crack bridging and crack shielding. The former contribution comes from higher work of fracture of large particles distributed in the matrix; whereas the latter is dominant when smaller particles with high yield strength are present.

An observation of indentation cracks in Al_2O_3/Al composites revealed that the fracture path is continuous in the ceramic matrix but intercepted by aluminum where it necks down to a chisel edge or a point, indicative of extensive crack bridging. Aluminum ligaments stretching up to 1 μm [152,156] were detected at distances as far as 160 μm behind the crack tip. In some

regions, matrix cracking is caused because of high stress exerted by deforming ligaments. Andersson and Aghajanian [130] developed a two-dimensional analytical model to describe fracture toughening in DIMOX composites and estimated the mean clamping stress(σ_m) as:

$$\sigma_m = \frac{f_m(t - 2R)E_m^n \sigma_y^{1-n}}{t} \ln\left(\frac{t}{t - 2R}\right) \qquad (2.17)$$

where f_m is the fraction of metal phase, $2t$ is the width of the undeformed metal ligament, R is the radius of the void in the metal, E_m is the elastic modulus of the metal, σ_y is the yield stress and n is a constant. Sigl $et\ al.$ [152] determined the plastic deformation of a metallic phase using a number of methods (finite element, slip line fields) and compared them with experimental data obtained on systems like Al_2O_3/Al and WC/Co. They concluded that a ductile phase having large uniaxial work of fracture and mean strain for hole initiation, richly contributes to the overall fracture toughness of the composite.

Pickard $et\ al.$ [157] measured toughness of DIMOX materials with or without SiC reinforcements. Higher strengths were obtained when SiC particulate preforms were used. Toughness increment observed with increasing particle size was attributed to frictional bridge effects (in addition to metal toughening). Even higher toughness values are predicted for composites with high aspect ratio. Furthermore, the residual metal (alloy) contribution to toughness can be enhanced by precipitation hardening.

2.5.2 Toughening mechanisms in ceramic-dispersed metal composites

In particulate reinforced metal matrix composites, toughness depends on a complex interaction between the constituent phases and the processing route employed [158]. They may be broadly classified as: (i) properties of the reinforcing phase, namely chemical nature, size, orientation and aspect ratio, (ii) properties of matrix alloy and (iii) processing route,such as distribution of reinforcement, level of porosity, segregation effects, etc. However, most metal matrix composites have ductile matrices which at the onset of fracture, exhibit localized crack tip plasticity [159]. In such systems, an energy dissipation technique, such as the J-integral was used to estimate the elastic strain energy released and the plastic energy

dissipated during crack the extension.
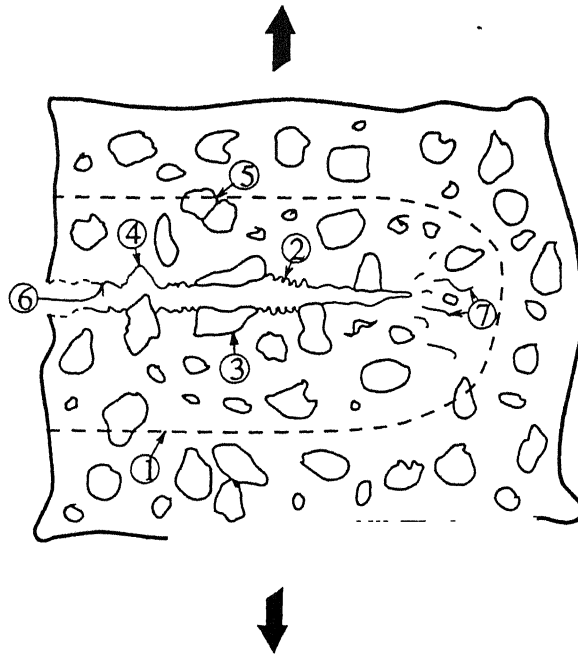
Figure 2.15: Energy absorption mechanisms in MMCs with discontinuous reinforcement[160]. For different mechanisms marked in the diagram refer to the text.

When a crack progresses through a particulate reinforced composite there are several mechanisms, which to a lesser or greater extent hinder the crack movement (Figure 2.15). Additionally, in fibre composites, fibre-matrix interface debonding may take place. Each of these mechanisms absorb energy, whereby requiring more work to be done by the external load [160]. They are: (1) deformation within plastic zone, (2) formation of voids along fracture surface, (3) fracture of reinforcement particles along crack path, (4) interfacial separation between matrix and reinforcement, (5) fracture of reinforcement particles within the plastic zone, (6) tortuous fracture path, increasing fracture surface area and (7) matrix crack near, but not continuous with the main crack.

When all other parameters are maintained constant, toughness increases with increase in size of the reinforcement. This is due to the presence of an extensive ductile matrix surrounding the larger diameter particles which enhance toughness through matrix plastic deformation [161]. Secondly, the presence of particulates alter the slip characteristics of the matrix by obstructing slip, limiting the operation of secondary dislocation sources and hindering cross-

slip. Finally, dispersoids limit the strain to fracture at the crack tip. The hard brittle particles within the plastic zone of the matrix undergo elastic deformation and decrease the work-to-fracture ratio in proportion to the reinforcement volume fraction. The elastic strain energy is released once the crack tip has passed. On the other hand, if the particle were to fracture, the energy of new surface formation is absorbed. However, the theoretical aspects of some of the above mentioned mechanisms are yet to be experimentally verified.

2.6 Applications

Two *in situ* methods, namely XD (Martin Marietta, U.S.A.) and DIMOX (Lanxide, U.S.A.) are being explored to manufacture various components in automobile and aerospace industries. DIMOX and PRIMEX processes offer composites of varying metal/ceramic ratio, with or without reinforcing materials. In these processes, a greater flexibility is achieved in tailoring properties from the view-point of applications. Keeping the advantages of the process (simplicity, flexibility and cost effectiveness) in mind, a large number of patents were filed based on liquid melt oxidation and nitridation [124]. In a recently published comprehensive report, methods for producing large, complex and thin shapes are briefly outlined [40]. Landini *et al.* [42] developed valve inserts using SiC and Al_2O_3 particulate reinforced Al_2O_3/Al composites which were successfully tested for 100 hours at full load operation on a single cylinder diesel engine. DIMOX composites exhibited superior wear resistance coupled with high hot-hardness. Also, components made out of SiC particulate reinforced Al_2O_3/Al composites (Alanx products, U.S.A.) were utilized for hydrocyclone cone liner and apexes. The performance of these composites were found to be superior (by up to 5 times) compared to conventionally used parts [162]. On similar lines, SiC (Nicalon) fibre reinforced Al_2O_3/Al composites (K_{1C} of 27 $MPa\sqrt{m}$ and σ_y of 880 MPa at room temperature) are projected as future materials for gas turbine applications [41]. The other suggested applications of these materials include wear parts for pumps, valves, chute liners, jet mill nozzles, heat exchangers, gun barrel liners, automobile parts (port liners, piston pins, etc.), armour, rocket engine components, electronic packaging, etc. [124] Unlike melt oxidized/reacted compos-

ites, XD materials can be subject to conventional metal working techniques to modify the microstructures and properties. XD materials are now being examined as potential structural materials for space applications [124].

Another recently developed family of materials perceived to have good application is the ZrB_2 platelet reinforced ZrC with varying residual Zr. These composites possess good electrical conductivity and complex shapes can be easily machined using electrical discharge machining (EDM). Further, components fabricated from these composites were successfully tested in solid fuel rocket engine at 800^oC. Presently, applications are limited to temperatures below 1000^oC due to their poor creep and oxidation resistance [41].

2.7   Summary and Scope of present work

In the recent past, several *in situ* methods have been developed to obtain metal/ceramic composites, which have potential to replace conventional materials. For clarity, these processes are classified based on reactant phases. They are liquid-liquid (sol-gel), liquid-gas (DIMOX and PRIMEX), liquid-solid (Zr-ZrC/ZrB_2 composites, Reaction metal penetration and mixed salt reactions), solid-gas (reduction of oxides) and solid-solid (SHS, Reaction sintering and XD) reactions. While many of these processes are confined to laboratory, a few are well developed to produce near net-shape components. In composite microstructures obtained by liquid-gas reactions, metallic and ceramic phases are interconnected three-dimensionally, usually with a preferred growth orientation. Further, oxidation/nitridation processes result in 'multiphase' structures by incorporating a variety of continuous/discontinuous reinforcements. Additionally, a flexible process, such as directed melt nitridation is capable of producing microstructure of two extremes, namely metal matrix and ceramic matrix composites.

Unlike directed melt oxidation, the microstructural development during composite growth in Nitrogen atmosphere in not well understood. Though composite microstructures with SiC, AlN, Al_2O_3 and TiB_2 have been shown to be possible, a systematic study on the influence of process variables and ensuing composite properties has not been attempted. A better

understanding of the process variables that influence the proportion of the Al and AlN in the matrix is desired. The residual aluminum in these composites restricts their application to low temperatures. Therefore, conversion of aluminum to a high temperature phase is desirable. Lastly, no mathematical model to predict the composite growth is reported in literature.

In the present study, several aluminum rich binary, ternary and quarternary alloys were nitrided to document the influence of processing variables on nitride formation. The processing variables examined from the viewpoint of nitridation are: Si content, process temperature and time. Further, nitridation experiments were interrupted at different stages to understand the nitridation mechanism. Optimizing the nitridation and infiltration characteristics, Al-2Si-8Mg alloy was chosen for infiltration studies in porous SiC preforms. The infiltration kinetics and microstructural development of SiC reinforced AlN/Al composites were studied as a function of process temperature, reinforcement size and shape. Additionally, the composites processed under the above conditions were mechanically characterized and compared with AlN reinforced AlN/Al composites.

The major drawback of SiC/AlN/Al composites is the residual aluminum. Aluminum softens at high temperatures and limits the use of the component to below $500^{\circ}C$. In order to convert the aluminum in matrix to a high-temperature phase, infiltration experiments were carried out through intermetallic (Nickel aluminide) preform at various temperatures. The microstructural development and mechanical properties of various intermetallic reinforced composites were assessed. Lastly, a mathematical model based on porous-bed phenomenon was developed to predict the composite growth. The influence of particle size and void fraction on infiltration rate were numerically assessed.

References

[1] F. S. Glasso, Unidirectionally solidified eutectics for optical-electronic and magnetic applications, *J. Met.*, **19** (1967) 17–21.

[2] H. Weiss, Electromagnetic properties of eutectic composites, *Metall. Trans.*, **2** (1971) 1513–1521.

[3] E. F. Bradley, *Superalloys: A Technical guide*, ASM International, Metals Park, Ohio, U.S.A (1988) 122.

[4] D. H. Duhl, Single crystal superalloys, In *Superalloys, supercomposites and superceramis*, ed. J. K. Tien and T. Caulfield, Materials Science and Technology series, Academic press, San Diego, U.S.A. (1989) 149–182.

[5] M. McLean, *Directionally solidified materials for high temperature service*, The Metals Society, London U.K. (1983) 55–106.

[6] W. A. Tiller, *Liquid metals and solidification*, American Society of Metals, Cleveland, Ohio, U.S.A. (1958) 256.

[7] K. A. Jackson and J. D. Hunt. Lamellar and rod eutectic growth, *Trans. Metall. Soc. AIME*, **236** (1966) 1129–1142.

[8] E. R. Thompson and F. D. Lemkey, Unidirectional solidification of Co-Cr-C monovariant eutectic alloys, *Metall. Trans.*, **1** (1970) 2799–2806.

[9] R. J. E. Glenny, J. E. Northwood and A. Burwood-Smith, Materials for gas turbines, *Int. Metall. Rev.*, **20** (1975) 1–28.

[10] G. H. Gessinger, Recent developments of powder metallurgy of superalloys, *Powder Metall. Int.*, **13** (1981) 93–101.

[11] E. Elliot, *Eutectic solidification processing: Crystalline and glassy alloys*, Butterworths, London, U.K. (1983) 308–347.

[12] F. D. Lemkey and S. G. Fishman, Insitu composites: Fabrication, In *Concise Encyclopedia of Composite Materials.* ed. A. Kelly, Pergamon press, Oxford (1989) 147–150.

[13] K. K. Chawla, *Composite materials: Science and Engineering*, Springer-Verlag, New York, U.S.A. (1987) 164.

[14] J. Bevk, W. A. Sunder, G. Dublon and D. E. Cohen, Mechanical properties of Copper based composites with insitu formed ultrafine filaments, In *Insitu Composites IV*, ed. F. D. Lemkey, H. E. Cline and M. McLean, Elsevier, New York, U.S.A. (1982) 121–133.

[15] J. D. Verhoeven, F. A. Schmidt, E. D. Gibson and W. A. Spitzig, Copper-refractory metal alloys, *J. Met.*, **9** (1986) 20–24.

[16] T. H. Courtney, Strengthening behaviour on insitu composites, In *Metal Matrix Composites: Mechanisms and Properties*, ed. R. K. Everett and R. J. Arsenault, Academic press, London, U.K. (1991) 101–131.

[17] N. J. Grant, A look at dispersion strengthening of powder metallurgy methods, In *Progress in Powder Metallurgy*, vol. 16, Metal Powder Industries Federation, New York, U.S.A. (1970) 99.

[18] N. C. Kothari, Dispersion hardening by Powder Metallurgy, In *Sintered Metal-Ceramic Composites*, ed. G. S. Upadhyaya, Elsevier publishers, Amsterdam, Netherland, (1984) 71–85.

[19] R. L. Graham, D. A. Edge and D. C. Moore, *Dispersion-hardened Copper and chemically prepared powders: Copper and its alloys*, The Institute of Metals, London U.K. (1970).

[20] A. V. Hoffman and C. L. Mantell, Mechanism of co-deposition of alumina with electrolytic copper, *Trans. Metall. Soc. AMIE*, **236** (1966) 1015–1019.

[21] W. A. Cense, M. Klerk and W. Albers, Aligned insitu growth of fibrous Ni-Nb$_2$O$_5$ composite by preferential internal oxidation, *J. Mater. Sci.*, **12** (1977) 2184–2188.

[22] E. Orowan, In *Symposium on internal stress in metals and alloys*, Institute of Metals, London, U.K. (1948) 451.

[23] J. W. Martin, *Micro-mechanism in particle hardened alloys*, Cambridge University press, Cambridge, U.K. (1980).

[24] L. M. Brown and R. K. Ham, Dislocation particle interaction, In *Strengthening methods in crystals*, ed. A. Kelly and R. B. Nicholson, Applied Science publishers, London, U.K. (1971).

[25] R. Lagneborg, Bypassing of dislocations past particles by climb mechanism, *Scripta Metall.*, **7** (1973) 605–614.

[26] E. Arzt and M. F. Ashby, Threshold stresses in materials containing dispersed particles, *Scripta Metall.*, **16** (1982) 1285–1290.

[27] E. Arzt and J. Schroder, Weak beam studies of dislocation/dispersoid interaction in an ODS superalloy, *Scripta Metall.*, **19** (1985) 1129–1134.

[28] E. Arzt and D. S. Wilkinson, Threshold stress for dislocation climb over hard particles: The effect of an attractive interaction, *Acta Metall.*, **34** (1986) 1893–1898.

[29] J. Rösler and E. Arzt. A new model-based creep equation for dispersion strengthened materials, *Acta Metall.*, **38** (1990) 671–683.

[30] M. J. Koczak and M. K. Premkumar, Emerging technologies for the in-situ production of MMC's, *J. Met.*, **45** (1993) 44–48.

[31] M. K. Premkumar and M. G. Chu, Synthesis of TiC particulates and their segregation during solidification in in-situ processed Al-TiC composites, *Metall. Trans.*, **24A** (1993) 2358–2362.

[32] M. J. Koczak and K. S. Kumar, U.S. Patent No. 4808372, March 1989.

[33] G. M. Scamans and E. P. Butler, In situ observations of crystalline oxide formation during aluminum and aluminum alloy oxidation, *Metall. Trans.*, **6A** (1975) 2055–2063.

[34] M. H. Zayan, O. M. Jamjoom and N. A. Razik, High-temperature oxidation of Al-Mg alloys, *Oxid. Met.*, **34** (1990) 323–333.

[35] M. H. Zayan, Model for non-protective oxidation of Al–Mg alloys, *Oxid. Met.*, **34** (1990) 465–472.

[36] C. Lea and C. Molinari, Magnesium diffusion, surface segregation and oxidation in Al–Mg alloys, *J. Mater. Sci.*, **19** (1984) 2336–2352.

[37] C. N. Cochran, D. L. Belitskus and D. L. Kinosz, Oxidation of Aluminum-Magnesium melts in air, Oxygen, flue gas and carbon dioxide, *Metall. Trans.*, **8B** (1977) 323–332.

[38] M. S. Newkirk, H. D. Lesher, D. R. White, C. R. Kennedy, A. W. Urquhart and T. D. Claar, Preparation of Lanxide Ceramic matrix composites: Matrix formation by the directed oxidation of molten metals, *Ceram. Eng. Sci. Proc.*, **8** (1987) 879–885.

[39] V. Jayaram, Ceramic composites by melt oxidation, *Mater. Eng.*, **3** (1992) 247–259.

[40] N. Claussen and A. W. Urquhart, Directed metal oxidation, In *Concise Encyclopedia of Advanced Ceramic Materials*, ed. R. J. Brook, Pergamon press, Oxford, U.K. (1992) 124–129.

[41] G. H. Schiroky, A. W. Urquhart and B. W. Sorenson, Ceramic composites for gas turbine engines via a new process, Paper presented at *Gas Turbine and Aeroengine Congress and Exposition*, Toronto, Canada, June 4–8 (1989).

[42] D. J. Landini and H. D. Lesher, Ceramic composite valve seat inserts, In proceedings of 3rd *Int. Symp. on Ceramic Materials and components for Engines*, ed. V. J. Tennery, Las Vegas, U.S.A. (1988) 1536–1551.

[43] S. L. Swartz, D. R. White and L. E. Cross, Dielectric properties of Lanxide^{TM} Al_2O_3/Al composites, *J. Mater. Sci.*, **27** (1992) 3932–3938.

[44] P. Barron-Antolin, G. H. Schiroky and C. A. Andersson, Properties of fibre reinforced alumina matrix composites, *Ceram. Eng. Sci. Proc.*, **9** (1988) 759–766.

[45] E. Manor, H. Ni, C. G. Levi and R. Mehrabian, Microstructure evolution of $SiC/Al_2O_3/Al$ alloy composites produced by melt oxidation, *J. Am. Ceram. Soc.*, **76** (1993) 1777–1787.

[46] A. S. Nagelberg, Growth kinetics of Al_2O_3/metal composites from a complex alumina alloy, *Solid State Ionics*, **32/33** (1989) 783–788.

[47] V. S. R. Murthy and B. S. Rao, Microstructural development in the directed melt oxidized (DIMOX) Al-Mg-Si alloys, *J. Mater. Sci.*, **30** (1995) 3091–3097.

[48] M. Hanabe, V. Jayaram and T. A. Bhaskaran, Growth of Al_2O_3/Al composites from Al–Zn alloys, *Acta Metall. Materiala*, **44** (1996) 819–829.

[49] E. Breval, M. K. Aghajanian and S. J. Luszcz, Microstructure of Al_2O_3/Al composites made by directed oxidation of aluminum, *J. Am. Ceram. Soc.*, **73** (1990) 2610–2614.

[50] A. S. Nagelberg, S. Antolin and A. W. Urquhart, Formation of Al_2O_3/metal composites by the directed oxidation of molten Aluminum-Magnesium-Silicon alloys: Part II, Growth Kinetics, *J. Am. Ceram. Soc.*, **75** (1992) 455–462.

[51] S. Antolin, A. S. Nagelberg and D. K. Creber, Formation of Al_2O_3/metal composites by the directed oxidation of molten Aluminum-Magnesium-Silicon alloys: Part I, Microstructural development, *J. Am. Ceram. Soc.*, **75** (1992) 147–154.

[52] O. Salas, H. Ni, V. Jayaram, K. C. Vlach, C. G. Levi and R. Mehrabian, Nucleation and growth of Al_2O_3/metal composites by oxidation of aluminum alloys, *J. Mater. Res.*, **6** (1991) 1964–1981.

[53] K. C. Vlach, O. Salas, H. Ni, V. Jayaram, C. G. Levi and R. Mehrabian, A thermogravimetric study of the oxidative growth of Al_2O_3/Al alloy composites, *J. Mater. Res.*, **6** (1991) 1982–1995.

[54] A. S. Nagelberg, Observation on the role of Mg and Si in the directed oxidation of Al–Mg–Si alloys, *J. Mater. Res.*, **7** (1992) 265–268. .

[55] M. Sindel, N. A. Travitzky and N. Claussen, Influence of Magnesium–Aluminum spinel on the directed oxidation of molten aluminum alloys, *J. Am. Ceram. Soc.*, **73** (1990) 2615–2618.

[56] P. Xiao and B. Derby. Alumina/aluminum composites formed by the directed oxidation of aluminum using magnesia as a surface dopant, *J. Am. Ceram. Soc.*, **77** (1994) 1761–1770.

[57] P. Xiao and B. Derby, Alumina/aluminum composites formed by the directed oxidation of aluminum using sodium hydroxide as a surface dopant, *J. Am. Ceram. Soc.*, **77** (1994) 1771–1776.

[58] M. S. Newkirk, A. W. Urquhart, H. R. Zwicker and E. Breval, Formation of Lanxide ceramic composite materials, *J. Mater. Res.*, **1** (1986) 81–89.

[59] T. Debroy, A. Bandopadhyay and R. Roy, Oxide matrix composites by directed oxidation of a commercial Al–Mg alloy, *J. Am. Ceram. Soc.*, **77** (1994) 1296–1300.

[60] H. Schmaizried and W. Laqua, Multicomponent oxides in Oxygen potential gradients, *Oxid. Met.*, **15** (1981) 339–353.

[61] E. Breval and A. S. Nagelberg, Microstructure of an Al_2O_3/metal composite containing an Al_2O_3 filler material, *Mater. Res. Soc. Symp. Proc.*, **B2** (1989) 93–98.

[62] A. Guha and V. S. R. Murthy, Refinement of directed melt oxidized structures, *Bull. Mater. Sci.*, **19** (1996) 1117–1124.

[63] S. P. Dhandapani, V. Jayaram and M. K. Surappa, Growth and microstructure of Al_2O_3–SiC–Si(Al) composites prepared by reactive infiltration of SiC preforms, *Acta Matall. Materiala*, **42** (1994) 649–656.

[64] H. R. Muralidhar and V. Jayaram, Infiltration studies of Al_2O_3/Al composite into Al_2O_3 preforms by directed melt oxidation of Al–Zn alloys, Private communication.

[65] D. K. Creber, S. D. Poste, M. K. Aghajanian and T. D. Claar, AlN composite growth by nitridation of aluminum alloys, *Ceram. Eng. Sci. Proc.*, **9** (1988) 975–982.

[66] H. Scholz and P. Greil, Nitridation reactions of molten Al–(Mg,Si) alloys, *J. Mater. Sci.*, **26** (1991) 669–677.

[67] M. K. Aghajanian, J. T. Burke, D. R. White and A. S. Nagelberg, A new infiltration process for the fabrication of metal matrix composites, *SAMPE Q.*, **20** (1989) 43–46.

[68] Y. Kagawa, S. C. Khatri and M. J. Koczak, Directed nitridation of liquid aluminum alloy: Growth process and modeling, *Ceram. Eng. Sci. Proc.*, **14** (1993) 776–781.

[69] H. LeHuy and S. Dallaire, Effects of Si and Mg dopants on the kinetics of aluminum alloys nitridation, In *Proceedings of Ceramic and Metal Matrix Composites*, ed. H. Mostarhaci, Pergamon press, New York, U.S.A. (1989) 302–311.

[70] H. Scholz and P. Greil, Synthesis of high purity AlN by nitridation of Li-doped Al-melt, *J. Eur. Ceram. Soc.*, **6** (1990) 237–242.

[71] S. Kúdela and A. Schweighofer, Slovac Academy of Sciences, Bratislava (CSSR), 200–201.

[72] A. Schweighofer and S. Kúdela, High pressure nitrided of Al-Mg alloys, *Korové Materiály*, **15** (1977) 257–268.

[73] I. A. Aksay, C. E. Hoge and J. A. Pask, Wetting under chemical equilibrium and non-equilibrium conditions, *J. Phys. Chem.*, **78** (1974) 1178–1183.

[74] S.-Y. Oh, J. A. Cornie and K. C. Russel, Wetting of ceramic particulates with liquid aluminum alloys: Part I Experimental techniques, *Metall. Trans.*, **20A** (1989) 527–532.

[75] S.-Y. Oh, J. A. Cornie and K. C. Russel, Wetting of ceramic particulates with liquid aluminum alloys: Part II, Study of wettability, *Metall. Trans.*, **20A** (1989) 533–541.

[76] F. Delanny, L. Froyen and A. Deruyttere, The wetting of solids by molten metals and its relation to the preparation of metal matrix composites, *J. Mater. Sci.*, **22** (1987) 1–16.

[77] S. K. Rhee, Wetting of ceramics by liquid aluminum, *J. Am. Ceram. Soc.*, **53** (1970) 386–389.

[78] D. A. Weirauch, Jr. Interfacial phenomena involving liquid metals and solid oxides in the Mg-Al-O system, *J. Mater. Res.*, **3** (1988) 729–739.

[79] R. B. Bhagat, in *Interfaces in Metal Matrix Composites*, ed. A. K. Dhingra and S. G. Fishman, Met. Soc. AIME, U.S.A. (1986) 169–174.

[80] J. W. McCoy, C. Jones and F. E. Warner, Preparation and properties of cast ceramic/aluminum composites, *SAMPE Q.*, **19** (1988) 37–50.

[81] S.-Y. Oh, J. A. Cornie and K. C. Russel, Particulates wetting and metal-ceramic interface phenomena, *Ceram. Eng. Sci. Proc.*, **8** (1987) 912–919.

[82] B. S. S. Daniel, *Processing of MMC's/CMC's by directed melt nitridation*, M.E.(I) Thesis, I.I.Sc., Bangalore, June 1992.

[83] M. K. Aghajanian, M. A. Rocazella, J. T. Burke and S. D. Keck, Fabrication of metal matrix composites by a pressureless infiltration technique, *J. Mater. Sci.*, **26** (1991) 447–454.

[84] S. Das, T. K. Dan, S. V. Prasad and P. K. Rohatgi, Aluminum alloy-rice husk ash particle composites, *J. Mater. Sci. Lett.*, **5** (1986) 562–564.

[85] T. Choh, R. Kanmel and T. Oki, Wettability of graphite to liquid aluminum and the effect of alloying elements on it, *Z. Metallk.*, **78** (1987) 286–290.

[86] A. Banerji, P. K. Rohatgi and W. Reif, Role of wettability in the preparation of metal matrix composites, *Metallw. Techn.*, **38** (1984) 656–661.

[87] G. Ziegler, J. Heinrich and G. Wötting, Relationships between Processing, Microstructure and Properties of dense and reaction bonded Silicon nitride, *J. Mater. Sci.*, **22** (1987) 3041–3086.

[88] H. Scholz, R. Günther, J. Rödel and P. Greil, Formation of Al_2O_3 fibre-reinforced AlN/Al-matrix composites by Al(Mg)-melt nitridation, *J. Mater. Sci. Lett.*, **12** (1993) 939–942.

[89] C. Toy and W. D. Scott, Ceramic-metal composite produced by melt infiltration, *J. Am. Ceram. Soc.*, **73** (1990) 97–101.

[90] E. D. Rodeghiero, O. K. Tse and E. P. Giannelis, Interconnected metal-ceramic composites by chemical means, *J. Met.*, (1995) 26–28. .

[91] E. Breval, Z. Deng, S. Chiou abd C. G. Pantans, Sol-gel prepared Ni-alumina composite materials: Part I Microstructure and Mechanical properties, *J. Mater. Sci.*, **27** (1992), 1464–1468.

[92] C. J. Brinker and G. W. Scherer, Sol-gel Science, Academic press, San Diego, U.S.A., (1990).

[93] B. Roy and D. Chakravorty, Electrical conductance of silver nanoparticles grown in glass-ceramic, *T. Phys.: Condens. Matter*, **2** (1990) 9323–9334.

[94] S. Roy, A. Chatterjee and D. Chakravorty, Glass-metal nanocomposites in bulk form by sol-gel route followed by hot-pressing, *J. Mater. Res.*, **8** (1993) 689–692.

[95] S. Roy and D. Chakravorty, Resistivity of ultrafine Iron particles in a glass matrix, *Jpn. J. Appl. Phy.*, **32** (1993) 3515–3517.

[96] S. Matsuo and T. Inabe, Fabrication of $Al–Al_2O_3$ composites by substitutional reaction in fused alumina, *Tokyo Ceram.*, (1991) 222–223.

[97] M.L.Breslin, J.Ringnalda, J.Seeger, A.L.Marasco, G.S.Daehn and H.L.Fraser, Aluminum/Aluminum Co-Continuous Ceramic Composite (C^4) materials produced by solid/liquid displacement reactions: Processing kinetics and microstructure, *Ceram. Eng. Sci. Proc.*, **15** (1994) 104–112.

[98] R. E. Loehman, K. Ewsuk and A. P. Thomasia, Synthesis of $Al_2O_3–Al$ composites by reactive metal penetration, *J. Am. Ceram. Soc.*, **79** (1996) 27–32.

[99] K. G. Ewsuk, S. J. Glass, R. E. Loehman, A. P. Thomasia and W. G. Fahrenholtz, Microstructure and properties of $Al_2O_3–Al(Si)$ and $Al_2O_3–Al(Si)–Si$ composites formed by insitu reaction of Al with Aluminosilicate ceramics, *Metall. Trans.*, **27A** (1996) 2122–2129.

[100] Y. Gao, J. Jia, R. E. Loehman and E. G. Ewsuk, Transmission electron microscopy study of Al/Al$_2$O$_3$ composites fabricated by reactive metal infiltration, *J. Mater. Res.*, **10** (1995) 1216–1225.

[101] E. Breval and W. B. Johnson, Microstructure of platelet-reinforced ceramics prepared by the directed reaction of zirconium with boron carbide, *J. Am. Ceram. Soc.*, **75** (1992) 2139–2145.

[102] W. B. Johnson, T. D. Claar and G. H. Schiroky, Preparation and processing of platelet reinforced ceramics by the directed reaction of zirconium with boron carbide, *Ceram. Eng. Sci. Proc.*, **9** (1989) 588–598.

[103] T. D. Claar, W. B. Johnson, C. A. Andersson and G. H. Schiroky, Microstructure and properties of platelet-reinforced ceramics formed by the directed reaction of zirconium with boron carbide, *Ceram. Eng. Sci. Proc.*, **75** (1989) 599–609.

[104] W. B. Johnson, A. S. Nagelberg and E. Breval, Kinetics of formation of a platelet-reinforced ceramic composite prepared by the directed reaction of zirconium with boron carbide, *J. Am. Ceram. Soc.*, **74** (1991) 2093–2101.

[105] P. Davis, Development of cast aluminum MMC's, London Scandinavian Metallurgical Co. Ltd., U.K.

[106] C. A. Handwerker, U. V. Deshmukh and D. C. Cranmer, In *Metal and Ceramic Matrix Composites: Processing, Modelling and Mechanical behaviour*, ed. R. B. Bhagat, A. H. Clauer, P. Kumar and A. M. Ritter, The Minerals, Metals and Materials Society, (1990) 457-465.

[107] G. Qi, M. Hino and A. Yazawa, Experimental study on the reduction-diffusion process to produce Fe–Nd, Fe–Sm, Co–Nd and Co–Sm alloys, *Mater. Trans. JIM*, **31** (1990) 463–470.

[108] E. Ustundag, R. Subramanian, R. Vaia, R. Dieckmann and S. L. Sass, Insitu formation of metal-ceramic micro structures, including metal-ceramic composites, using reduction reactions, *Acta Metall.*, **41** (1993) 2153–2161.

[109] E. Ustundag, R. Subramanian, R. Dieckmann and S. L. Sass, Insitu formation of metal-ceramic micro structures in the Ni–Al–O system by partial reduction reactions, *Acta Metall.*, **43** (1995) 383–389.

[110] P. Franke and R. Dickmann, Thermodynamics of iron manganese mixed oxides at high temperatures, *J. Phys. Chem. Sol.*, **51** (1990) 49–57.

[111] Z. A. Munir, Synthesis of high-temperature materials by self-propagating combustion methods, *Am. Ceram. Soc. Bull.*, **67** (1988) 342–349.

[112] A. G. Merzhanov, I. P. Borovinskaya, A. N. Pitjulin, V. I. Ratnikov, K. L. Epishin and V. L. Kvanin, Method for making a composite, Patent no. US4988480 (U.S.A.), Jan. 1991.

[113] Z. A. Munir, Reaction synthesis processes: Mechanisms and characteristics, *Metall. Trans.*, **23A** (1992) 7–13.

[114] M. G. Lakshmikantha, A. Bhattacharya and J. A. Sekhar, Numerical modeling of solidification combustion synthesis, *Metall. Trans.*, **23A** (1992) 23–34.

[115] H. C. Yi and J. J. Moore, Self-propagating high-temperature (combustion) synthesis (SHS) of powder-compacted materials, *J. Mater. Sci.*, **25** (1990) 1159–1168.

[116] J.-P. Lebrat, A. Verma and A. E. Miller, Combustion synthesis of Ni$_3$Al and NiAl-matrix composites, *Metall. Trans.*, **23A** (1992) 69–76.

[117] Y. Choi, M. E. Mullins, K. Wijayatilleke and J. K. Lee, Fabrication of metal matrix composites of TiC–Al through self-propagating synthesis reaction, *Metall. Trans.*, **23A** (1992) 2387–2392.

[118] H. P. Li, S. B. Bhaduri and J. A. Sekhar, Metal-ceramic composites based on the Ti-B-Cu porosity system, *Metall. Trans.*, **23A** (1992) 251–261.

[119] H. J. Feng, J. J. Moore and D. G. Wirth, Combustion synthesis of ceramic-metal composite materials: The TiC–Al$_2$O$_3$–Al system, *Metall. Trans.*, **23A** (1992) 2373–2379.

[120] Z. A. Munir, The preparation of multiphase materials through Self-sustaining powder reactions, In *Sintering of multiphase Metal and Ceramic systems*, ed. G. S. Upadhyaya, Sci-Tech publication, U.S.A. (1990) 37–46.

[121] N. Claussen, R. Janssen and D. Holz, Reduction bonding of aluminum oxide (RBAO), *J. Ceram. Soc. Japan*, **103** (1995) 749–758.

[122] N. Claussen, D. E. Gracia and R. Janssen, Reduction Sintering of Alumina-aluminide alloys (3A), *J. Mater. Res.*, **11** (1996) 2884–2888.

[123] W. G. Fahrenholtz, K. G. Ewsuk, R. E. Loehman and A. P. Tomasia, Formation of structural intermetallics by reactive metal penetration of Ti and Ni oxides and Aluminides, *Metall. Trans.*, **27A** (1996) 2100–2104.

[124] D. Lewis III, Insitu reinforcement of metal matrix composites, In *Metal Matrix Composites: Processing and Interfaces*, ed. R. K. Everett and R. J. Arsenault, Academic press, London (1991) 121–150.

[125] R. Mitra, M. E. Fine, and J. R. Weertman, Chemical reaction strengthening of Al/TiC metal matrix composites by isothermal heat treatment at 913K, *J. Mater. Res.*, **8** (1993) 2370–2379.

[126] M. E. Fine, R. Mitra and J. R. Weertman, Interfaces in Al–TiC composites prepared by insitu processing, *Z. Metallk.*, **84** (1993) 282–285.

[127] R. Mitra, W. A. Chiou, J. R. Weertman, M. E. Fine and R. M. Aikin Jr, Relaxation mechanisms at the interface in XD^{TM} Al/TiC$_p$ metal matrix composites, *Scripta Metall. Materialia*, **25** (1991) 2689–2694.

[128] L. Wang and R. J. Arsenault, Interfaces in XD processed TiB$_2$/NiAl composites, *Metall. Trans.*, **22A** (1991) 3013–3018.

[129] M. K. Aghajanian, N. H. Macmillan, C. R. Kennedy. S. J. Luszcz and R. Roy, Properties and microstructure of Lanxide Al$_2$O$_3$–Al ceramic composite materials, *J. Mater. Sci.*, **24** (1989) 658–670.

[130] C. A. Andersson and M. K. Aghajanian, The fracture toughening mechanism of ceramic composites containing adherent ductile metal phases, *Ceram. Eng. Sci. Proc.*, **9** (1988) 621–626.

[131] F. E. Heredia, A. G. Evans and C. A. Andersson, Tensile and shear properties of continuous fibre-reinforced SiC/Al_2O_3 composites processed by melt oxidation, *J. Am. Ceram. Soc.*, **78** (1995) 2790–2800.

[132] H. Lin and K. Breder, Creep deformation in Alumina–Silicon Carbide composites produced via a directed metal oxidation process, *J. Am. Ceram. Soc.*, **79** (1996) 2218–2220.

[133] M. Sterntzkem, M. Knechtel, M. Hoffman, E. Broszeit and J. Rödel, Wear properties of alumina/aluminum composites with interpenetrating networks, *J. Am. Ceram. Soc.*, **79** (1996) 121–128.

[134] V. Jayaram, R. Manna, M. G. Kshetrapal, J. Sarkar and S. K. Biswas, Microstructure control and wear of Al_2O_3–SiC–(Al,Si) composites made by melt oxidation, *J. Am. Ceram. Soc.*, **79** (1996) 770–772.

[135] A. A. Griffith, The phenomena of rupture and flow in solids, *Phil. Trans. Roy. Soc. Lond.*, **A221** (1920) 163–165.

[136] P. M. Kelly, The quantitative relationship between microstructure and properties in two-phase alloys, *Int. Met. Rev.*, **18** (1973) 31–36.

[137] V. C. Nardone and R. M. Prewo, On the strength of discontinuous silicon carbide reinforced aluminum composites, *Scripta Metall.*, **20** (1986) 43–48.

[138] R. J. Arsenault and M. Taya, Thermal residual stresses in metal matrix composites, *Acta Metall.*, **35** (1987) 651–659.

[139] R. J. Arsenault and R. M. Fisher, Microstructure of fibre and particulate SiC in 6061 Al composite, *Scripta Metall.*, **17** (1983) 67–71.

[140] R. J. Arsenault and N. Shi, Dislocation generation due to difference between coefficients of thermal expansion, *Mat. Sci. Eng.*, **81** (1986) 175–187.

[141] N. Hansen, The effect of grain size and strain on the tensile flow stress of Al at room temperature, *Acta Metall.*, **25** (1977) 863–869.

[142] M. Vogelsang, R. J. Arsenault and R. M. Fisher, An Insitu HVEM study of dislocation generation at Al/SiC interfaces in metal matrix composites, *Metall. Trans.*, **17A** (1986) 379–389.

[143] E. O. Hall, The deformation and aging of mild steel: III Discussion and results, *Proc. Phys. Soc.*, **B64** (1951) 747–753.

[144] N. J. Petch, The cleavage strength of poly crystals, *J. Iron Steel Inst.*, **174** (1953) 25–28.

[145] C. O. McHugh, T. J. Whalen and M. Humenik Jr, Dispersion strengthened Aluminum oxide, *J. Am. Ceram. Soc.*, **49** (1966) 486–491.

[146] P. Hing and G. W. Groves. Strength and fracture toughness of polycrystalline magnesium oxide containing metallic particles and fibres, *J. Mater. Sci.*, **7** (1992) 427–434.

[147] A. V. Virkar and D. L. Johnson, Fracture behavior of ZrO_2–Zr composites, *J. Am. Ceram. Soc.*, **60** (1977) 514–519.

[148] V. V. Krstic, P. S. Nicholson and R. G. Hoagland, Toughening of glasses by metallic particles, *J. Am. Ceram. Soc.*, **64** (1981) 499–504.

[149] M. I. Mendelson and M. F. Fine, Enhancement of fracture properties of wustite by precipitation, *J. Am. Ceram. Soc.*, **57** (1974) 154–159.

[150] D. T. Rankin, J. J. Stiglich, D. R. Petrak and R. Ruh. Hot-pressing and mechanical properties of Al_2O_3 with an Mo–dispersed phase, *J. Am. Ceram. Soc.*, **54** (1971) 277–281.

[151] M. F. Ashby, F. J. Blunt and M. Bannister, Flow characteristics of highly constrained metal wires, *Acta Metall.*, **37** (1989) 1847–1857.

[152] L. S. Sigl, P. A. Mataga, B. J. Dalgleish, R. M. McMeeking and A. G. Evans, On the toughness of brittle materials reinforced with a ductile phase, *Acta Metall.*, **36** (1988) 945–953.

[153] A. G. Evans and R. M. McMeeking, On the toughening of ceramics by strong reinforcements, *Acta Metall.*, **34** (1986) 2435–2441.

[154] B. D. Flinn, M. Rühle and A. G. Evans, Toughening in composites of Al_2O_3 reinforced with Al, *Acta Metall.*, **37** (1989) 3001–3006.

[155] L. R. Thompson and R. Raj, Insitu stress–strain response of small metal particles embedded in a ceramic matrix, *Acta Metall. Materialia*, **42** (1994) 2477–2485.

[156] B. Budiansky, J. C. Amazigo and A. G. Evans, Small scale crack bridging and the fracture toughness of particulate reinforced ceramics, *J. Mech. Phys. Sol.*, **36** (1988) 167–187.

[157] S. M. Pickard, E. Manor, H. Ni, A. G. Evans and R. Mehrabian, The mechanical properties of ceramic composites produced by melt oxidation, *Acta Metall. Materialia*, **40** (1992) 177–184.

[158] C. M. Friend, Toughness in metal matrix composites, *Mater. Sci. Tech.*, **5** (1989) 1–7.

[159] T. J. Baker and D. R. Munasinghe, In *Metal Matrix Composites: Structure and Property assessment*, The Institute of Metals, London, U.K. Nov. 1987, Paper no. 26.

[160] D. L. Davidson, Fracture toughness of particulate metal matrix composites, In *Metal Matrix Composites: Mechanisms and Properties*, ed. R. K. Everett and R. J. Arsenault, Academic press, London, U.K. (1991) 217–234.

[161] Y. Flom and R. J. Arsenault, Fracture of SiC/Al composites, In 6th *Int. Conf. on Comp. Mater. and 2nd Eur. Conf. on Comp. Mater.*, vol. 2, Elsevier Applied Science, Barking, Essex, U.K. (1987) 189–198.

[162] J. Weinstein and B. Rossing, Application of a new ceramic/metal composite technology to form net shape wear resistant components, In *High Performance Composites for the 1990's*, ed. S. K. Das, C. P. Ballard and F. Marikar, The Minerals, Metals and Materials Society, U.K. (1990) 339–360.

Chapter 3

Experimental

3.1 Introduction

In this chapter, the experimental procedures adopted for the processing and characterization of reinforced AlN/Al composites are described in detail. A preliminary study of nitridation and infiltration kinetics of various binary and ternary alloys was undertaken before selecting an alloy for the purpose of infiltration. The chosen alloy was infiltrated into various forms of SiC, AlN and Nickel aluminide particulate preforms. The ensuing composites were characterized for their microconstituents and mechanical properties. Microstructural characterization to identify the various phases and their distribution was carried out using X-ray and electron/optical microscopy techniques. The mechanical property measurements carried out in the present work are: Vickers microhardness, four-point flexural strength and fracture toughness.

3.2 Composite processing

AlN/Al composites were formed by reacting molten aluminum alloys in a nitrogenous atmosphere. Special care was taken to maintain a very low Oxygen partial pressure in the reaction chamber. For studying the microstructural development in various alloys, nitridation experiments were interrupted at different time intervals. The quenched samples were

Table 3.1: Alloy compositions used in the present investigation.

Sr. No.	Nominal composition (wt.%)	Sr. No.	Nominal composition (wt.%)
1	Al–8Mg	7	Al–5Si–8Mg
2	Al–8Zn	8	Al–8Si–8Mg
3	Al–3Na	9	Al–2Si–2.3Li
4	Al–2.3Li	10	Al–2Si–8Mg–1Fe
5	Al–0.5Si–8Mg	11	Al–2Si–4Mg–4Zn
6	Al–2Si–8Mg		

cut parallel to the growth direction to examine structural variations using the Scanning Electron Microscope (SEM). For infiltration experiments, loose or sintered preforms were used. Spontaneous infiltration takes place when the porous preform is wet by the molten alloy. The infiltrated composites on cooling were found to be nearly dense.

3.2.1 Alloy preparation

Al, Si, Mg, Zn, Na and Li elements used for alloy preparation were of > 99.95% purity. For alloy preparation, a known amount of aluminum was melted in a clay-graphite crucible using a SiC resistance heated electric furnace. To arrive at a given alloy composition, the weight of each element was directly calculated from the required wt.%, taking into account the losses due to volatilization and oxide formation. Si was added at higher temperatures ($>1000^{\circ}C$) to ensure complete dissolution. The alloy melt was thoroughly degassed before adding the volatile alloying elements wrapped in aluminum foil. The melt was finally cast into cylindrical bars of 20 mm diameter. The compositions of these alloys are tabulated in Table 3.1.

3.2.2 Preform materials

The filler materials used in the present work and their sources are listed in Table 3.2. The preform was generally used as loose powder and in selected cases the powder was sintered be-

fore insertion into the crucible. Various forms of SiC reinforcements, namely fibres, platelets and particulates, were used to study the influence of filler material morphology on infiltration kinetics and mechanical properties. When SiC fibres were infiltrated, the bundle of fibre was arranged such that the fibre axis was aligned parallel to the infiltration direction.

Table 3.2: Details of reinforcing material used in this investigation.

Sr. No.	Reinforcing material	Supplier	Particle size (μm)
1	SiC particulate ($\alpha + \beta$)	Carborundum Universal, India	32–45 45–71 71–160
2	SiC platelets (β)	Millienium Technology Inc., USA	20–30
3	SiC short fibre (β)	Millienium Technology Inc., USA	5–10
4	SiC fibre (β)	Nippon Carbon, Japan	10–25
5	SiC monofilaments ($\alpha + \beta$)	AVCO speciality materials, USA	142 μm with a 6μm C-rich layer
6	AlN particulate	Elektroschmelzwerk Kempten, GmbH, Germany	3–20
7	Nickel Aluminide (Ni_2Al_3+$NiAl_3$)	Gesellschaft für Elektro-metallurgie, GmbH, Germany	45–80

While no chemical treatment was given to SiC fibres and platelets, additional processing was needed to remove residual carbon and surface oxide layer from SiC particulates. The SiC particulates were heated at $900^{\circ}C$ in air for 5 hours, to ensure complete oxidation of residual carbon. Later, the heat treated powder was washed with HF, followed by water, acetone and finally dried in an oven at $200^{\circ}C$.

For the infiltration experiments to study variation in particle size and temperature, sintered SiC particulate preforms were used. The acid washed SiC powder was mixed with a few drops of 2% polyvinyl acetate as binder. The binder mixed power was cold pressed in an 1" diameter die to a load of 20 kg/cm^2 and held for one minute. Later, the green compact was sintered in air at $1200^{\circ}C$ for 2 hours to provide adequate strength for handling and machining. The volume fraction of the pores was calculated from the weight of the sintered

powder compact. The nickel aluminide particulates used were of <100 μm size, with a composition of 50 $wt.\%$ Ni and Al. The composition lies within the Ni_2Al_3 and $NiAl_3$ two phase field in the Ni–Al phase diagram.

3.2.3   Crucible configuration

Pore free recrytallized alumina crucibles were made from 20 mm inner diameter hollow tubes (2 mm thick) supplied by Kumar Manufacturing Company, Calcutta. One end of the crucible was sealed with alumina paste and sintered at 1200^oC. A coating of zirconia was applied at the bottom to make the growth/infiltration unidirectional. Experiments were carried out in two configurations, *viz* with or without preform (Figure 3.1). For nitridation studies of base alloys, the metal billet was kept in the crucible and placed within the furnace. Whereas, for infiltration experiments, the preform was placed on top of the metal as shown in Figure 3.1b.
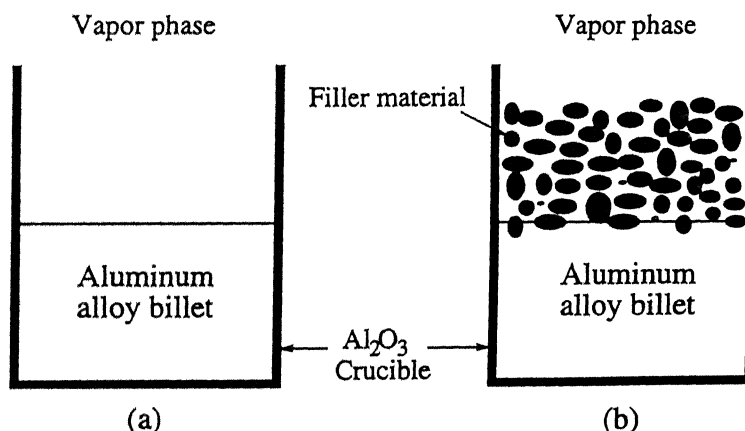
Figure 3.1: Schematic of crucible arrangement (a) without and (b) with preform.

3.2.4   Nitridation experiments

The experimental arrangement consisted of a tubular furnace in conjunction with a Nitrogen gas supply at the inlet, and a rotary pump at the outlet (Figure 3.2). The furnace has a pore free mullite tube of 50 mm inner diameter, heated externally by SiC heating elements. The furnace temperature was controlled by a 10 kV microprocessor base power controller.

The temperature was measured using a Pt–Pt-13%Rh (R type) thermocouple, placed within the furnace chamber in contact with the outside wall of the mullite tube.
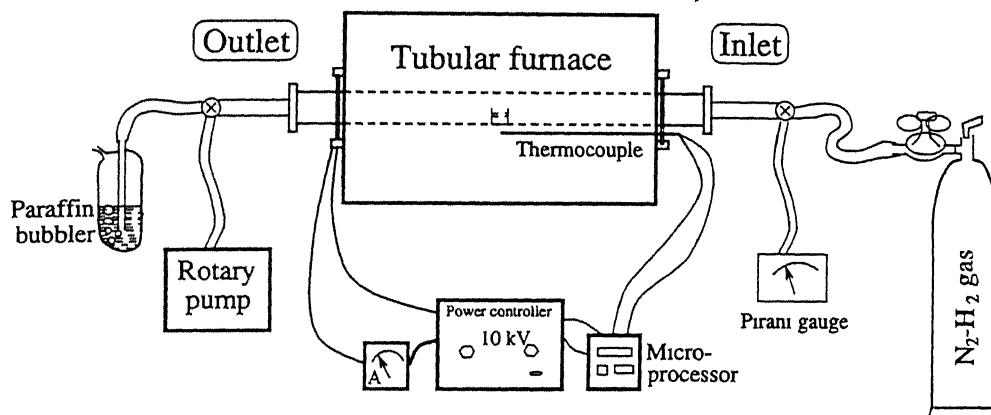
Figure 3.2: Experimental arrangement used for composite processing in Nitrogen atmosphere.

The furnace tube was calibrated against the external thermocouple under flowing gas conditions. There was a $35\pm3^{\circ}C$ temperature variation between the inside and outside wall of the furnace tube. The constant temperature zone extended to 30 mm on either side from the center of the tube. There was a temperature drop of $8^{\circ}C$ at the extremes of the constant temperature zone. The reaction gas consisted of a mixture of Nitrogen and 4% Hydrogen of high grade supplied by Indian Oil Limited, New Delhi. Hydrogen was required to maintain the atmosphere slightly reducing. A 3-way tap was employed at the outlet, to switch the outflow from the rotary pump to the paraffin column.

To begin an experiment, the sample containing crucible was weighed before placing in the constant temperature zone of the tubular furnace and sealed at both ends. The furnace chamber was evacuated and purged with the reaction gas three times before switching the outflow to the paraffin bubbler. A constant gas flow rate of $\sim$10 cm^3/min was maintained throughout the experiment. Once the gas flow has steadied, the furnace chamber was heated to the reaction temperature at the rate of 6 $^{\circ}C/min$. After the process duration, the furnace was cooled, and the sample was removed and weighed to calculate weight gain/loss.

3.2.5   Thermo Gravimetric Analysis (TGA)

The TGA analysis was carried out on selected alloys using a CAHN balance (model 171). The weight gain during nitridation and infiltration experiments was monitored to follow the reaction progress by continually measuring the sample weight. A 7 mm inner diameter recrystallized alumina crucible containing the sample was placed in a weighing bucket and suspended within the horizontal tubular furnace by a platinum wire. The crucible was covered with alumina wool to prevent the Mg vapour from contaminating the furnace tube. The balance arrangement was isolated from the furnace chamber by flowing Argon gas. The experimental start-up procedure and heating rate were the same as described previously. The sample weight and temperature were recorded at 10 second intervals, and stored in a personal computer for data analysis.

3.3   Microstructural characterization

3.3.1   X-Ray Diffraction (XRD)

XRD patterns were obtained from the powder sample composite materials using an X-ray diffractometer (Iso–Debyeflex 2002), having a Cu target (K$_\alpha$, λ=1.514Å). About 0.5 g of the reinforcement particle or infiltrated composite was ground to a fine powder in an alumina mortar and pestle. In case of alloy nitrided samples, a diamond file was used to file the requisite amount of powder. The settings used for X-ray diffraction are given in Table 3.3. The diffraction pattern was recorded on a strip chart recorder. Initially, a rapid scan was made from 20 to 120°C (2θ) to locate the position of the different peaks. In order to separate and identify overlapping peaks, a slower scan was employed.

3.3.2   Optical Microscopy

Samples for microstructural examination were sectioned using a slow speed isomet saw. The cold mounted samples were polished on a series of emery papers. The final polish was done

Table 3.3: XRD setting used for characterization of powder samples.

Parameter	Scan	Setting
Voltage	–	30 kV
Current	–	20 mA
Scanning speed (2θ)	rapid	$3^o/min$
	slow	$0.6^o/min$
Chart speed	rapid	12 mm/min
	slow	15 mm/min
Time constant	–	10 s
Counts/min	rapid	10 K
	slow	variable

with one micron diamond, followed by 0.05 micron alumina. An optical microscope (Leitz) was used for preliminary microstructural examination. A better contrast between ceramic and metallic phases was obtained in optical micrography.

3.3.3 Scanning Electron Microscopy (SEM)

The SEM (JSM 840A, JEOL) was used for a variety of purposes including microstructural characterization and fractography. Samples were coated with silver to avoid charging. For microstructural observation, the back scattered mode was preferred to enhance the contrast between the ceramic and metallic phases. On the other hand, the secondary mode was preferred for observation of fracture features. In selected cases, compositional analysis was carried out using the Energy Dispersive X-ray microanalyer (EDAX) associated with the SEM.

3.3.4 Transmission Electron Microscopy (TEM)

Since the composite contains a brittle reinforcement dispersed in a ductile matrix, special care was required in sample preparation. Initially, 0.3 mm thick slices were cut from the infiltrated composite on a slow speed Isomet saw. The flat samples were mechanically thinned down to ~0.1 mm thickness on 600 grid emery paper, from which 3 mm disc specimens were punched.

These specimens were then dimpled to ~ 40 μm thickness on a dimpler, using one micron diamond paste as the grinding medium. The dimpled disc samples were further thinned using an ion beam thinning machine. The ion beam thinning unit was operated under the following conditions for 80 to 120 hours, until the sample became electron transparent.

Gun voltage	4 kV
Beam inclination	10–15°
Gun current	5–40 μA (dc)
Gas	Ar (high purity)

3.4 Mechanical testing

The mechanical tests performed on the composite were microhardness, flexural strength and fracture toughness. The flexural strength and fracture toughness were carried out in an Instron 1195 machine, using a 4-point bending fixture with 4 mm and 10 mm inner and outer spans, respectively. A constant (slowest) cross-head speed of 50 $\mu m/min$ was maintained for all tests until failure occurred.

3.4.1 Vickers Microhardness

Microhardness measurements (Leitz, Miniload 2) were carried out in case of aluminide reinforced samples to measure the hardness variations in the matrix, as well as reinforcement phase. The test was performed by dropping a loaded diamond indentor (10–50 g) on the different phases. In each case, on an average at least 10 readings were taken.

3.4.2 Flexural strength

Flexural strength measurements were carried out on a brass 4-point fixture with cylindrical steel pins at the inner and outer span positions. Rectangular beam specimens of 3.5×2.5×14 mm dimension were cut using an Isomet diamond saw and the surfaces were polished to 1 micron finish. Each sample was placed in the fixture as shown in Figure 3.3 and loaded in

an INSTRON 1195 machine. The load *vs.* displacement data was recorded on a strip chart. The flexural strength was calculated according to the expression:

$$\sigma_y = \frac{3P}{bw^2}\left(\frac{d_2 - d_1}{2}\right) \tag{3.1}$$

where P is the load at failure, b is the breadth, w is the width of the beam, and d_1 and d_2 are the inner and outer span lengths, respectively, of the 4-point jig.

3.4.3 Fracture toughness
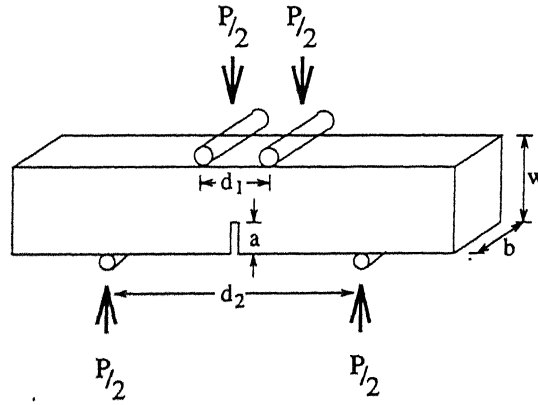
Figure 3.3: Schematic of four-point testing arrangement to measure strength and toughness of beam specimens.

For toughness (K_{1c}) measurements, in addition to the sample preparation for flexural strength, a notch roughly one-third of sample width (w) was introduced mid-span using the Isomet saw. The sample is placed in the 4-point fixture as shown in Figure 3.3, such that on loading the notched face will be in tension. The fracture toughness was calculated using the following expression:

$$K_{1c} = \frac{3Pa^{1/2}}{bw^2}\left(\frac{d_2 - d_1}{2}\right)\left[3.86 - 6.15\left(\frac{a}{w}\right) + 27\left(\frac{a}{w}\right)^2\right]^{1/2} \tag{3.2}$$

where a is the notch depth and the other terms are similar to those in Equation 3.1.

3.5 Mathematical modelling

A FORTRAN 77 code was developed to model the liquid rise phenomenon through porous ceramic preforms. The program uses a forward difference technique, to calculates flow velocities and pressure values at uniformly spaced grid points within the computational domain. The fluid flow part of the code is based on the Algorithm (SIMPLE) developed by Patankar and Spalding [1]. The solution procedure marches forward in time, treating the unsteady state equations as quasi-steady. Further details of the numerical procedure are provided in chapter 6.

References

[1] S. V. Patankar and D. B. Spalding, A calculation procedure for Heat, Mass and Momentum transfer in three-dimensional parabolic flows, *Int. J. Heat Mass Transfer*, **15** (1972) 1787–1792.

Results and Discussion

Chapter 4

Nitridation of Aluminum Alloys

4.1   Introduction

Nitridation of aluminum rich alloys was carried out in N_2-4%H_2 atmosphere under varying process conditions. The process variables examined in the present study include, alloy composition, nitridation temperature and time. To understand the nitridation mechanism, the process was interrupted periodically to observe the macro and microstructural development. On each alloy sample, the weight gain measurement was used to discern the amount of nitride that had formed. The difference in weight, before and after the experiment, include both the weight loss due to escape of volatile elements and weight increase caused by *in situ* AlN formation. Further, thermo-gravimetric analysis (TGA) was carried out on selected Al–Si–Mg alloys to understand the influence of Si on nitridation.

The surface of the nitrided samples were microscopically observed to study the external growth morphology. A vertical section parallel to the growth direction of the nitrided sample was examined to reveal internal nitride formation beneath the surface layer. The microstructural observations were correlated to the weight gain measurements. A small portion of the sample was ground to fine powder for X-ray analysis to qualitatively identify the phases present.

Results

4.2 AlN/Al composite formation in Al alloys

4.2.1 Binary alloy nitridation

To characterize the nitridation behaviour in binary alloys, Al-8Mg, Al-8Zn, Al-3Na and Al-2.3Li alloys were nitrided at 1050°C. The choice of alloy was made ensuring that the minor constituent is volatile at the process temperature to serve as an Oxygen gettering agent. The normalized weight gain/loss of alloys nitrided at different temperatures for various durations are presented in Table 4.1. The negative values in weight is due to the excessive weight because of Mg evolution. The nitride formation can be perceived by comparison of weight gain data. Both Al-8Mg and Al-8Zn alloys registered continual weight loss with increase in

Table 4.1: Nitridation data of Binary alloys.

Alloy composition (wt.%)	Process temperature (°C)	Process duration (hrs)	Normalized wt. gain (g/cm²)
Al-8Mg	1050	24	−0.084
		40	−0.113
	1150	24	−0.107
Al-8Zn	1050	24	−0.104
		40	−0.147
	1150	24	−0.209
Al-3Na	1050	24	−0.050
Al-2.3Li	1050	24	+0.025

nitridation temperature and process duration. On the contrary, Al-3Na and Al-2.3Li alloys exhibited marginal to substantial weight increase after nitridation for 24 hours at 1050°C.

The role of Mg as a deoxidant is confirmed by the presence of MgO (as fine particle or sponge) on the alloy surface and walls of the crucible. Often the sponge consisted of fine fibres. These fibres were polycrystalline in nature of 1–2 μm in diameter (Figure 4.1). Mg was identified using EDAX. Similar features were not distinctly observed in the alloys containing other solute atoms. This is because the vapour is carried away by the flowing gas and

deposited elsewhere in the furnace chamber. Further nitridation was not observed, due to a passivating surface nitride layer formation on Al-8Mg and Al-8Zn alloys. The morphology of the surface nitride layer is shown in Figure 4.2(a&b). A cross-section revealed a surface nitride layer of <20 μm thick, which is presumably non-porous and obstructs the access of the underlying metal to the nitriding atmosphere. Hence, the AlN/Al composite growth is inhibited. On the contrary, no passivating nitride layer was formed on the Al-3Na and Al-2.3Li alloy surfaces. The unstable surface nitride layer permits continued interaction between the molten metal and the reaction gas. This is particularly evident by the AlN whisker like growth on the surface of Al-3Na and Al-2.3Li alloys, when nitrided at $1050^{o}C$ for 24 hours (Figure 4.2(c&d)). X-ray analysis carried out on ground powder taken from the surface of the composite confirmed the presence of hexagonal AlN of the wurtzite structure (Figure 4.3). The presence of Al was also identified in the nodules grown on the Li containing alloy.

The cross-section of the nitrided Al-3Na and Al-2.3Li alloys are shown in Figure 4.4. Since the nitrided surface layer is non-passivating in these alloys, continued reaction leads to formation of large isolated AlN crystals, well below the surface nitride layer, indicative of inward growth of AlN (Figure 4.4(c&d)). However, there is only limited outward growth above the surface AlN layer.

4.2.2 Nitridation of Si containing alloys

The nitridation behaviour of various ternary alloys, particularly with small amounts of Si added to the binary alloys examined earlier are studied. The influence of process parameters, such as temperature and time, on the nitride formation is also presented. But first, the nitridation mechanism is elucidated by treating the Al-2Si-8Mg alloy as a model system.
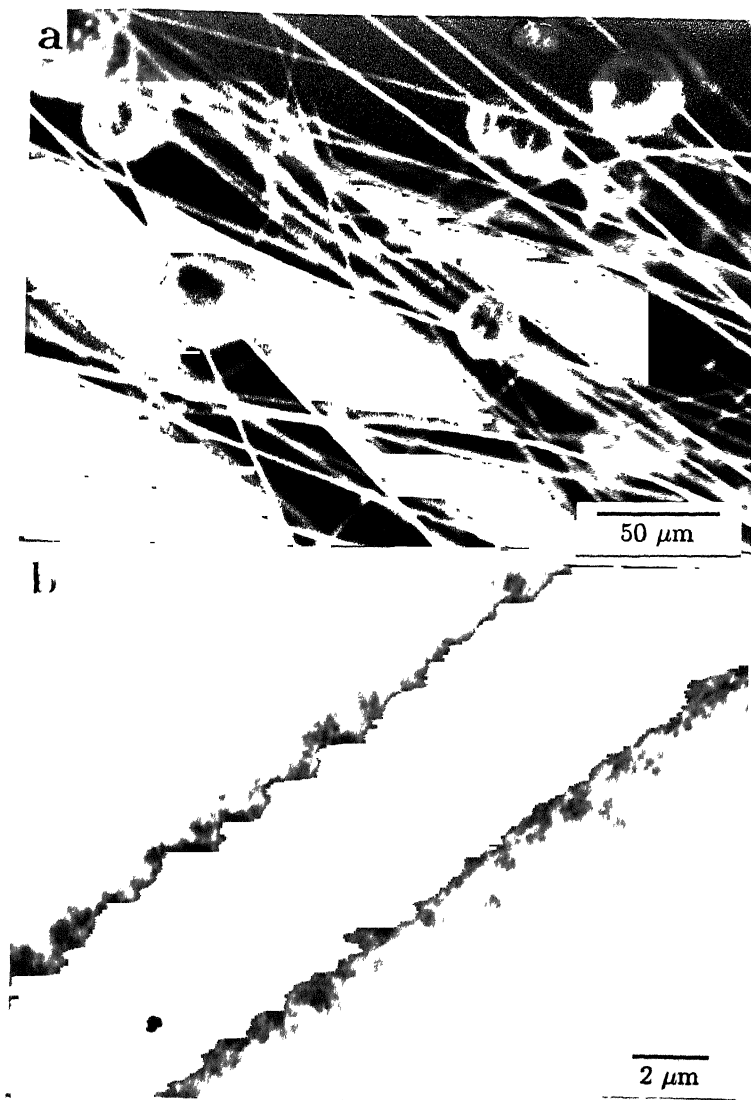
Figure 4.1: (a) SEM and (b) TEM micrographs of the MgO fibres showing polycrystalline nature.
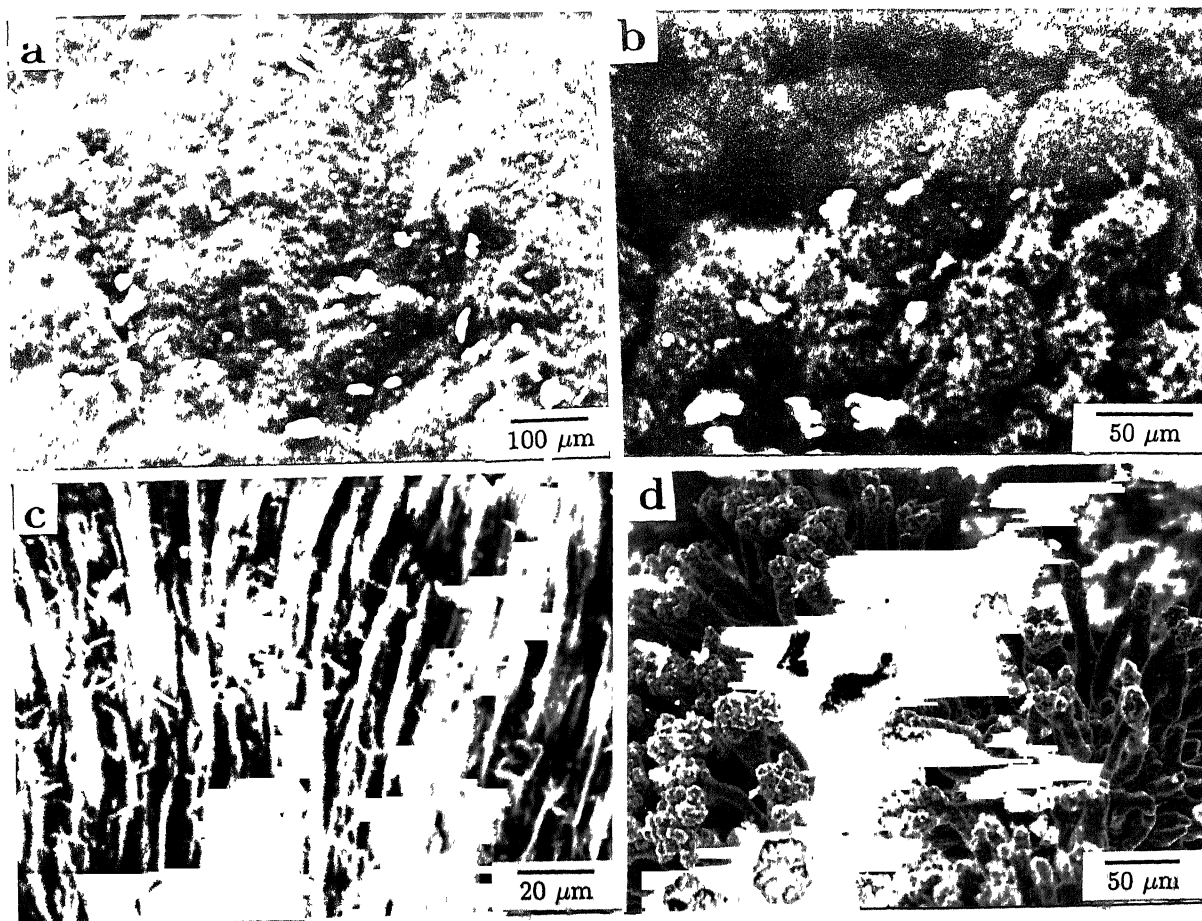
Figure 4.2: Surface nitride features of (a) Al-8Mg, (b) Al-8Zn, (c) Al-3Na and (d) Al-2.3Li alloys nitrided at 1050$°C$.
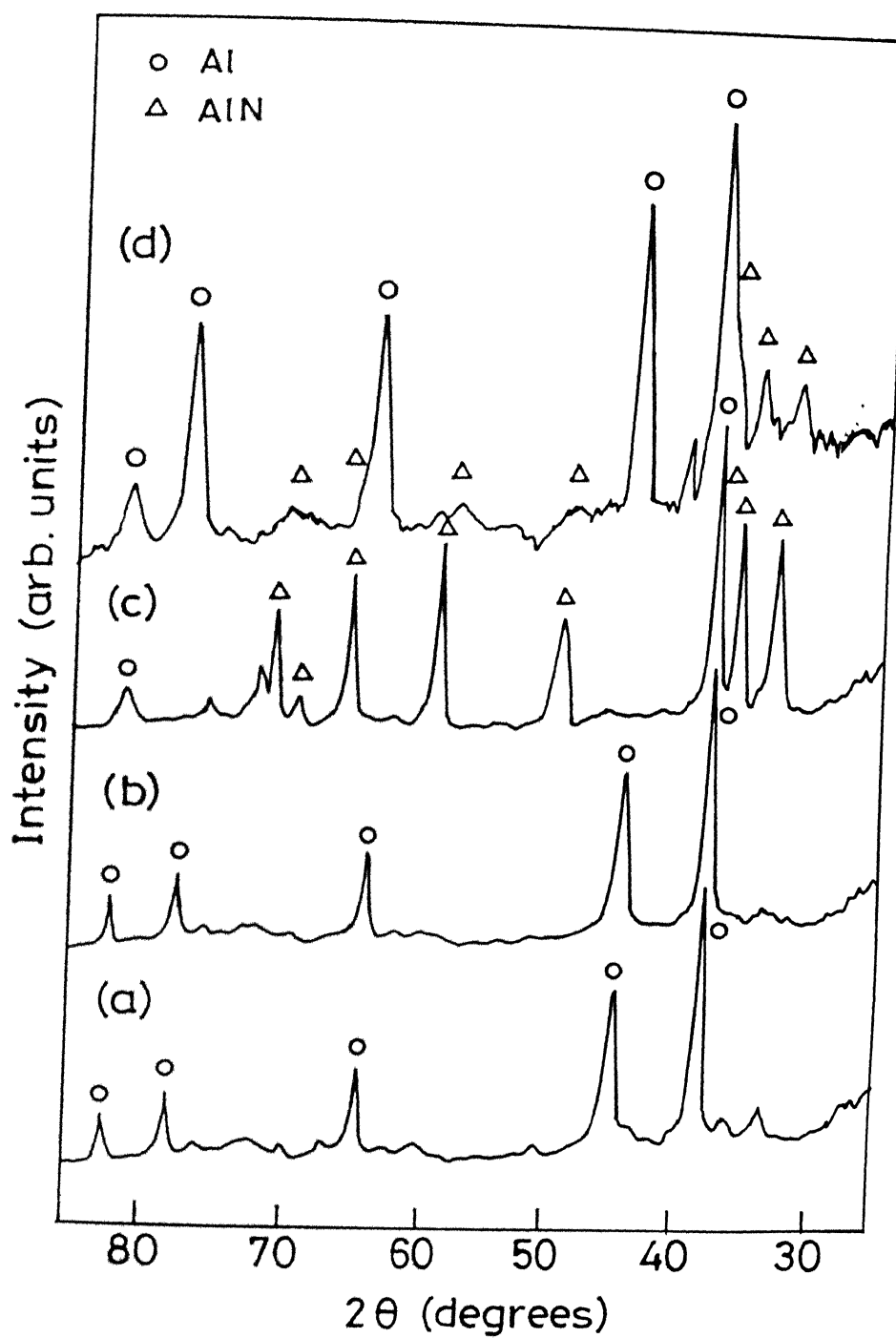
Figure 4.3: X-ray analysis of the surface nitride layer of (a) Al-8Mg, (b) Al-8Zn, (c) Al-3Na and (d) Al-2.3Li nitrided at 1050°C.
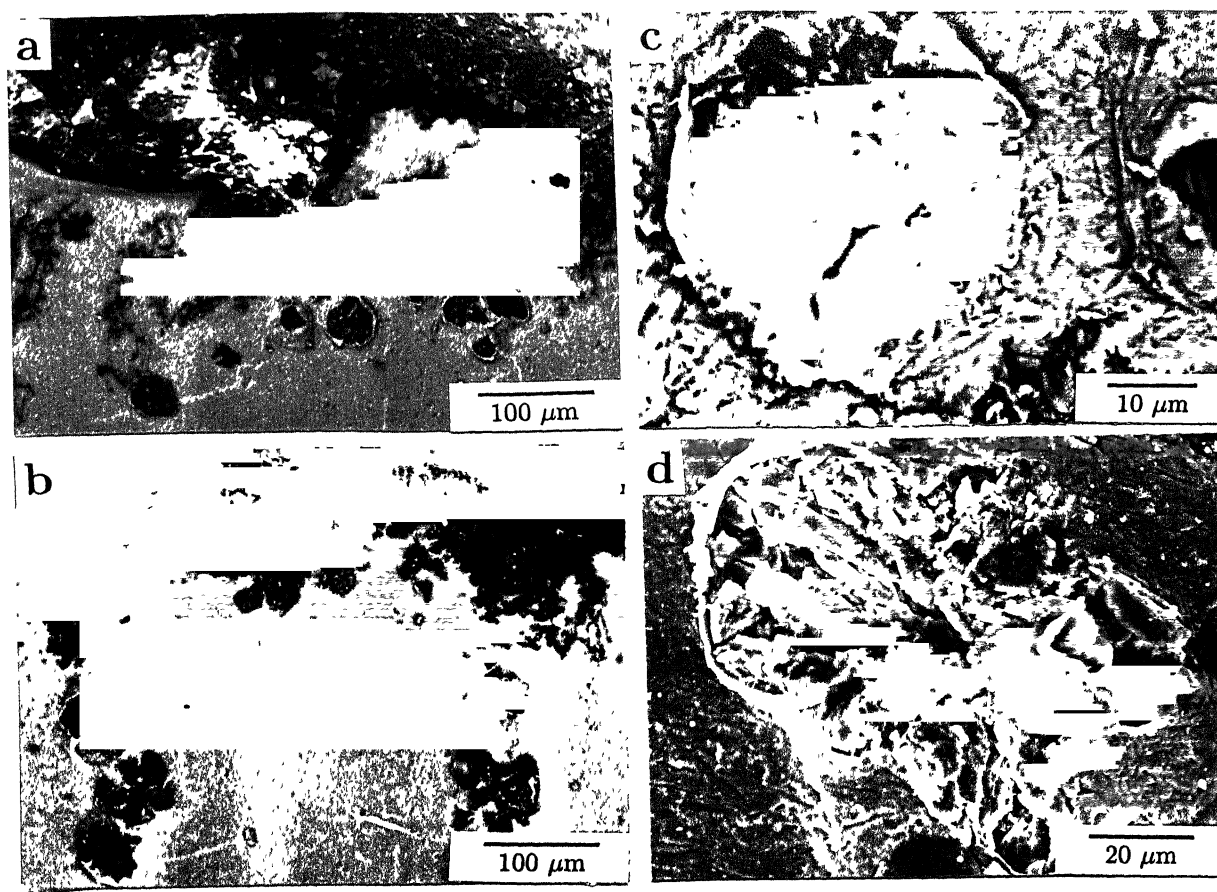
Figure 4.4: Cross-sectional micrographs showing surface nitride features of (a) Al-3Na and (b) Al-2.3Li alloys. (c&d) show enlarged view of the isolated internal nitride formed in (a&b), respectively.

(a) Nitridation studies in Al-2Si-8Mg alloy

To understand the AlN/Al composite growth mechanism, the nitridation of an Al-2Si-8Mg alloy at 1100^oC was interrupted at different time intervals (by periodically removing the specimen from the furnace) to observe the macro and microstructural development. In the early stages of the experiment (<6 hours), the Mg in the alloy escapes as vapour and is deposited as white MgO crystals on the sample surface and refractory tube walls. Simultaneously, nitride formation commences and the surface of the alloy turns black. Subsequently, the alloy *wicks* through the microdiscontinuities in the surface nitride layer, forming small metal globules (Figure 4.5a). With time, the globules coalesce into small colonies (Figure 4.5b) and bulk composite growth begins. When these colonies were observed at a later stage (>15 hours), long columnar AlN crystal growth is observed (Figure 4.5c). In select regions, hexagonal faceted AlN crystals were also observed on the surface.

The cross-sectional micrographs in Figure 4.6 identify the different regions of composite growth in Al-2Si-8Mg alloy after 12 hours. The primary globule appearing on the surface formed an AlN/Al layer of >300 μm thickness (Figure 4.6a). Further formation of fine globules atop the primary nodule is also seen. The metal reservoir present in the center of the globule supplies aluminum through microchannels that are present in the composite layer to the secondary globule (Figure 4.6b). The underneath composite layer reveals columnar AlN crystals and microchannels which also supply metal to the reservoir in the primary globule (Figure 4.6c).

(b) Effect of process temperature

Together with alloying additions, temperature is considered to be an important variable to control composite growth in liquid melts. The cross-sectional micrographs of Al-2Si-8Mg alloy nitrided for 40 hours at 950, 1050 and 1150^oC are shown in Figure 4.7. With increase in processing temperature, three domains of nitride formation are clearly delineated. The
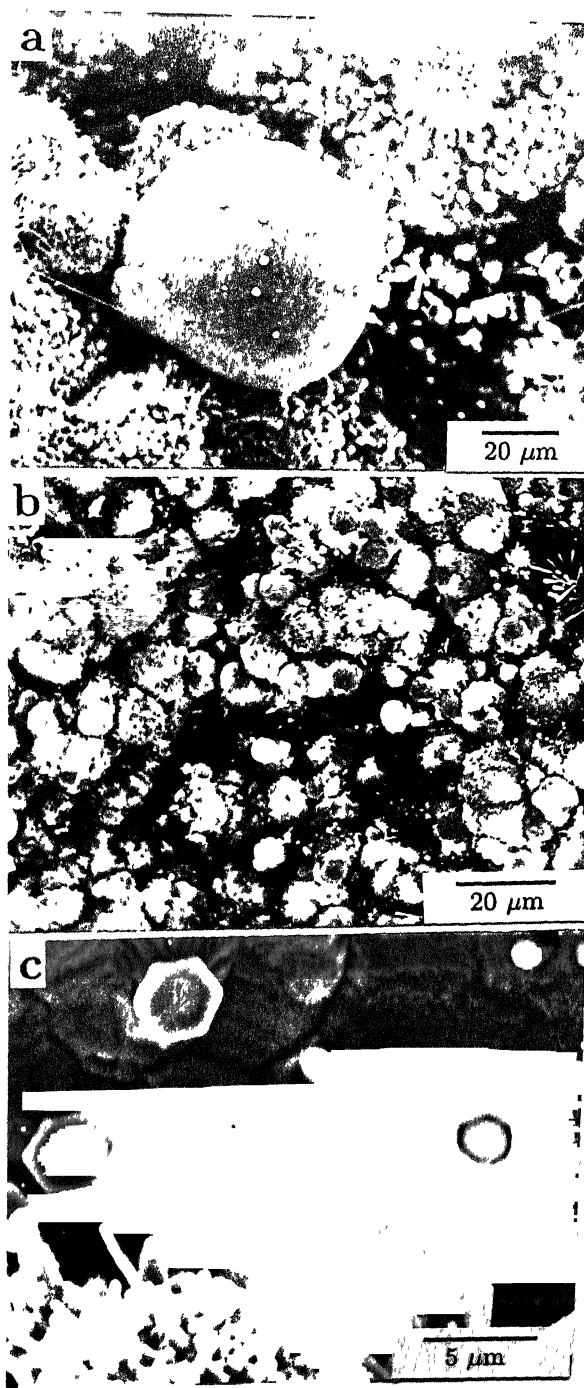
Figure 4.5: Stages of AlN growth. (a) Aluminum alloy wicking to the surface, (b) globules coalesce to form the growth front and (c) hexagonal crystal formation on the surface.
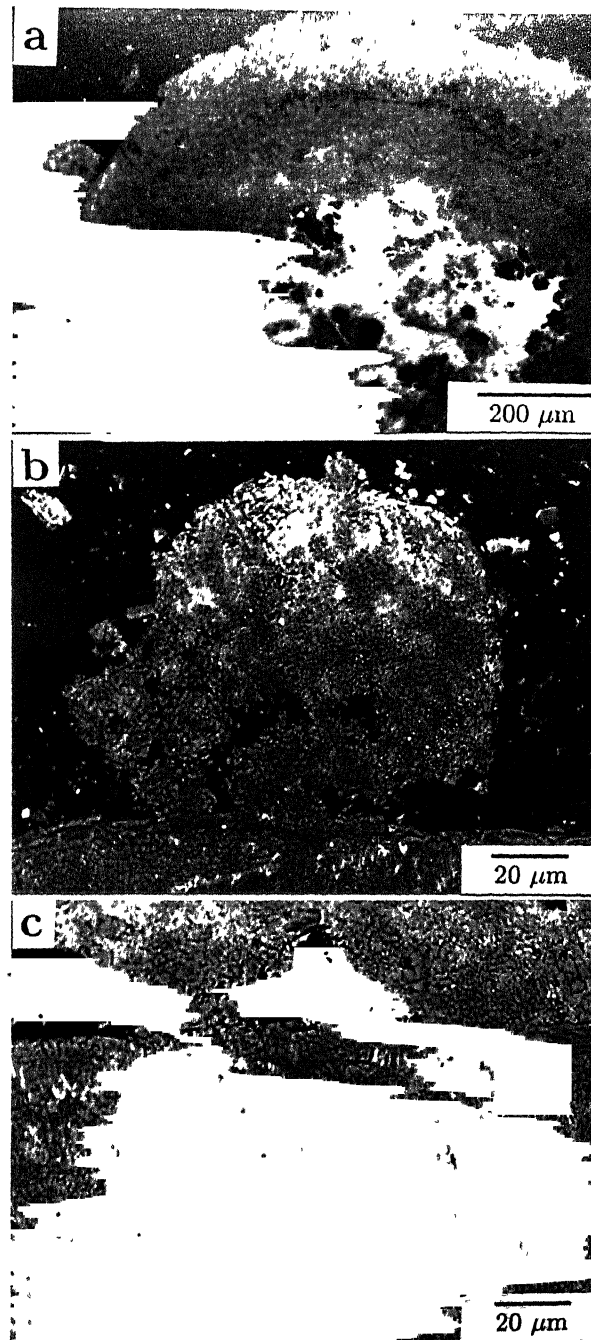
Figure 4.6: Cross-sectional view of (a) a globule with a central metal reservoir, (b) a secondary globule with interconnected AlN/Al and (c) the underneath layer showing AlN crystals and microchannels.
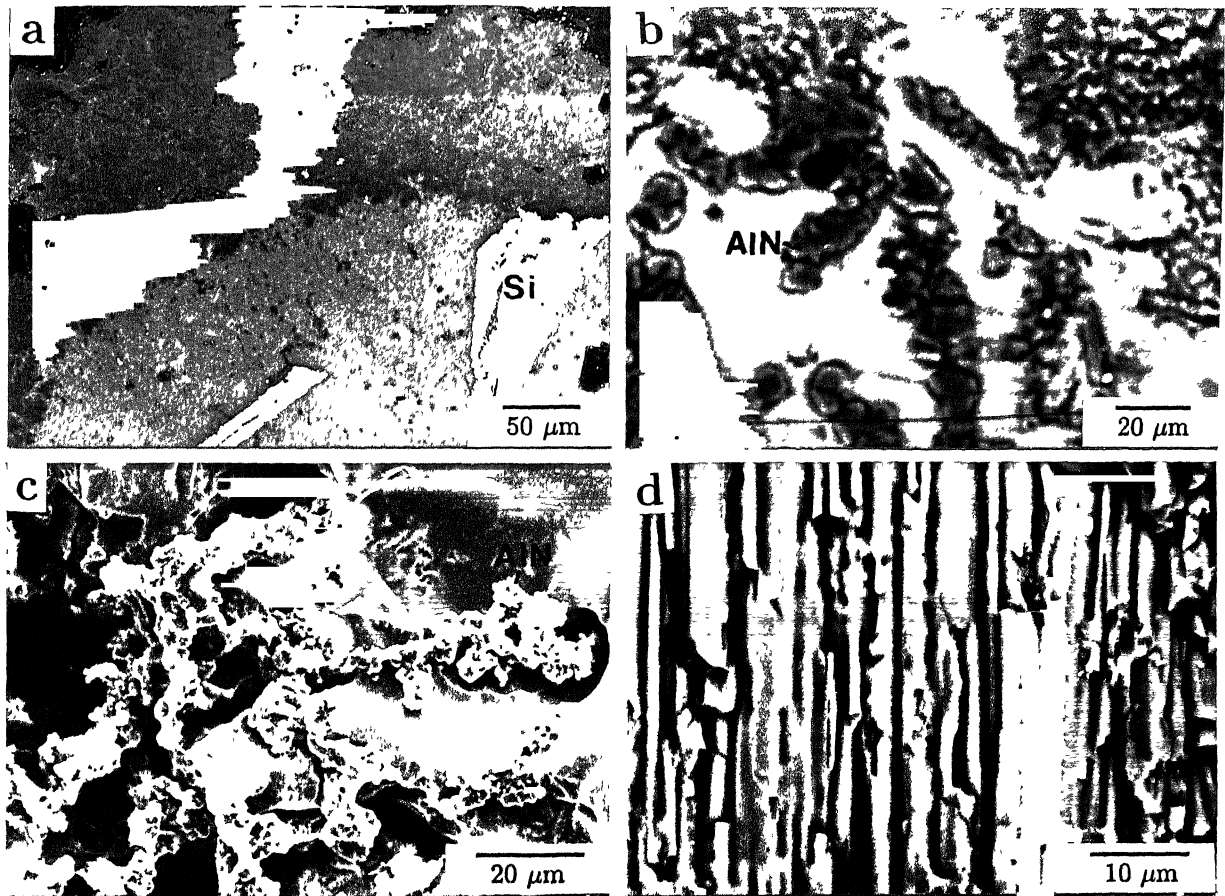
Figure 4.7: Cross-sectional micrographs showing (a) surface nitridation at 950^oC, (b) bulk nitridation at 1050^oC, (c) deep etched feature of (b) showing interconnected nature of AlN, and (d) break-away nitridation at 1150^oC showing long AlN crystals.

alloy nitrided at $950^{\circ}C$ shows only a *surface nitride layer* (<50 μm thick) with external globular growth (Figure 4.7a). On the other hand, the alloy nitrided at $1050^{\circ}C$ shows extensive AlN formation throughout the metal (Figure 4.7b). This is the desired AlN/Al composite processing domain and the microstructural feature is termed as *bulk nitridation*. A sample etched with 10% HF for 20 minutes reveals the interconnectivity of the AlN crystals (Figure 4.7c). Lastly, the alloy nitrided at $1150^{\circ}C$ shows friable AlN with crystals aligned parallel to the growth direction (Figure 4.7d). This morphology, termed as *break-away nitridation*, may not useful from composite processing viewpoint due to extensive porosity.

(c) Effect of Si on Nitridation

The binary alloys containing small amounts of Si were nitrided at $1050^{\circ}C$ for 24 and 40 hours

Table 4.2: Nitridation of Si containing ternary and quarternary alloys.

Alloy composition (wt.%)	Process temperature ($^{\circ}C$)	Process duration (hrs)	Normalized wt. gain (g/cm^2)
Al-2Si-8Zn	1050	24	−0.099
		40	−0.129
	1150	24	−0.219
Al-2Si-2.3Li	1050	24	+0.025
Al-0.5Si-8Mg	1100	40	+0.046
Al-2Si-8Mg	1050	24	−0.049
		40	−0.022
	1100	12	−0.034
		24	−0.017
		40	+0.014
Al-5Si-8Mg	1100	40	−0.010
Al-8Si-8Mg	1100	40	−0.094
Al-2Si-8Mg-1Fe	1050	40	−0.034
	1150	24	−0.042
Al-2Si-4Mg-4Zn	1050	40	−0.114
	1150	24	−0.109

(Table 4.2). After nitridation, no significant weight gain was observed in Al-2Si-8Zn and Al-2Si-3Li alloys compared to the binary alloys. On the contrary, the SEM micrographs reveal variations in the surface and internal microstructural characteristics (Figure 4.8). Though

the cross-section does not reveal any bulk nitride formation, the nodules appearing on the Al-2Si-8Zn alloy surface are finer compared to Al-8Zn alloy (Figure 4.1b). Similarly, the Al-2Si-2.3Li alloy does not show any nodular growth on the surface, whereas the cross-section reveals a fine and evenly distributed AlN/Al composite structure, as compared to Al-2.3Li alloy (Figure 4.1d). In the present work, interest is confined to the Mg containing alloys.

To study the influence of Si variation on the nitridation of Al–Si–Mg ternary alloy, alloys containing different amounts of Si (0.5–8 $wt.\%$) were nitrided (Table 4.2). The cross-sectional microstructures of alloys nitrided at 1100^oC for 24 hours are shown in Figure 4.9. While bulk nitridation is possible in Al-0.5Si-8Mg and Al-2Si-8Mg alloys, the nitride formation is limited to surface layer formation in the case of Al-5Si-8Mg (<1 mm) and Al-8Si-8Mg (<100 μm) alloys. X-ray analysis of Al-2Si-8Mg alloy nitrided at 1100^oC for 40 hours shows the presence of AlN and Al (Figure 4.10).

The TGA analysis of Al–Si–Mg alloys were carried out at 1000^oC for 12 hours (Figure 4.11). The weight gain vs time plots include both the weight loss due to Mg vapour escaping from the alloy and the weight gain due to AlN formation. The absence of any apparent weight loss is because the alumina wool used to partially seal the crucible mouth trapped most of the magnesia. This appears as an accelerated weight gain in the early stages of the experiment. Since both the processes take place simultaneously in the early stages of the experiment, it is difficult to isolate and differentiate between the two. Discounting the magnesia formation (since all the alloys had $8wt.\%$ Mg), a higher conversion of Al to AlN is observed with the increase in Mg/Si ratio.
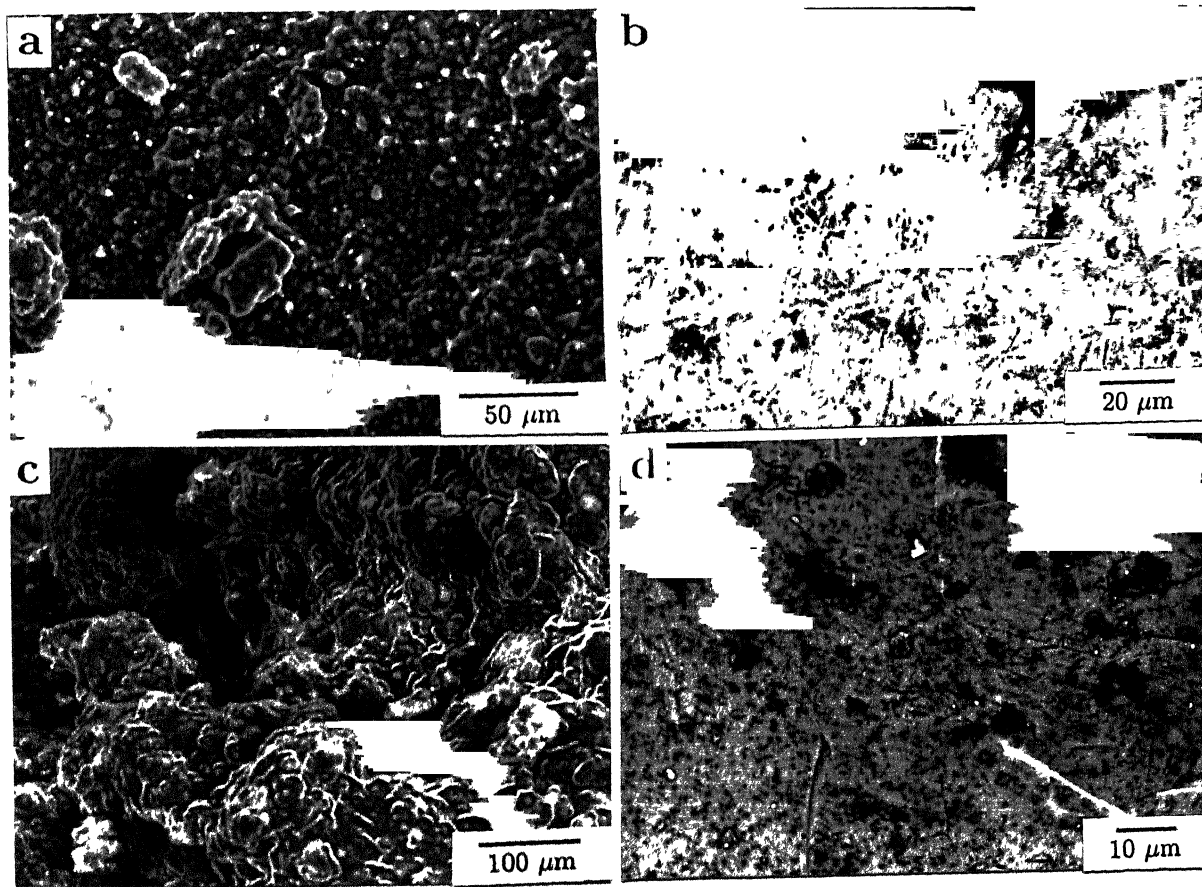
Figure 4.8: SEM micrographs of (a) Surface features and (b) internal structure of Al-2Si-8Zn alloy compared with (c) the surface features and (d) internal composite structure of Al-2Si-2.3Li alloy nitrided at $1050^{o}C$.
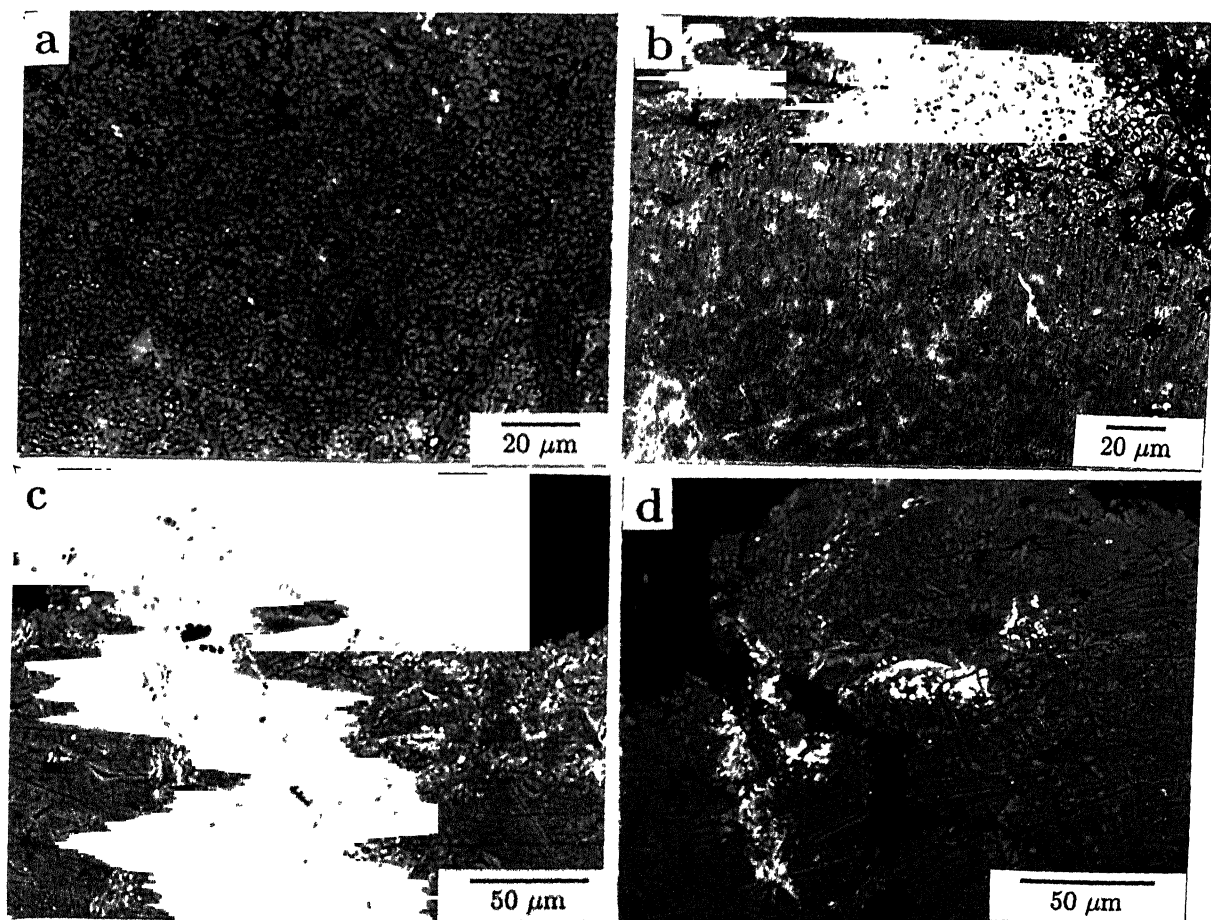
Figure 4.9: Cross-sectional micrographs of (a) Al-0.5Si-8Mg, (b) Al-2Si-8Mg, (c) Al-5Si-8Mg and (d) Al-8Si-8Mg alloys nitrided at 1100°C for 24 hours.
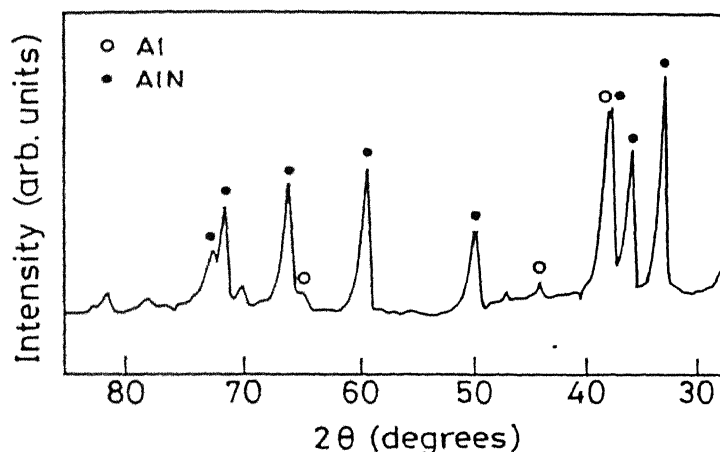
Figure 4.10: X-ray analysis of Al-2Si-8Mg nitrided at 1100°C for 40 hours.

(d) Effect of Fe addition

Small amounts of Fe addition are suggested to improve wetting and aid faster infiltration of Al-Si-Mg alloys [1,2]. To understand the influence of Fe on nitridation, Al-2Si-8Mg-1Fe alloy was nitrided at 1050 and 1100°C (Table 4.2). By comparing the weight gain with Al-2Si-8Mg alloy, it is noted that Fe additions does not reveal significant AlN formation. Further, the cross-sectional micrograph reveals only a surface nitride layer of ~100 μm thickness (Figure 4.12a). Some isolated AlN crystal growth was observed within the aluminum (Figure 4.12b). Comparing the microstructures with those of Al-2Si-8Mg (Figure 4.7b), it appears that Fe addition does not lead to extensive nitride formation.

(e) Effect of Mg and Zn additions

Since no composite development was observed in the Zn containing alloy, the combined influence of Mg and Zn was explored. Similar to Al-2Si-8Zn alloy, significant weight loss was observed in the Zn containing quarternary alloy (Table 4.2). The sample cross-section did not reveal any internal nitride formation. On the other hand, faceted cubical crystallites were obtained on the sample surface in several areas (Figure 4.13). The X-ray analysis of
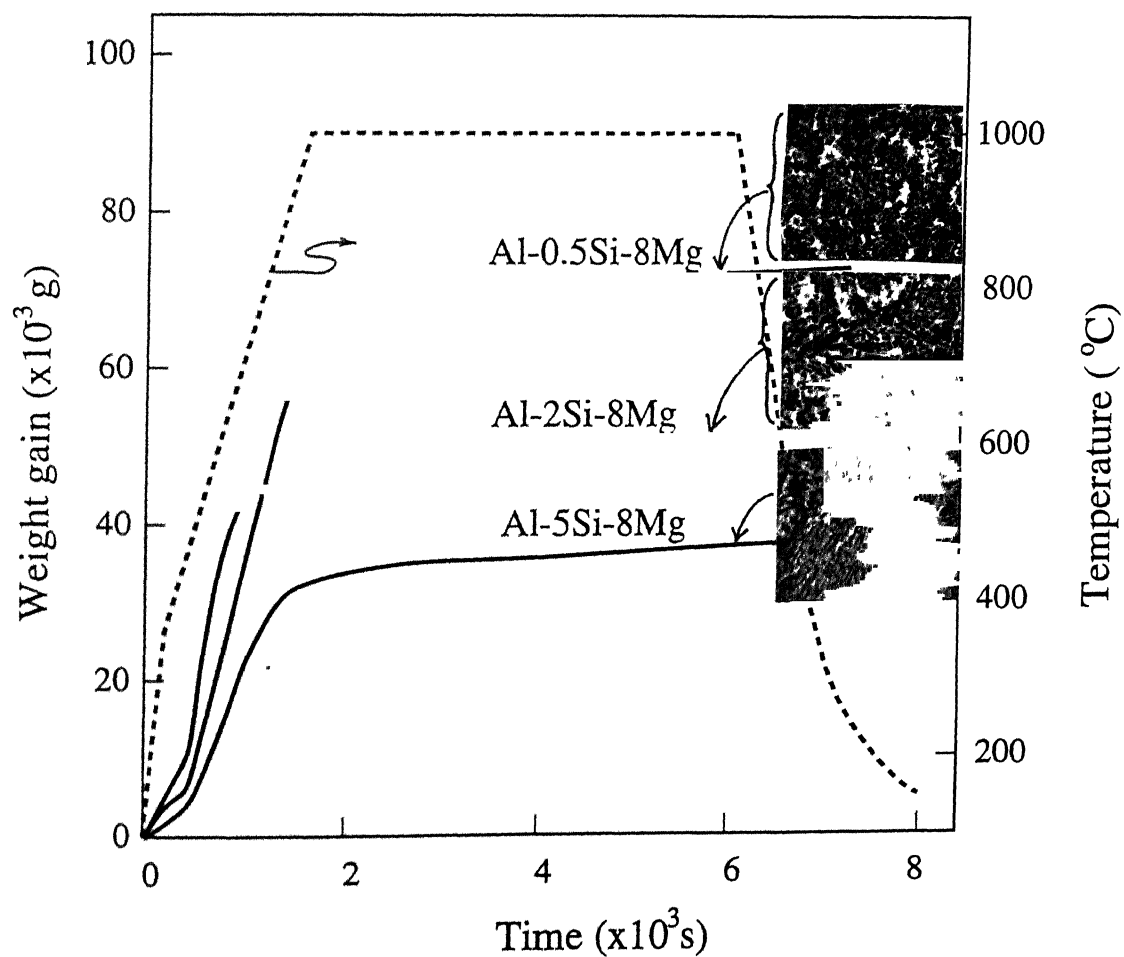
Figure 4.11: TGA plots of Al-0.5Si-8Mg, Al-2Si-8Mg and Al-5Si-8Mg alloys nitrided at 1000°C for 12 hours.

the surface layer identified the cuboids growing on the surface as the two cubic forms of AlN of the wurtzite and sphalerite type crystal structure (Figure 4.14). Previously, the transformation to cubic phase was known to take place only under high pressures. No AlN of the wurtzite structure was detected. Mg along with Zn appears to modify the growth pattern of AlN, such that the cubic phase becomes stable at atmospheric pressures.

Discussion

4.3 Mechanism of nitride growth

4.3.1 Solute atom influence in Nitridation

The role of Mg and Si on nitridation is multifold. Addition of Mg improves wettability by decreasing the contact angle. Unlike in oxide systems, the wettability of AlN by aluminum is extremely good [3]. Further improvement in wetting is anticipated with addition of volatile elements. Scholz and Griel [4] are of the opinion that Mg_3N_2 is responsible for modifying the nature of the surface nitride layer and improving the flux of Nitrogen into the melt. In the present investigation, the presence of Mg_3N_2 could not be detected. However, it is possible that it may be present in very small quantities. If Mg_3N_2 formation was the key step to continuous nitride formation, most Al–Mg alloys would have formed composites. On the contrary, Mg plays an important role as a local Oxygen getter. By preferential oxidation of the Mg in the vapour phase, the partial pressure of Oxygen seen by the aluminum alloy is much reduced and favourable conditions for nitridation is established. Finally, volatile solute atoms also appear to play an important role in determining the structure of AlN. In the presence of Mg, Li or Zn, AlN of the wurtzite crystal structure was formed. Contrarily, the dual presence of Mg and Zn resulted in AlN with a cubic (Sphalerite and NaCl type) structure. AlN of the wurtzite structure is reported to transform to NaCl type crystal structure at $\sim 21 \pm 1\ GPa$ at ambient temperatures [5]. On the other hand, transformation
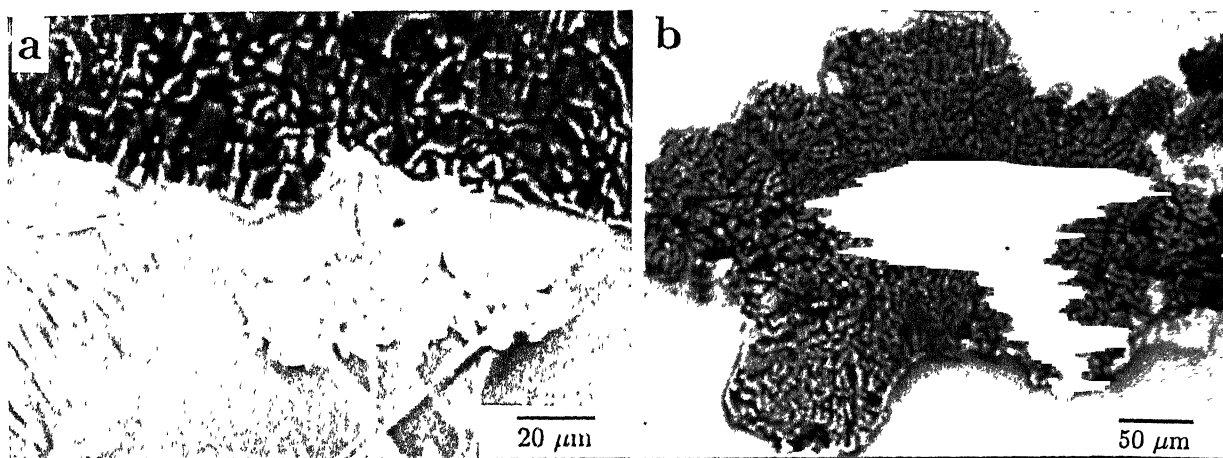
Figure 4.12: Cross-sectional micrograph showing (a) the surface nitride layer and (b) isolated internal nitride formation in Al-2Si-8Mg-1Fe alloy nitrided at $1100^{o}C$.
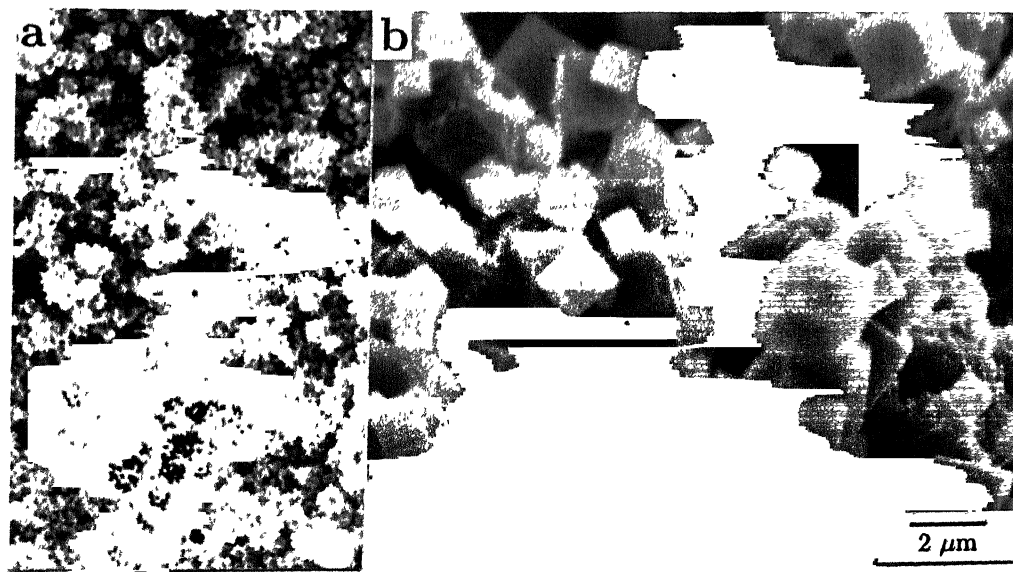
Figure 4.13: SEM micrographs showing (a) cubic AlN crystals on the Al-2Si-4Mg-4Zn alloy surface. (b) A higher magnification of the same.
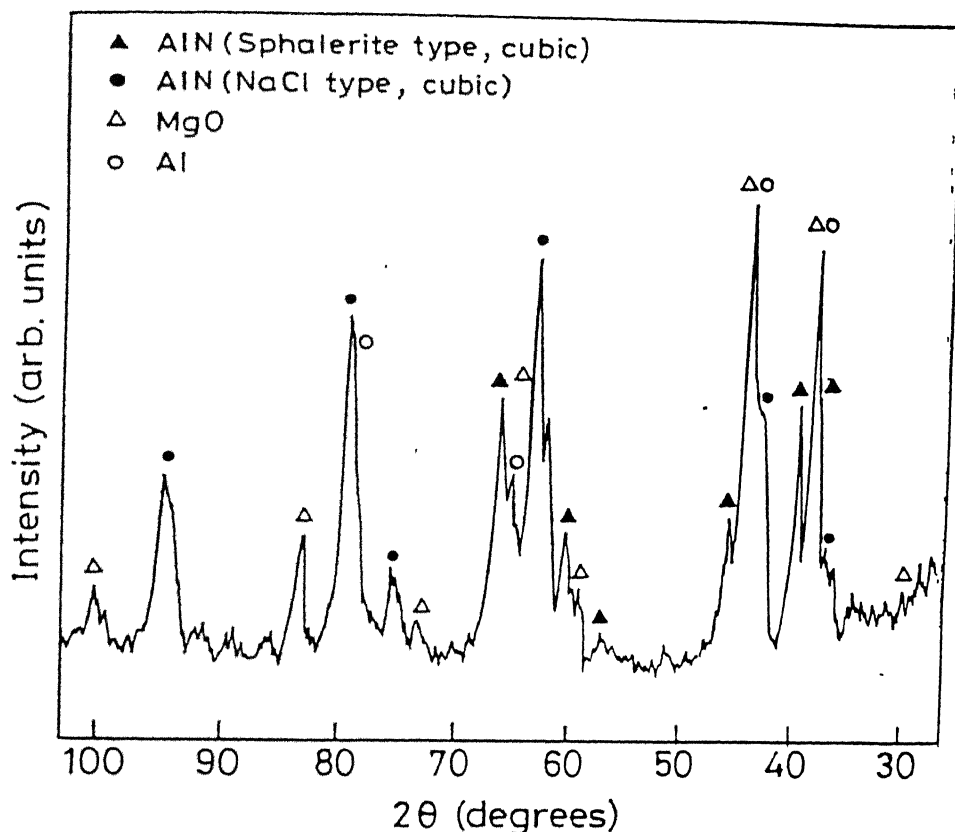
Figure 4.14: X-ray analysis of the surface layer of Al-2Si-4Mg-4Zn nitrided at $1050°C$ for 24 hours.

to Sphalerite type crystal structure is known to occur at 30 GPa at ambient temperature and 5.5 GPa at $1000°C$ [6]. In the present case, the combined influence of Mg and Zn modify the reaction conditions such that the cubic phase is the stable morphology at atmospheric pressure. Further study is required to fully understand this interesting transformation.

Si in isolation is non-effective in aluminum alloy nitridation. But in conjunction with Mg, it effectively transforms the reaction mechanism from a surface nitridation to bulk nitride formation. This change is brought about in two ways. Firstly, the surface nitride layer characteristics are modified by the appearance of extensive discontinuities, such as microcracking, microporosities, etc. These openings on the surface layer accommodate wicking of liquid alloy and nitridation takes place extensively. due to larger surface area of aluminum exposed to the reaction gas. Secondly, the nitride formation rate can be expected to improve by enhancing solubility or diffusivity of Nitrogen in the alloy. The solubility of Nitrogen in aluminum at $1000°C$ is reported to be 2×10^{-6} $at.\%$ [7]. Additionally. 0.5 $wt.\%$ addition of Si increased the viscosity of pure aluminum from 0.85 to 0.91 cP at $900°C$ [8]. However,

there is no data available on in the literature on the solubility and diffusivity of Nitrogen in complex aluminum alloys.

It is also important to note that rather than a mere presence of Mg and Si, a combined ratio of the two is of greater significance. A higher Mg is beneficial in controlling Oxygen in the reaction atmosphere. But higher Si containing alloys always form a passivating surface nitride layer [9]. For this reason, lower Si (i.e. higher Mg/Si ratio) is desirable for bulk composite growth.

4.3.2 Composite development in Al–Si–Mg alloys

The microstructural development during nitridation of Al-2Si-8Mg alloy progresses through several steps. Even as the Mg vapour escapes from the surface, the molten alloy gets nitrided forming a thin discontinuous layer of AlN on the surface (<1 μm thick). In the next stage, the surface nitride layer allows liquid metal to wick through the surface discontinuities, forming metal globules on the surface. As the process continues, the globules get nitrided and simultaneously coalesce to form a continuous growth front. The capillaries in between the AlN crystals aid wicking of molten metal, thereby sustaining the growth of AlN/Al composite structure. On the other hand, when the composite is processed at much higher temperature, the kinetics of AlN formation is faster resulting in columnar growth of AlN crystals along the [0001] crystal direction [10].

The nitridation process has many parallels to the DIMOX process which has been extensively studied [11–13]. In the early stages, when the alloy is held at above the liquidus temperature, a duplex oxide layer (MgO + $MgAl_2O_4$) forms on the surface. These oxide layers are porous and contain interconnected microdiscontinuities. The liquid metal from the underneath reservoir wicks through the pore channels and emerge as small nodules on the surface. Many such nodules coalesce to form a 'cauliflower' type of colony on the surface. Finally, several such colonies form a planar oxidation front. At each stage, the duplex layer envelopes the nodules and Mg (or any volatile species) in the alloy reservoir depletes with time. When the Mg content in the alloy drops below a threshold value, i.e. $0.3wt.\%$, columnar Al_2O_3 crystals

nucleate and grow to several tens of microns uninterruptedly. Al_2O_3 grows mainly as 'α' with the c-axis maintained parallel to the growth direction in an interconnected manner [14]. Finally, an Oxygen gradient builds up across the duplex layers causing Mg^{2+}, Al^{3+} and O^{2-} ions from the underneath layers to dissociate. Mg^{2+} ions migrate to the surface and maintain the nonprotective MgO layer, whereas Al^{3+} and O^{2-} contribute to bulk growth of Al_2O_3 [15].

The number of stages involved in AlN/Al composite growth are lesser compared to oxidation. In nitridation, no complex surface oxide/nitride layers are formed. However, transitional stages, such as nodule formation by wicking, conversion of these nodules to composite structure and columnar growth are quite similar. The specific volume ratio of the nitride layer ($V_{AlN}/V_{Al}=1.26$) is greater than unity and is expected to form a protective nitride surface layer. Similar to oxidation, Mg present in the alloy is reported to have a catalytic effect on nitride formation, such that it helps to transfer the surface reaction into a volume reaction [4].

Based on the reaction kinetics of composite formation, the Al to AlN conversion observed in this investigation can be broadly classified into four reaction domains. They include, (1) passivating surface nitridation with no internal nitride formation, (2) predominantly surface nitridation with diffusion controlled volume nitridation, (3) bulk nitridation with extensive outward AlN/Al composite growth and (4) break-away nitridation with complete conversion to AlN. In the present work, reaction mechanism 1 is observed in Al-8Mg and Al-8Zn alloys (Figure 4.2), where the nitridation is limited to a surface layer formation. Alloys with low Mg/Si ratio display mechanism 2 (Figure 4.9(c&d)). On the other hand, alloys with higher Mg/Si ratio (i.e. Al-0.5Si-8Mg and Al-2Si-8Mg) exhibit bulk nitridation (mechanism 3, Figure 4.9(a&b)). Lastly, break-away nitridation (mechanism 4) is observed in high Mg/Si ratio containing alloys nitrided at temperatures above 1100^oC (Figure 4.7d). In the earlier investigation, these four stages were observed by varying the alloy composition. From the present results, it is concluded that temperature variation can also shows similar transitions in reaction mechanism in a particular alloy.

The significant variables in aluminum alloy nitridation are the alloy composition, Oxygen

partial pressure and process temperature. The present experimental observation proves that small additions in Si is an important nitridation parameter. Scholz and Greil [4] had previously shown that by varying the Mg/Si ratio four reaction mechanisms, similar to those observed in the present investigation. Their experiments in static and flowing gas conditions proved that the nitridation mechanism is critically dependent on the Oxygen partial pressure. Accelerated nitride formation (mechanism 4) was observed when the Oxygen partial pressure was very low, such as in static gas conditions. On the contrary, in flowing gas conditions, the effective Oxygen partial pressure is higher because of continuous depletion of the Mg vapour cloud from above the alloy surface.

Temperature as a processing variable has been shown to alter the nitridation reaction mechanism from a surface reaction (mechanism 1) to break-away nitridation (mechanism 4, Figure 4.7). An increase in process temperature will enhance the nitridation reaction kinetics, increase Nitrogen solubility and decrease the melt viscosity. Apparently, since the reaction kinetics has an exponential dependence on temperature, above a critical temperature, the growth of AlN is much faster and grows as continuous columnar crystals (Figure 4.7d). Further, the continuous directional growth of AlN crystals on the alloy surface (Figure 4.2(c&d)) and limited solubility of of Nitrogen in aluminum suggest that the growth of AlN could take place by a Vapour-Liquid-Solid (VLS) mechanism. Such whisker like growths have been previously observed and reported in nitridation and carbide formation of Si alloys [16–18].

A possible explanation for the bulk nitride formation in Al-Si-Mg alloys is as follows. When a high Mg/Si ratio containing alloy is heated above the liquidus temperature, the alloy looses Mg to the vapour phase. The effective Oxygen partial pressure reduction at the alloy surface during the initial stages, facilitates nucleation and growth of AlN crystals at several sites due to vapour phase (gas-liquid) reaction. Moreover, in nitriding a high Mg containing alloy, before the solute Mg is completely depleted, sufficient network of AlN/Al is formed on the surface. Once the composite network has developed, the outward growth of composite (mechanism 3) is sustained by the capillary pressure, long after all the Mg has escaped from the alloy. With increase in Si concentration in the alloy, the enhanced viscous force decreases the ability of the metal to wick through the surface discontinuities,

thereby leading to only an isolated, diffusion controlled internal nitridation (mechanism 2). Alternatively, a decrease in the Mg concentration of the alloy will not allow sufficient time for the AlN crystals to form and develop microchannels on the surface, before the Mg is depleted resulting in only a surface nitride formation (mechanism 1). On the other hand, when a high Mg/Si containing alloy is nitrided at high temperature ($>1100^\circ C$), the rapid conversion of Al to AlN in the presence of an Oxygen getter leads to an extended outward growth of AlN crystals (mechanism 4). The wicking of metal through the pore channels does not keep pace with outward growth, resulting in a porous structure. Thus, the alloy composition, gas purity and temperature are critical to the nitridation process.

4.4   Preliminary infiltration experiments

There is a lack of contact angle data for various aluminum alloys on SiC substrate material in Nitrogen atmosphere. In the absence of such information, to characterize the infiltration behaviour, various alloys were infiltrated through SiC particulate preforms. The selected binary alloys were not successful in infiltrating in the temperature range of $900-1100^\circ C$. On the other hand, with 2 $wt.\%$ addition of Si, Al-2Si-8Mg and Al-2Si-3Li were able to infiltrate, but no preform wetting was possible by the Zn containing ternary alloy. Best infiltration rates were obtained in the Al–Si–Mg system. It was noted earlier that the Al to AlN conversion improves with increase in Mg/Si ratio. Infiltration with Al-0.5Si-8Mg alloy resulted in non-uniform liquid metal penetration, leaving large uninfiltrated cavities within the preform. On the contrary, no such anomalies were observed in the case of Al-2Si-8Mg alloy infiltrated through SiC preforms. For this reason, Al-2Si-8Mg alloy was selected for infiltration experiments. The details of the infiltration studies are provided in the following chapter.

4.5 Summary

The microstructural development during nitridation in several binary and Si containing complex alloys were studied. Among the binary alloys, nitridation was either limited by the formation of a passivating surface nitride layer or confined to external growth of crystals with very little bulk nitridation. On the contrary, with small amount of Si addition, the nitridation characteristics transforms to a bulk nitridation with outward growth of AlN/Al composite network. Similar to Oxidation, the bulk nitridation of aluminum alloys progresses through several stages. Due to the Oxygen gettering by certain volatile elements, such as Mg, Li and Na, and possibly improved Nitrogen solubility by Si solute atoms, accelerated nitride growth takes place on the alloy surface forming AlN/Al composite. After the depletion of the Mg solute atoms, the capillary pressure forces the metal to wick through the micropore channels and form globules on the surface. These globules contain interconnected network of AlN/Al and are in contact with the metal reservoir below. As the process continues, the globules coalesce together to form the composite growth front.

By varying the ratio of Mg/Si solute content in the alloy and temperature, four different nitridation reaction mechanisms have been identified. They include, (i) passivating surface nitridation with no internal nitride formation, (ii) predominantly surface nitridation with diffusion controlled volume nitridation, (iii) bulk nitridation with extensive outward AlN/Al composite development and (iv) break-away nitridation with complete conversion to AlN. In all the alloys studied till now, AlN of the wurtzite crystal structure formed. In contrast, AlN of the Sphalerite and NaCl type crystal structure in obtained in the nitridation of a Mg and Zn containing alloy. Finally, during preliminary infiltration experiments, Al-2Si-8Mg alloy displayed optimal infiltration characteristics. Al-2Si-8Mg alloy selected for infiltration studies for its consistency in uniformly infiltrating SiC preforms at sufficiently fast rates.

References

[1] D. K. Creber, S. D. Poste, M. K. Aghajanian and T. D. Claar, AlN composite growth

by nitridation of aluminum alloys, *Ceram. Eng. Sci. Proc.*, **9** (1988) 975–982.

[2] M. K. Aghajanian, J. T. Burke, D. R. White and A. S. Nagelberg, A new infiltration process for the fabrication of metal matrix composites, *SAMPE Q.*, **20** (1989) 43–46.

[3] S. K. Rhee, Wetting of ceramics by liquid aluminum, *J. Am. Ceram. Soc.*, **53** (1970) 386–390.

[4] H. Scholz and P. Greil, Nitridation reactions of molten Al-(Mg,Si) alloys, *J. Mat. Sci.*, **26** (1991) 669–677.

[5] K. Kondo, A. Sawaoka, K. Sato and M. Ando, Shock compression and phase transformation of SlN and BP, in *Shock waves in Condensed Matter – 1981, AIP Conf. proc. No. 78*, Ed. W. J. Nellis, L. Seaman and R. A. Graham, New York, U.S.A. (1982) 325–329.

[6] L. F. Vereschagin, G. A. Adadurov, O. N. Breusov, K. P. Burdina, L. N. Burenkova, A. N. Dremin, E. V. Zubova and A. I. Rogacheva, Effect of high static and dynamic pressure on aluminum nitride, *Dokl. Akad. Nauk SSSR*, **182**[2] (1968) 301–303.

[7] H. A. Wriedt, The Al–N system, *Bull. Alloy Phase Diagram*, **7** (1986) 329–333.

[8] F. Lihl, E. Nachtigali and A. Schwaiger, Construction of Al–Si phase diagram, *Z. Metallk.*, **89** (1968) 213–217.

[9] Y. Kagawa, S. C. Khatri and M. J. Koczak, Directed nitridation of liquid aluminum alloy: Growth process and modeling, *Ceram. Eng. Sci. Proc.*, **14** (1993) 776–781.

[10] P. G. Caceres and H. K. Schmid, Morphology and crystallography of Aluminum Nitride whiskers, *J. Am. Ceram. Soc.*, **77** (1994) 977–983.

[11] O. Salas, H. Ni, V. Jayaram, K. C. Vlach, C. G. Levi and R. Mehrabian, Nucleation and growth of Al_2O_3/metal composites by oxidation of aluminum alloys, *J. Mater. Res.*, **6** (1991) 1964–1981.

[12] A. S. Nagelberg, S. Antolin and A. W. Urquhart, Formation of Al_2O_3/metal composites by the directed oxidation of molten Aluminum-Magnesium-Silicon alloys: Part II, Growth Kinetics, *J. Am. Ceram. Soc.*, **75** (1992) 455–462.

[13] V. S. R. Murthy, and B. S. Rao, Microstructural development in the directed melt oxidized (DIMOX) Al-Mg-Si alloys, *J. Mater. Sci.*, **30** (1995) 3091–3097.

[14] E. Breval, M. K. Aghajanian, J. Biel and N. S. Nagelberg, Directed oxidation/nitridation of Al alloys: The orientation of the oxides/nitrides formed adjacent to Al_2O_3 or AlN reinforcement particles, *J. Mater. Sci. Lett.*, **14** (1995) 28–30.

[15] V. Jayaram, Ceramic components by melt oxidation, *Mater. Eng.*, **3** 247–259.

[16] A. Atkinson, A. J. Mouldson and E. W. Roberts, Nitridation of high-purity Silicon, *J. Am. Ceram. Soc.*, **59** (1976) 285–89.

[17] N. V. Gribkov, V. A. Silaev, B. V. Shchetanov, E. L. Umautsev and A. S. Isaikin, Growth mechanisms of Silicon Nitride whiskers, *Sav. Phys. Crystall.*, **16** (1972) 852–54.

[18] J. P. Milewski, G. F. Hurley, Vapour–liquid–solid (VLS) SiC whiskers: Synthesis and mechanical properties, in *Fiber reinforced Ceramic Composites*, ed. K. S. Mazdiyasni, Noyes publication, New Jersy, U.S.A. (1990), 93–101.

Chapter 5

Reinforced AlN/Al Composites

5.1 Introduction

In the previous chapter of Results and Discussion, AlN/Al composite growth in several binary and ternary alloys was examined. Among the various Al-Si-Mg alloys studied, composite growth was observed to be faster in alloys having a higher Mg/Si ratio. Additionally, increased Mg content in the alloy enhances the wettability of liquid onto ceramic preforms achieving better infiltration. For infiltration of SiC preforms, Al-2Si-8Mg alloy was preferred because of uniform and fast composite formation. Earlier, Aghajanian *et al.* [1] had infiltrated Al_2O_3, TiB_2, AlN and Si_3N_4 preforms, but no detailed work was reported with SiC preforms. Hence in the present work, different SiC filler materials (particulates, platelets and fibres) were infiltrated under various processing conditions. The microstructure and mechanical properties of these composites were evaluated and compared with AlN reinforced AlN/Al composites, which were infiltrated under similar conditions.

Further, the high temperature application of AlN/Al composites is limited by the presence of residual aluminum which softens at $\sim 600^o C$. By converting the residual aluminum to a high temperature phase, one can extend its application to higher temperatures. In the later part of the chapter, an attempt to convert the residual aluminum to an intermetallic is presented. The microstructural development and mechanical properties of nickel aluminide infiltrated composites are studied at different reaction temperatures.

5.2   Microstructural development in SiC reinforced AlN/Al composite

Incorporation of a reinforcement phase within the directed melt nitrided composite has several advantages. The composite growth rate improves and enhanced mechanical properties are envisaged. Additionally, with the ability to tailor the microstructure, composites with a wide range of properties can be produced. Alloying additions play a significant role by modifying the wetting characteristics and altering the reaction kinetics. Mg along with Si are known to aid infiltration. Apart from alloying additions and filler material, reaction atmosphere and temperature are additional variables to tailor microstructure and properties. In the following sections, the influence of filler morphology, size and processing temperature are presented and discussed.

5.2.1   Effect of reinforcement morphology

Various forms of SiC reinforcements were infiltrated using Al-2Si-8Mg as the base alloy, at a temperature of $950^{\circ}C$, over a constant period of 8 hours (Table 5.1). From the results obtained, it was not possible to isolate the effect of the filler geometry on infiltration rate, because of the large differences in filler size. The wettability of SiC substrate material by Al is poor (contact angle, $\theta = 120^{\circ}$) [2]. In Nitrogen atmosphere with Mg alloying additions, substantial decrease in the contact angle value is achieved [3]. Mg additions modify the surface tension of the alloy, which in turn improves the wettability. Alternatively, Mg can induce spontaneous wetting through promotion of interfacial reaction with the substrate material. In comparison to infiltration in SiC preforms, the infiltration rates in AlN particulate preforms were faster by a factor of two. This rapid rise of liquid alloy through relatively fine
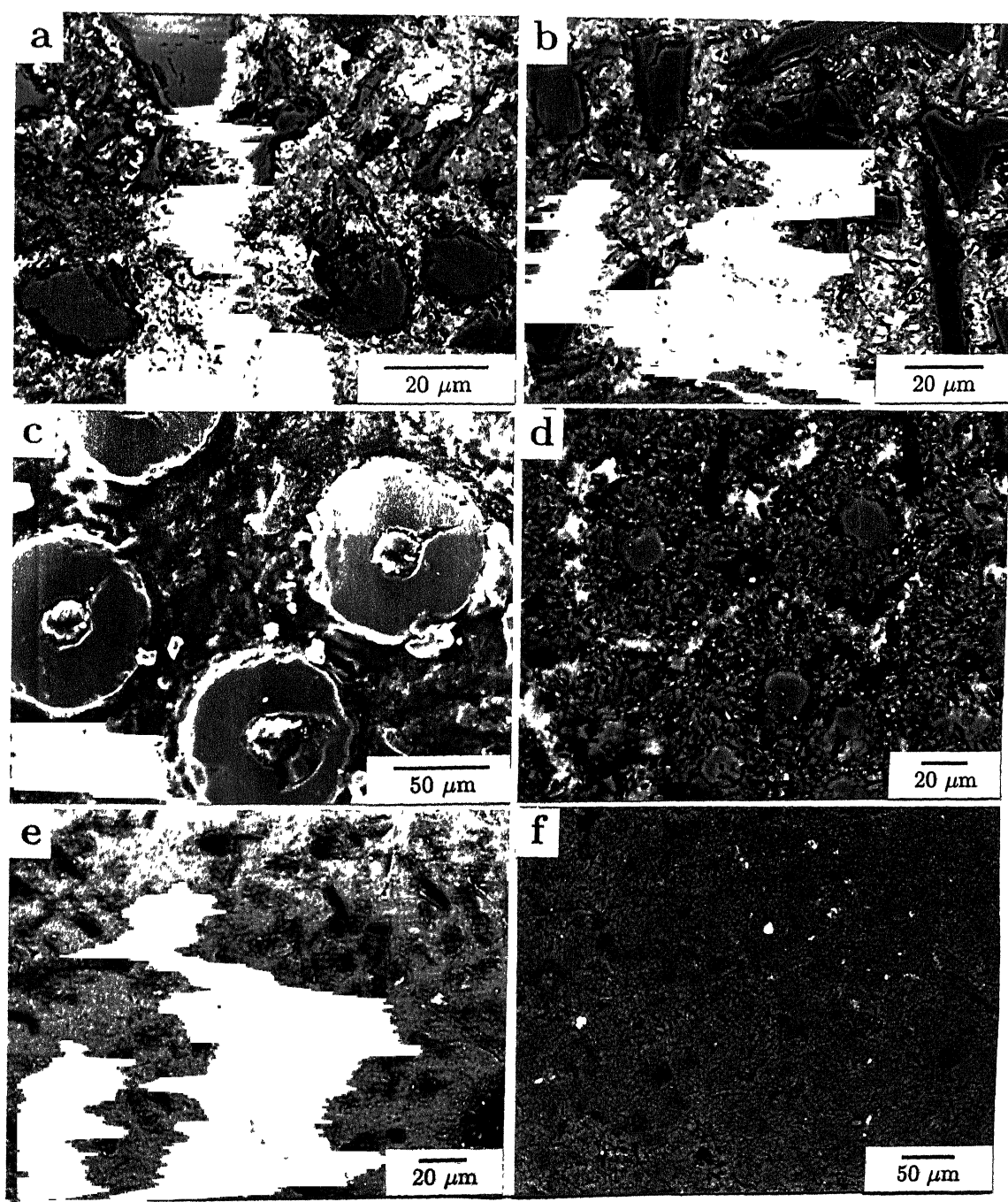
Figure 5.1: Microstructures of AlN/Al composites with various reinforcements. (a) SiC particulates, (b) SiC platelets, (c) AVCO SVS-6 fibres, (d) Nicalon fibres, (e) chopped fibres and (f) AlN particulates.

pore channels is mainly due to the enhanced wetting of AlN substrate material. Another important observation in the case of infiltration through platelet preforms is its non-uniformity. This is due to the obstruction of liquid metal path by preferential stacking of platelets on their faceted surfaces.

Table 5.1: Microstructural constituents and infiltration data of various filler material processed at 950°C.

Filler material	Reinforcement size (μm)	Volume fraction (%)			Infiltration rate (mm/hr)
		Porosity	AlN/Al	SiC	
SiC fibre	10–25	<3	58	38	–
SiC short fibre	5–10	<3	56	41	–
SiC platelet	20–30	<5	52	43	0.25
SiC particulate	45–71	0.8	40	59	1.0
AlN particulate	3–20	<1	48	51[†]	2.1

[†] AlN reinforcement

More than the filler geometry, the surface chemistry of the filler materials which were procured from various sources (see Table 3.2), is expected to significantly affect infiltration behaviour. SiC particulates and platelets have a thin silica layer on the surface. The surface chemistry details of SiC chopped fibres obtained from Millinium Technologies Inc. is not known. However, it appears that they are derived by reacting Carbon fibre with externally deposited Si. AVCO SVS-6 monofilaments (142 μm dia) are CVD processed with a 6 μm C/Si gradient layer on the periphery. On the other hand, Nicalon fibres contain a monocrystalline silicon-oxy-carbide structure with Oxygen enrichment on the surface.

The Microstructure of various SiC reinforced AlN/Al composites are illustrated in Figure 5.1. For comparison purpose, AlN particulate reinforced composite structure is also included. The X-ray analysis reveals the presence of SiC, AlN and Al in the case of SiC particulate reinforced composites (Figure 5.2). The submicron size metal channel through which metal wicks is shown in Figure 5.3a. In all the microstructures, a variation in composite structure (AlN/Al) and porosity levels are observed. The heterogeneous nucleation of AlN on Nicalon SiC fibres is distinctly seen, whereas in other reinforced structures, it is not as obvious. On the contrary, in AVCO SiC monofilaments, the surface carbon layer could have reacted with

the alloy to form Al_4C_3, inhibiting the nucleation of AlN on the fibre surface. Although Al_4C_3 formation is not evident in X-ray diffraction patterns obtained from SiC particulate composites, TEM investigation revealed the presence of isolated Al_4C_3 crystals adjacent to SiC (Figure 5.3b). The AlN reinforced composite microstructure are finer due to the micron size particulates used as filler material.
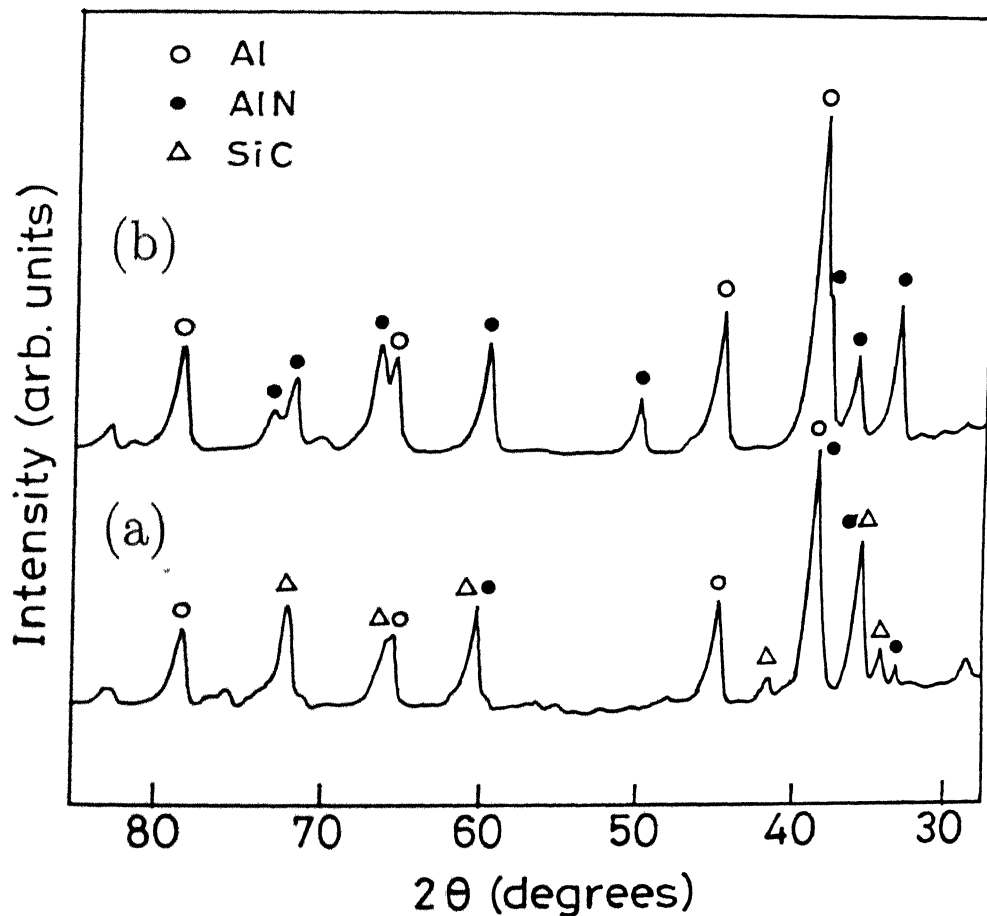
Figure 5.2: X-ray analysis of (a) SiC and (b)AlN particulate reinforced composites.

TEM micrographs clearly reveal the fine AlN crystallites growing in the aluminum matrix (Figure 5.3c). The average size of the AlN crystallites are less than one micron.
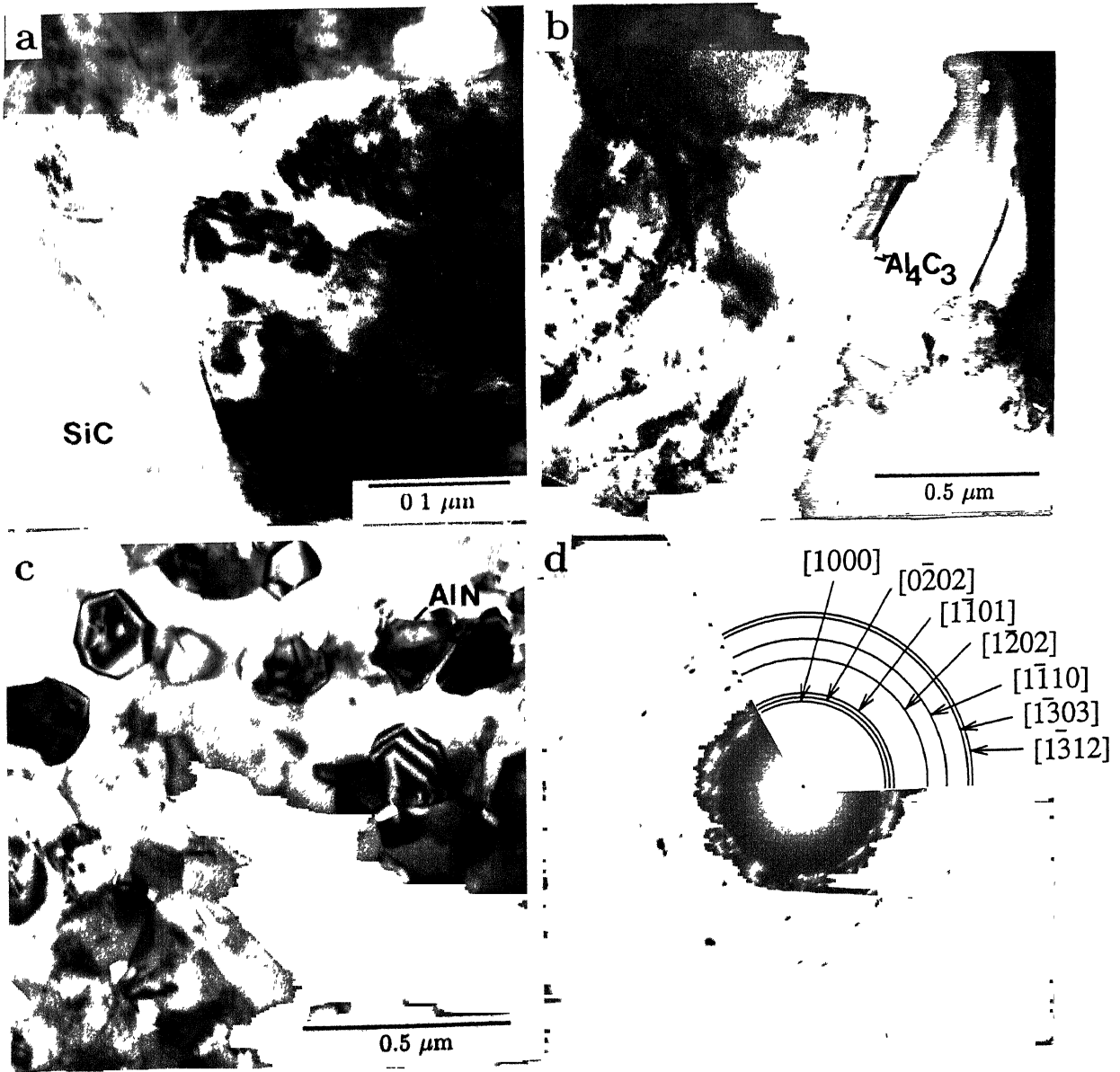
Figure 5.3: TEM micrographs showing (a) wicking through a microchannel in SiC particulate AlN/Al composite, (b) formation of Al_4C_3 in SiC particulate reinforced AlN/Al composite, (c) fine grained AlN crystals nucleated within the aluminum matrix and (d) SAD pattern of the fine AlN crystals.

5.2.2 Effect of particle size

To study the effect of filler size on composite formation, sintered SiC particulate preforms of different size ranges were prepared and infiltrated at 1050^oC for a duration of 6 hours. The infiltration data along with characteristics of the various SiC preforms are presented in Table 5.2. Firstly, there appears to be a direct correlation between the infiltration rate and the minimum pore radius (r). The calculated minimum pore radius represents the radius of the largest circle that fits within the closest triangular configuration of mean size particulates, assuming optimum distribution (FCC type) of perfectly spherical particles. SiC particles of smaller size (32–45 μm), having a minimum pore radius of 5.2 μm exhibit an infiltration rate of 0.9 mm/hr. In comparison, the larger particulate preform (71–160 μm),

Table 5.2: SiC preforms of various particulate size ranges infiltrated at 1050^oC.

Particulate size range (μm)	Packing fraction	Surface area ($10^3/m$)	Inter-particle distance (d) (μm)	Min. pore radius (r) (μm)	Infiltration rate (mm/hr)	Normalized wt. gain (g/cm^2)
32–45	0.56	87.1	42.4	5.2	0.9	0.69
45–71	0.58	60.0	62.9	7.3	1.2	0.60
71–160	0.61	31.5	123.5	13.5	1.5	0.42

with a minimum pore radius of 13.5 μm exhibits an infiltration rate of more than 1.5 times (1.5 mm/hr). Secondly, there is a direct relationship between the nitride formation rate (indicated by weight gain) and the mean preform particulate surface area. This is because the surface of the filler material offers sites for heterogeneous nucleation of AlN crystal (termed as secondary nucleation). Thirdly, due to the larger interparticulate spacing and lower conversion to AlN, larger shrinkage cavities are seen within the coarser particulate reinforced composites (Figure 5.4). The presence of porosity is expected to adversely affect mechanical properties.

In the coarser SiC particulate preform, infiltration is faster, but nitride formation rate is
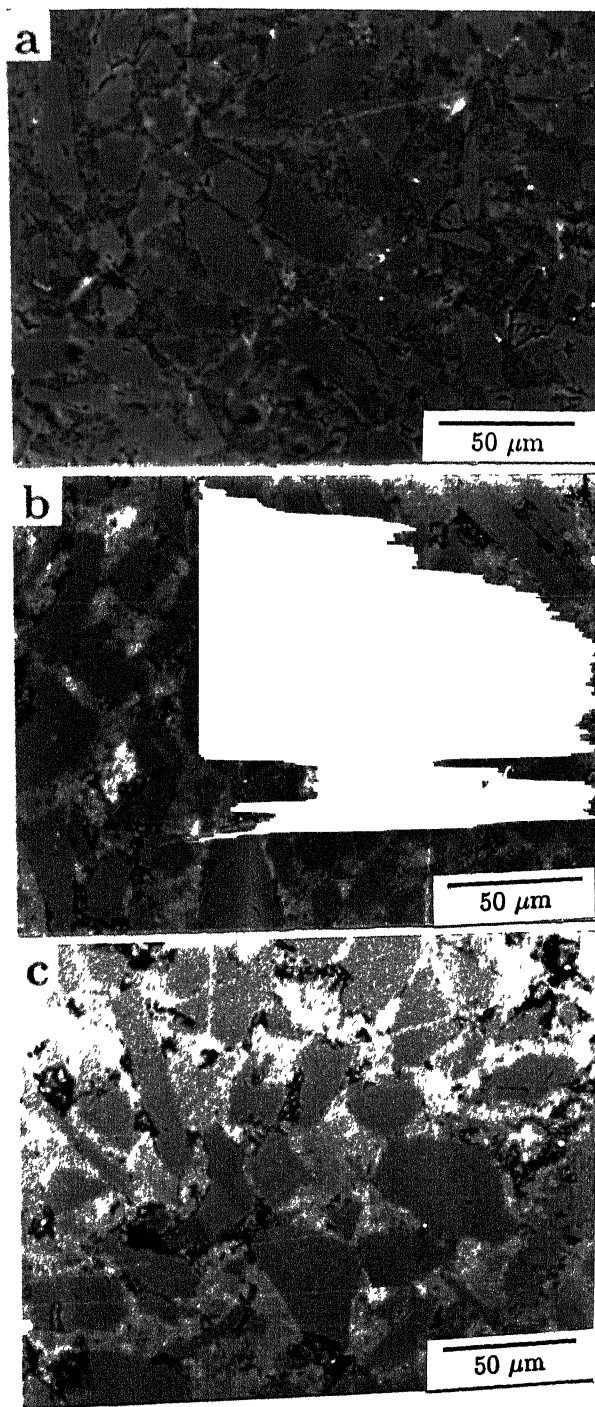
Figure 5.4: Microstructure of (a) 32–45 μm, (b) 45–71 μm and 71–160 μm SiC particulate reinforced composites processed at 1050^oC showing varying amounts of porosity.

slower, resulting in marginally metal-rich composites. On the other hand, the converse is true in the case of finer particulate composites. Similar observations of particulate dependence of infiltration are reported for AlN particulate preforms [4]. These results are also consistent with the predictions of the mathematical model developed by Hillig [5]. However, experimental results can differ from theoretical calculations because: (i) there is a wide variation in the channel size along with the infiltration path, (ii) variation in packing fraction within the preform, (iii) wetting behaviour and (iv) interfacial reactions. Interfacial reactions can significantly alter the infiltration behaviour. For example, in fused Al_2O_3 powder preforms, the infiltration behaviour is not consistent with theoretical predictions [3]. Similarly, Mg vapour deposited on the particulate surface ahead of the growth front can improve wetting behaviour. Additionally, such vapour depositions lead to channelized growth leaving large voids within the composite structure.

5.2.3   Effect of process temperature

The TGA weight gain plot of an Al-2Si-8Mg alloy infiltrated through the intermediate size range is shown in Figure 5.5. The weight gain gradient reveals enhanced nitride formation compared to the base alloy nitridation. The relative improvement of AlN formation is due to fresh metal constantly appearing on the surface to react with the reaction gas and the SiC particle surface serving as secondary nucleation sites.

The intermediate size range (45–71 μm) SiC particulate preform was infiltrated for $6hrs$ at different temperatures (Table 5.3). From the weight gain data it is observed that AlN formation is a strong function of temperature. Aghajanian *et al.* [3] observed an exponential relationship with temperature for the infiltration of Al-10Mg alloy in fused Al_2O_3 particulate preform. Further, the activation energy for infiltration of Al-2Si-8Mg alloy through SiC preform was calculated to be 25 kJ/mol (Figure 5.6). In contrast, activation energy of 330 and 460 kJ/mol was measured for infiltration into AlN particulate preforms of two different particle size from different sources [4]. From the infiltration data provided by Aghajanian *et al.* [3], an activation energy of 91 kJ/mol was calculated for Al_2O_3 preforms.
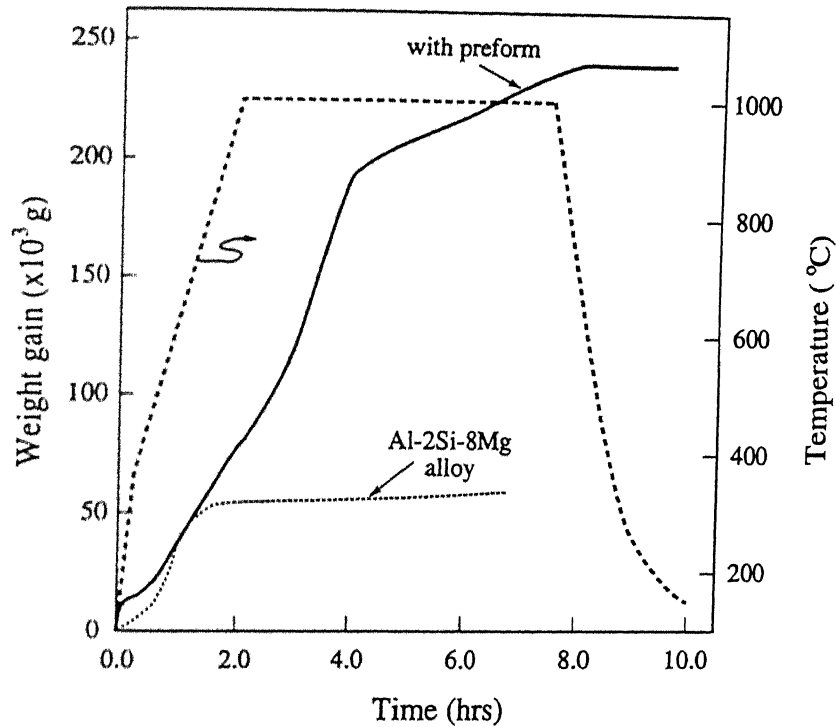
Figure 5.5: TGA plot for an Al-2Si-8Mg alloy infiltrated through SiC preform.

Table 5.3: Effect of process temperature on infiltration rate and nitride formation.

Temperature (^{o}C)	Infiltration rate (mm/hr)	Normalized wt. gain (g/cm^2)
950	1.0	+0.16
1050	1.2	+0.60
1100	1.3	+1.08

The activation energies for infiltration and viscous flow of some systems reported in the literature are listed in Table 5.4. It is well established that physical processes such as viscous flow of fluids or physical adsorption involve an activation energy of <80 kJ/mol, while chemical processes involving rearrangement of atomic bonds require higher energies. For instance, Kurilko *et al.* [7] reported values of 92 and 67 kJ/mol for infiltration of molten lead and Indium through titanium preforms, whereas the activation energies for viscous flow of Pb and In are 8.4 and 6.7 kJ/mol, respectively. Due to the order of magnitude difference in values, it was concluded that the decrease in melt viscosity cannot be rate controlling.

From the above discussion, an activation energy value of 25 kJ/mol compares to a physical
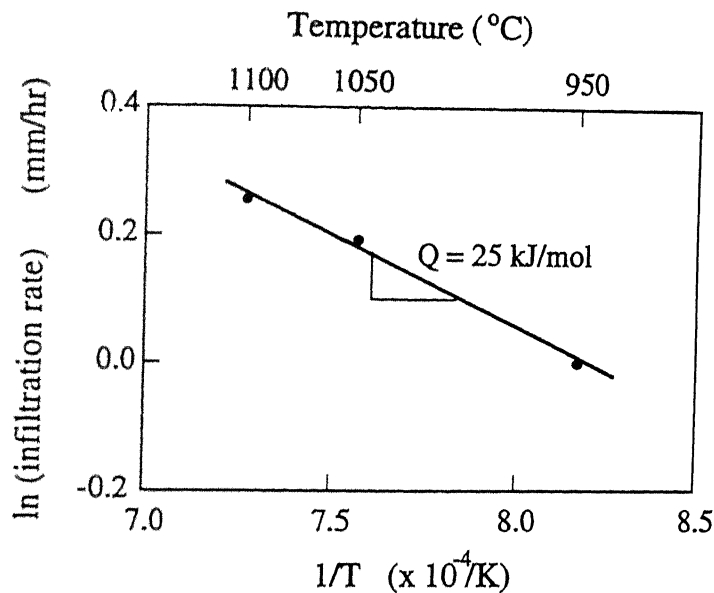
Figure 5.6: Activation energy measurement of Infiltration through SiC preform.

phenomenon rather than a chemical reaction as infiltration rate controlling. The surface tension force is understood to be the driving force for infiltration through pore channels, of which, the contact angle is an integral part. The present value probably corresponds to the decrease in contact angle, caused by variation in the interfacial energies, rather than a decrease in the melt viscosity alone. Conversely, the higher values calculated for Al_2O_3 particulate could refer to interfacial reactions, such as spinel formation. The activation energy of AlN infiltration was measured for two different particle sizes (3.6 and 5.5 μm) from different sources. These infiltration experiments were carried out at very high temperatures ($>1200^oC$), where the kinetics for Al to AlN conversion is very fast, forming a predominantly ceramic matrix. For this reason, the measured activation energy could possibly represent the rate of AlN formation, which in this case also corresponds to the composite growth.

5.2.4 Mechanical properties

The flexural strength and fracture toughness of SiC reinforced AlN/Al composites are shown in Table 5.5. Irrespective of the reinforcement type (continuous or discontinuous), SiC reinforced composites exhibit a typical fracture toughness value of 5.5 $MPa\sqrt{m}$ and an average flexural strength of 185 MPa. There was no significant improvement in properties with SiC

Table 5.4: Activation energy for fluid flow in various systems.

Sr No.	System	Activation energy (kJ/mol)	Remarks
1	Liquid Pb through Cu powder [6]	8.2	Viscosity driven
2	Liquid Pb through Ti powder [7]	92	Reaction driven
3	Liquid In through Ti powder [7]	67	Reaction driven
4	Viscous flow of Pb	8.4	–
5	Viscous flow of In	6.7	–
6	Viscous flow of Al [8]	8.4	–
7	Liquid Al through AlN powder [4]	330, 460	$1200-1240^oC$ Reaction driven
8	Liquid Al through Al_2O_3 powder [3]	91	$850-1000^oC$
9	Liquid Al through SiC powder	25	$950-1100^oC$

(Nicalon) fibre reinforcement. This is probably due to fibre weakening brought about by long exposure at high reaction temperatures. The mechanical properties of SiC/AlN/Al composites are comparable with AlN_p/AlN/Al composites processed at 950^oC. The mechanical properties of SiC particulate reinforced composites have an inverse relation with reinforcement size and processing temperature. On the other hand, the mechanical properties of AlN particulate reinforced composites improve with processing temperature. Significantly, the porosity values in AlN particulate composites are minimal at all processing temperatures.

The fractograph of various AlN/Al composites are shown in Figure 5.7. SiC and AlN particulate composites exhibit transgranular failure (while the matrix shows ductile failure) due to excellent interfacial bonding. In SiC fibre (Nicalon) reinforced composites, little or no pull out was observed. After a few weeks storage in air, deterioration in mechanical properties of all SiC reinforced composites sets in. This degradation is brought about by Al_4C_3 interaction with moisture in air. On the other hand, AlN_p/AlN/Al composites remained stable even after prolonged storage.

Table 5.5: Mechanical properties of SiC and AlN reinforced composites.

(a) Reinforcement effect					
Reinforcement	Infiltration Temperature ($^o C$)	K_{IC} ($MPa\sqrt{m}$)		σ_y (MPa)	
		Max.	Mean	Max.	Mean
SiC platelets	950	6.2	5.7	185	182
SiC particulates	950	7.0	5.5	226	181
SiC fibres	950	6.2	5.5	195	184
AlN particulates	950	5.2	5.0	201	190
(b) Particle size effect					
SiC Reinforcement size (μm)	Infiltration Temp. ($^o C$)	% Porosity	K_{IC} ($MPa\sqrt{m}$)		σ_y (MPa)
			Max.	Mean	Max.	Mean
32 − 45	1050	1.5	4.8	4.4	251	177
45 − 71	1050	3.2	3.9	3.7	145	140
71 − 160	1050	5.1	2.9	2.8	174	125
(c) Temperature effect					
Reinforcement	Infiltration Temp. ($^o C$)	% Porosity	K_{IC} ($MPa\sqrt{m}$)		σ_y (MPa)
			Max.	Mean	Max.	Mean
SiC particulates (45 − 71 μm)	950	0.8	7.0	5.5	226	181
	1050	3.2	4.8	4.7	195	183
	1100	3.8	4.1	4.0	209	186
(d) AlN$_p$ reinforced composites					
Reinforcement	Infiltration Temp. ($^o C$)	% Porosity	K_{IC} ($MPa\sqrt{m}$)		σ_y (MPa)
			Max.	Mean	Max.	Mean
(3 − 20 μm)	950	<1	5.2	5.0	201	190
	1050	<1	6.4	6.2	265	252
	1100	<1	7.7	7.4	320	298

5.2.5   Limitations of SiC reinforced composites

The major limitations of SiC reinforced composites are the residual metal retained in the matrix and the formation interfacial Al_4C_3. While the latter is discussed and possible solutions are suggested later in the chapter, the former limits its high temperature application due to softening of aluminum above $500^o C$. The metal channels are essential from the processing viewpoint, to sustain the wicking of metal to the gas–metal interface. The sustained liquid percolation through microchannels ensures continued composite growth. While the metal within the microstructure cannot be eliminated, its content can be reduced by increased conversion of Al to AlN. This can be achieved by one or a combination of the following:
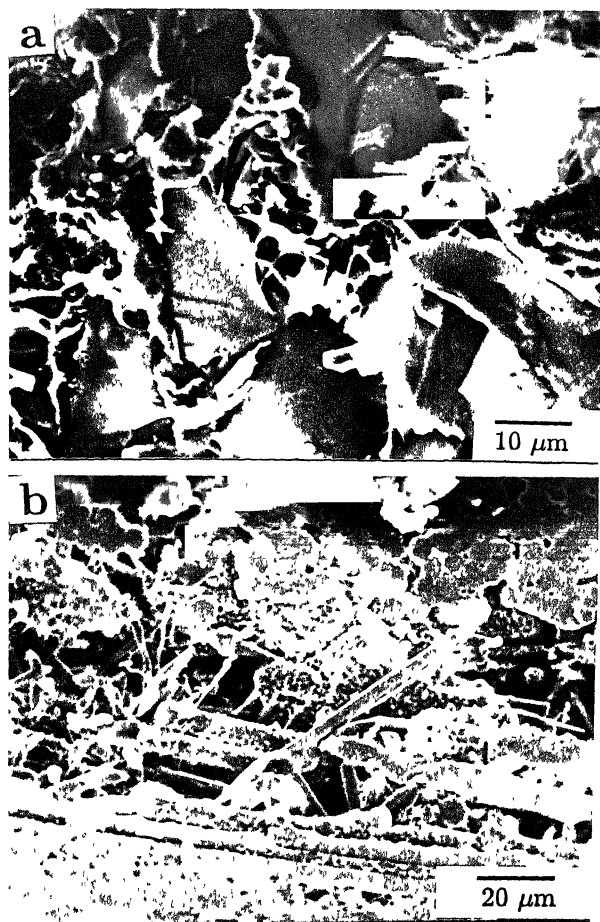
Figure 5.7: Fractographs of (a) SiC particulate reinforced composite showing transgranular failure and (b) Nicalon fibre reinforced composite showing no pull-out.

(i) by modifying the alloy, such as increasing the Mg/Si ratio or incorporating elements such as Li, (ii) decreasing the reinforcement size and (iii) increasing the processing temperature. Processing at higher temperatures not only improves the nitridation reaction kinetics, but also introduces a larger fraction of porosity within the matrix phase. An additional alternative is to convert the aluminum within the composite to a high temperature phase such as an intermetallic. One possible way to achieve this is by reacting the residual aluminum with intermetallics to form aluminides, which offer better high temperature properties. To explore this possibility and analyze the microstructural development in intermetallic preform, Nickel aluminide powder was selected for infiltration.

5.3   Nickel Aluminide reinforced AlN/Al composites

When aluminides are used as reinforcing materials, the liquid melt not only wets the filler spontaneously, but also generates heat due to exothermic interfacial reactions. The governing reaction can be generally expressed as

$$A_w B_x \,_{(s)} + A_y B_z \,_{(s)} + Al \,_{(l)} \xrightarrow{N_2} A_a B_b \,_{(s)} + A_c B_d \,_{(s)} + \cdots + AlN \,_{(s)} + Al \,_{(l)} \qquad (5.1)$$
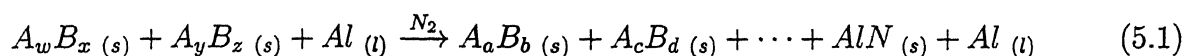
The final microstructure would consist of intermetallics of various stoichiometric/non-stoichiometric compositions [14]. The process thus takes the advantage of both Combustion Synthesis and Pressureless Infiltration. The favourable combination of the two techniques considerably decreases the processing temperature and introduces phases that exhibit greater thermal stability. Since these phases are formed *in situ*, the composite is expected to have good mechanical properties due to clean interfaces. Further improvement is envisaged by ductilizing Nickel aluminide with boron addition [15].

Preliminary experiments of aluminum infiltration through Ni powder preform was not successful between 750–$1050^{\circ}C$. The infiltrating metal was obstructed by the reaction product (a Nickel aluminide) which completely sealed the pore channels, preventing composite growth. For this reason, Nickel aluminide powder was preferred as a preform material, whose average composition lies within the $NiAl_3 + Ni_2Al_3$ phase field (Figure 5.8). The presence of the two
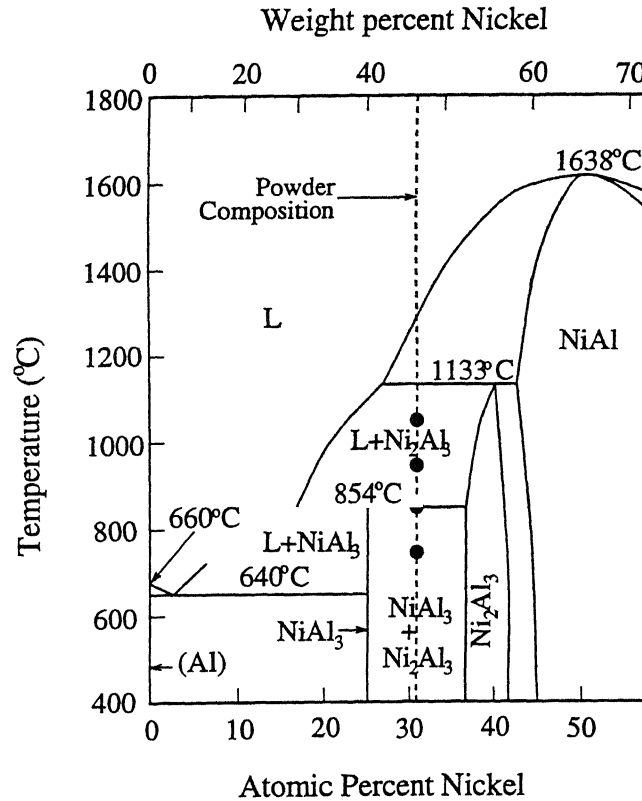
Figure 5.8: Ni–Al phase diagram indicating the composition of aluminide powder and reaction temperatures (marked ●).

phases in the particles was confirmed by both optical microscopy (Figure 5.9) and X-ray analysis (Figure 5.10a).

During reactive infiltration, the nickel aluminide powder undergoes phase changes due to diffusion and/or dissolution controlled reaction taking place at the particle–matrix interface. The reactions occurring at the interface ensures spontaneous spreading of the alloy around the particles. Hence, infiltration rates in these systems are higher than SiC preforms, by a factor of three. Further, the reactions involving intermetallic compounds are exothermic in nature, improving the kinetics of *in situ* reactions at fairly low temperatures at fairly low processing temperatures.
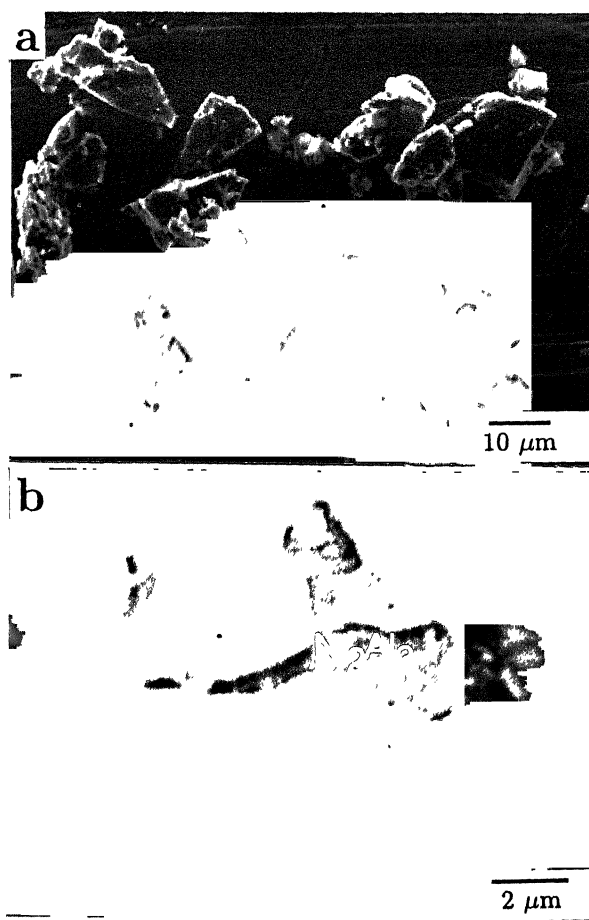
Figure 5.9: Micrographs showing (a) Nickel aluminide particle morphology and (b) a cross-section showing coexistence of Ni_2Al_3 and $NiAl_3$ phases within a particle.
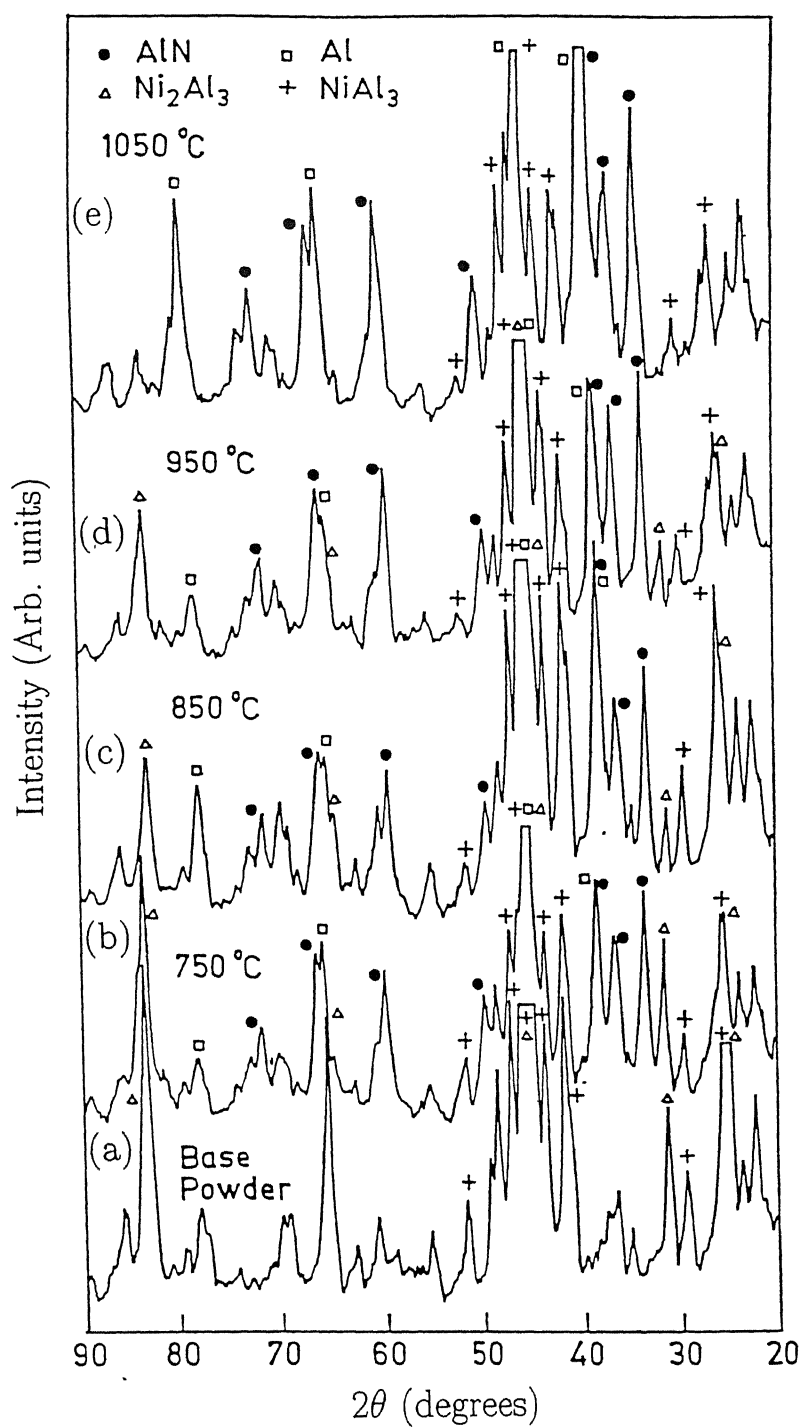
Figure 5.10: X-ray profiles of (a) the base aluminide powder and composites processed at (b) $750^{\circ}C$, (c) $850^{\circ}C$, (d) $950^{\circ}C$ and (e) $1050^{\circ}C$.

5.3.1   Microstructural evolution in infiltrated composites

The X-ray diffraction profiles of the composite infiltrated at various processing temperatures are illustrated in Figure 5.10. From the diffraction patterns it is evident that depending on the processing temperature, the proportion of various phases formed during infiltration shows significant variation. The presence of Ni_2Al_3 and $NiAl_3$ intermetallic compounds is evident in all the composites. However, the height of the Ni_2Al_3 peak decreases with increasing processing temperature and is present in very small proportions in the 1050^oC infiltrated composite. Significant amount of AlN presence is detected even at the lowest processing temperature. The presence of Al is detected in all the composites, but shows a drastic increase in volume fraction at 1050^oC.

Representative micrographs of composites produced at various temperatures are shown in Figure 5.11. With increase in processing temperature, a larger fraction of the inter-metallic is converted to $NiAl_3$, which is consistent with the XRD analysis. The $NiAl_3$ segregates to the particle boundary forming a peripheral rim surrounding Ni_2Al_3. The thickness of the $NiAl_3$ rim gradually increases with increase in process temperature. At 950^oC, it is observed that the $NiAl_3$ particulates do not have a sharply defined morphology, indicating that a dissolution–reprecipitation reaction may be taking place. Further, the $NiAl_3$ extends from the particulates into the matrix. At 1050^oC, Ni_2Al_3 phase disappears from the particulates and $NiAl_3$ solidifies as large, blocky precipitates within the aluminum matrix. The aluminum matrix exhibits an eutectic microstructure of Al and $NiAl_3$ lamellae with large AlN segregations. The shape of the particles does not change significantly until 950^oC, although the size of the particulates shows a gradual increase.

Various phases formed during reactive infiltration were further confirmed by taking microhardness measurements (Table 5.6). At 750^oC, the aluminide is predominantly Ni_2Al_3 (darker phase in Figure 5.11a), surrounded by a thin layer of $NiAl_3$ (brighter phase). The peripheral $NiAl_3$ layer becomes thicker with increase in infiltration temperature up to 950^oC. The
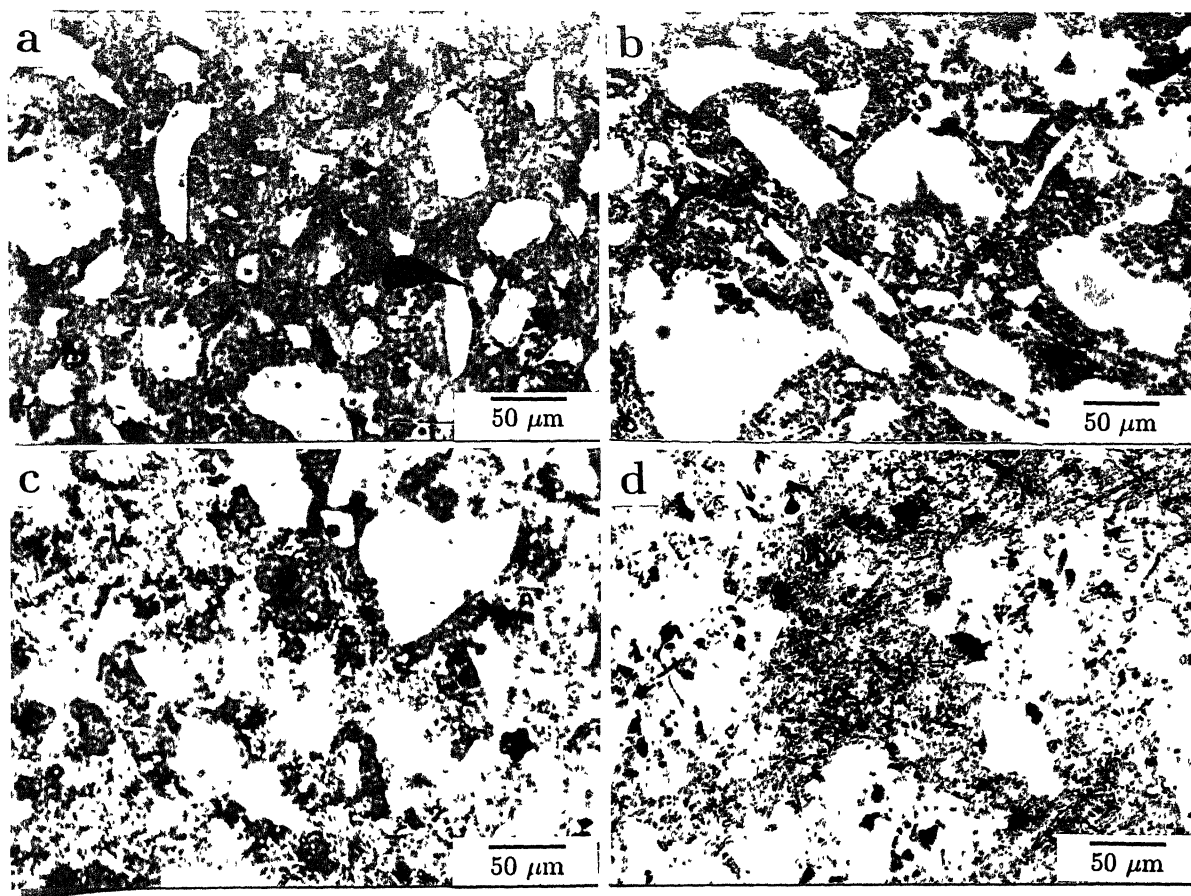
Figure 5.11: Representative micrographs of composites processed at (a) 750°C, (b) 850°C, (c) 950°C and (d) 1050°C showing variation in intermetallic content and particle size. At lower processing temperatures, the structure is predominantly aluminide, whereas at higher temperatures. bulk amount of aluminum and segregation of AlN are evident.

difference in hardness of these two phases is distinctly seen at lower temperatures. However, at higher temperatures, variation in $NiAl_3$ hardness is suggestive of change in Ni to Al ratio. Occasionally, at small pockets of aluminum present in the composite, lower hardness ($\sim$158 VHN) is recorded. At 1050°C, the matrix hardness is moderate ($>$350 VHN) due to

Table 5.6: Microhardness data of Nickel aluminide reinforced composites.

Temperature	Microhardness (VHN)	
(°C)	Ni_2Al_3	$NiAl_3$
750	1095	730
850	1095	857
950	1081	701
1050	–	788

formation of eutectic mixture. The phase changes occurring at various temperatures can be better understood by considering the reactions taking place above and below the peritectic temperature independently. In principle, the desired microstructure can be obtained by varying the composition of the powder and process conditions.

5.3.2   Infiltration below the peritectic temperature

When the process temperature is below the peritectic temperature, Ni_2Al_3 and $NiAl_3$ are stable compounds in the powder preform. A diffusion couple is established across the metal–intermetallic interface when the infiltrating Al comes in contact with the powder particle. Atomic (Ni & Al) displacements take place within the intermetallic such that, the $NiAl_3$ phase segregates to the periphery. The thickness of this layer depends on the kinetics of several reactions listed below. A schematic of the diffusion couple established is presented in Figure 5.12.

Janssen and Rieck [17] have studied the Al–Ni_2Al_3 diffusion couple up to 610°C and found that the Al atoms migrate through the $NiAl_3$ product by vacancy diffusion mechanism. The
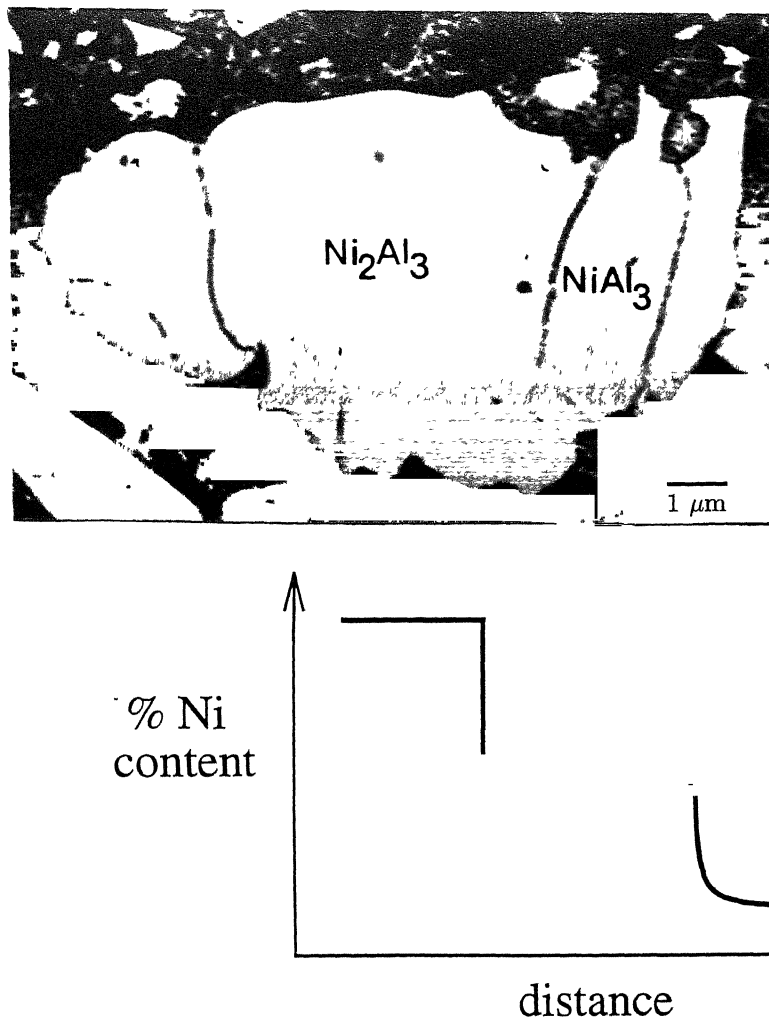
Figure 5.12: (a) Micrograph of a Nickel aluminide particle reacted at $850^{\circ}C$ showing microcracking and preferential segregation of Ni_2Al_3 and $NiAl_3$ phases. (b) The variation of Ni composition profile from the center of the particle into the matrix.

reaction of Al with $NiAl_3$ at the $\langle Ni_2Al_3 \rangle$ | $\langle NiAl_3 \rangle$ interface creates vacancy of Al sites in $NiAl_3$. The reaction can be represented by Kröger–Vink notation as:

$$\langle Ni_2Al_3 \rangle + 3\ Al_{Al} \longrightarrow 2\ \langle NiAl_3 \rangle + 3\ V_{Al}''' + 9\ h^o \tag{5.2}$$
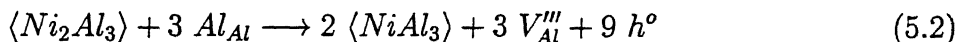
The vacancy diffusion of Al must be charge compensated by the movement of holes within the $NiAl_3$ crystals. The vacancies are destroyed at the $\{Al\}$ | $\langle NiAl_3 \rangle$ interface according to the reaction:

$$\{Al\} + V_{Al}''' + 3\ h^o \longrightarrow Al_{Al} \tag{5.3}$$

In this reaction, the solid state diffusion of Al in $NiAl_3$ is expected to be rate controlling.

On cooling, in regions within the matrix where the alloy composition is hyper-eutectic, pro-eutectic $NiAl_3$ would precipitate before the eutectic composition solidifies at 640^oC according to:

$$\{Al - 3at.\%Ni\} \longrightarrow \langle NiAl_3 \rangle + \langle Al \rangle \tag{5.4}$$
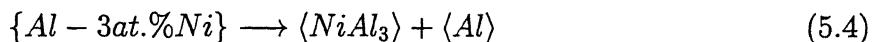
On the other hand, the pockets of Al present in the 750^oC processed composite can be explained as due to pro-eutectic Al precipitation from regions of hypo-eutectic alloy composition before eutectic solidification takes place.

5.3.3 Infiltration above the peritectic temperature

When infiltration takes place above the peritectic temperature, even before the infiltrating metal comes in contact with the aluminide particles, the $NiAl_3$ phase ($\sim 50\ vol.\%$) present in the aluminide particle is converted to Ni_2Al_3 and aluminum (rich in Ni) according to the reaction:

$$\langle NiAl_3 \rangle \longrightarrow \langle Ni_2Al_3 \rangle + \{Al - 15at.\%Ni\} \tag{5.5}$$
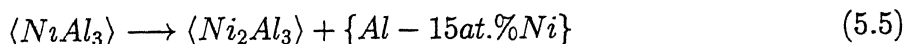
For this reason, the infiltration kinetics is expected to be faster, as the Ni_2Al_3 particle surface is already wetted by the aluminum alloy. When aluminum from the reservoir comes in contact with the preform powder, dissolution of the Ni_2Al_3 phase takes place to achieve local equilibrium within the melt according to the reaction:

$$\langle Ni_2Al_3 \rangle \longrightarrow 2\ Ni_{\{Al\}} + 3\ \{Al\} \tag{5.6}$$
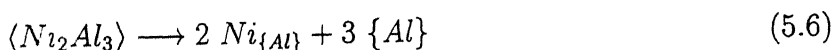
The kinetics of this reaction will depend on the diffusivity of Ni in molten aluminum.

At higher processing temperatures, the kinetics of the above reactions (Equation 5.5 & 5.6) is faster, leading to partial/complete dissolution of nickel aluminide in aluminum. The enhanced diffusivities of Ni in Al at higher temperatures is evidenced by the presence of $NiAl_3$ precipitates well below the preform in the metal reservoir. Due to this excess loss of Ni from the preform domain, a larger volume fraction of Al is present in the 1050^oC processed composite (Figure 5.11d). The final microstructure depends on the relative aluminum alloy composition in the equilibrium phase diagram.

Case I: In regions where the alloy composition falls within the peritectic domain, on cooling, Ni_2Al_3 precipitates out of the Ni rich liquid until the peritectic temperature is reached. At the peritectic temperature, the reverse reaction of Equation 5.5 occurs. But, since all peritectic reactions are sluggish (due to diffusion through solid reaction product) and continued temperature decrease, the remaining liquid precipitates out pro-eutectic $NiAl_3$ until the eutectic temperature is reached. At 640^oC the eutectic mixture solidifies according to Equation 5.4.

Case II: When the composites of the alloy fall within the hyper-eutectic domain, but not within the peritectic composition, $NiAl_3$ precipitation takes place followed by eutectic solidification (Equation 5.4).

Case III: In locations where the alloy composition falls within the hypo-eutectic domain, pro-eutectic Al precipitates occurs followed by eutectic solidification. A preliminary calculation reveals that if complete dissolution of the aluminide phases is assumed the amounts of Ni in the alloy does not exceed 15 $at.\%$. Further, the X-ray analysis and micrographs of composites processed at 1050^oC do not reveal the presence of any Ni_2Al_3. Thus Case I as a possible mechanism can be eliminated. Similarly, since no pro-eutectic Al can be detected Case II can also be ruled out. In which case, the $NiAl_3$ phase present in the 950 and 1050^oC processed composites is due to mechanisms discussed in Case III being operational. Pro-eutectic $NiAl_3$ precipitates as isolated particles and preferentially on undissolved $NiAl_3$ particles forming a $NiAl_3$ rim. The remaining matrix has the eutectic microstructure.

5.3.4 *In situ* AlN formation

The XRD and micro-hardness data reveal a relatively higher proportion of AlN formation in the matrix. The reaction with absorbed Nitrogen takes place according to the reaction:

$$\{Al\} + N_{\{Al\}} \longrightarrow \langle AlN \rangle \qquad (5.7)$$

In SiC reinforced composites, significant amount of AlN formation in the matrix is detected only above $1000^{o}C$ [18]. Contrarily, in the aluminide reinforced composites, greater conversion of Al to AlN is observed even at $750^{o}C$. This large amount of AlN formation can be attributed to the enhanced kinetics due to exothermic heat released by some of the intermetallic reactions. Previously, Ni as an alloying addition was known to refine the oxide structure in DIMOX composite [19]. In the present case, the dissolved Ni may have a catalytic influence on AlN formation.

5.3.5 Mechanical properties

The Flexural strength and toughness data of the composites processed at various processing temperature are shown in Figure 5.13. Aluminide reinforced AlN/Al composites exhibit a decreasing trend with increasing processing temperature. The porosity levels in all the
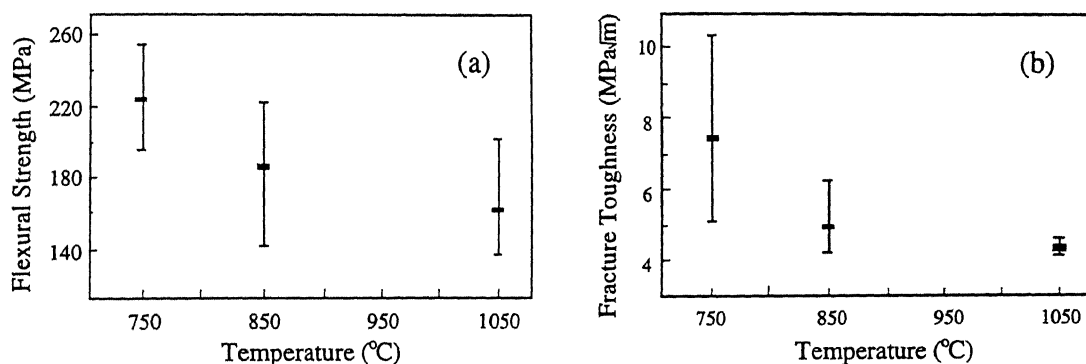
Figure 5.13: (a) Flexural strength and (b) Fracture toughness of Nickel aluminide reinforced AlN/Al composites processed at various temperatures.

composites were less than 1 *vol.%*. Best properties of 255 *MPa* and 10.35 $MPa\sqrt{m}$ are reported for the composites processed at the lowest temperature. The property values are

comparable to SiC or Al_2O_3 reinforced AlN/Al composites infiltrated at 1000^oC [10]. On the other hand, Nickel aluminide powder sintered at 900^oC for 4 hours exhibited a flexural strength of 135 MPa and a fracture toughness value of 3.2 $MPa\sqrt{m}$. The sintered samples had a porosity value of 6 $vol.\%$. The fractographs of intermetallic reinforced composites are shown in Figure 5.14. Nickel aluminide infiltrated at 850^oC clearly indicate that the intermetallic particles exhibit excellent interfacial bonding at lower processing temperatures. In case of 1050^oC processed composite, the intermetallic particles are coarser and show brittle cleavage fracture features. The unreacted residual aluminum exhibits ductile chisel-edge type failure.

The variation in the mechanical properties of infiltrated composite is attributed to the volume fraction and microstructural distribution of Ni_2Al_3, $NiAl_3$, AlN and Al. The fine dispersion of AlN within the $NiAl_3$/Al eutectic microstructure is expected to be the reason for the improved mechanical properties at lower temperatures. With increase in processing temperature, the volume fraction of the harder Ni_2Al_3 phase decreases and a larger fraction of pro-eutectic $NiAl_3$ forms. Further, although the kinetics of AlN formation improves with temperature increase, on cooling from above 950^oC, the AlN formed appear as isolated agglomerates along eutectic grain boundaries. This and the migration of Ni from the preform to the reservoir accounts for the decrease in flexural strength and toughness of composites processed at 1050^oC.

From the correlation between the microstructure and mechanical properties, it is believed that a finer distribution of AlN in the matrix and incorporation of a larger volume fraction of Ni_2Al_3 in the final microstructure would lead to improvement in mechanical properties. To this end, processing at lower temperature and/or having a larger fraction of Ni in the starting powder are recommended. Ideally, it would be possible to entirely eliminate the low temperature phase (aluminum), by judicious choice of intermetallic composition and processing parameters.
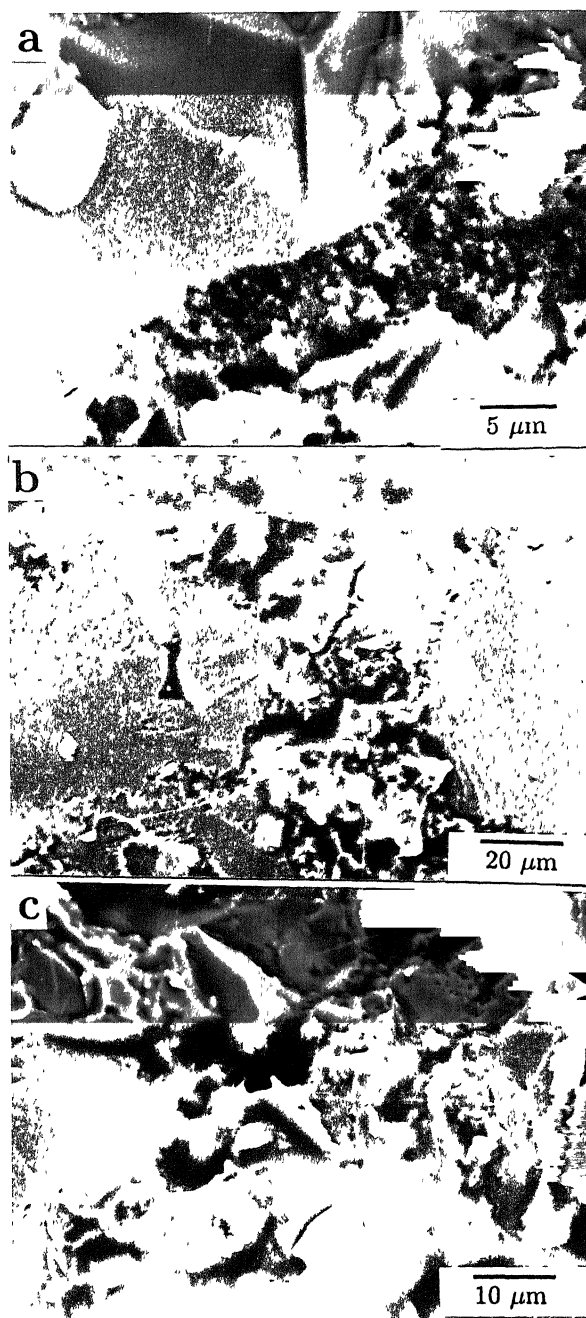
Figure 5.14: Fractographs of intermetallic composite processed at (a) $850^{\circ}C$ showing good interfacial bonding and, $1050^{\circ}C$ showing (b) brittle cleavage failure and (c) plastic deformation of metallic phase

5.4 Interfacial reaction and its prevention

Reactions forming brittle carbide or intermetallics at the matrix–reinforcement interface generally have a detrimental effect on mechanical properties of MMCs. In particulate and monofilament composites, brittle and moisture sensitive Al_4C_3 is formed according to the reaction:

$$3SiC + 4Al \longrightarrow Al_4C_3 + 3Si \qquad (5.8)$$

The reaction and growth kinetics of Al_4C_3 in SiC/Al composites were reported and discussed by several researches [20, 21]. Al_4C_3 is soluble in water and decreases corrosion resistance of the composite. Further, the presence of Al_4C_3 as an interface product limits the mechanical properties of the composite. X-ray diffraction patterns obtained from particulate and platelet infiltrated composites did not reveal any Al_4C_3 formation. However, TEM micrographs clearly identify the presence of Al_4C_3 at the SiC particulate–aluminum interface (Figure 5.3b). The SiC particulate reinforced composites deteriorated into powder after prolonged exposure to moisture. On the other hand, no such degeneration was observed in AlN particulate composites, although they were processed under similar conditions.

Since the formation of Al_4C_3 has been a major limitation for SiC reinforced aluminum matrix composites, some options to limit/inhibit carbide formation is discussed. Usually an increase in Si concentration in the alloy suppresses Al_4C_3 formation [22]. But further lowering of Mg/Si ratio is not desirable from the viewpoint of composite growth, as they decrease the conversion ratio of Al to AlN. The other alternative is to preoxidize the SiC particles (sintering in air) to form a SiO_2 barrier layer on the surface to prevent or delay the reaction between SiC and Al. With extended times the silica rich layer is reduced by the molten metal according to the reaction:

$$3SiO_2 + 4Al \longrightarrow 2Al_2O_3 + 3Si \qquad (5.9)$$
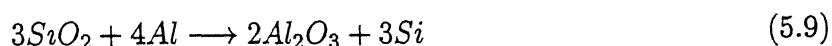
The reduced Si is transported by the liquid melt and precipitated elsewhere [23, 24]. Most of the metallic (Ni, Cu, Ti) or intermetallic (Ni_3Al, ZrB_2, TiB_2) coatings that were attempted in various MMCs have met with limited success [25]. Oxide layers, such as Al_2O_3 and ZrO_2

can be effective barriers, but infiltration is a problem due to poor wettability. One feasible solution is to coat SiC with a nitride, which is both stable in aluminum and easily wetted by the alloy. Prior to infiltration, AlN or Si_3N_4 coatings can be deposited on the filler material by CVD or sol-gel process. In case of CVD, gas mixtures such as ($AlCl_3.3NH_3 + H_2$, $SiH_4 + N_2H_2 + H_2$) or ($SiN_4 + NH_3$) can be used [26, 27]. Alternatively, to deposit a nitride layer *via* sol-gel, a thin film of Al_2O_3 is first deposited and then nitrided at 900–1200°C to obtain AlN [28].

5.5 Summary

The infiltration of various SiC preforms by Al-2Si-8Mg alloy at 950°C has been successfully demonstrated. The secondary nucleation of AlN crystals on SiC fibre is attributed to fibre chemistry. No such nucleation is found on AVCO SVS–6 monofilaments, due to the C-rich surface layer. The infiltration rate in SiC particulate preform increase with particle size and process temperature. An activation energy of 25 kJ/mol was obtained for the infiltration of aluminum through SiC preform. The low activation energy corresponds to a physical phenomenon, such as modification of interfacial energy leading to a decrease in contact angle.

Maximum flexural strength and fracture toughness values of 250 MPa and 7.0 $MPa\sqrt{m}$ are observed for SiC particulate reinforced AlN/Al composites. The decrease in properties recorded with the increase in processing temperature and SiC particle size is primarily attributed to the increased porosity levels within the matrix. The lack of property improvement of fibre reinforced composites over particulate and platelet reinforced composites is attributed to weakening of fibres, due to long exposure at high reaction temperatures. Over a period of time, the $SiC_p/AlN/Al$ composites exhibited deterioration in properties due to Al_4C_3 reaction with moisture. Al_4C_3 formation can be prevented by prior coating of the SiC particulates with AlN on Si_3N_4. The use of directed melt nitrided composites for high temperature application is limited by the residual aluminum within the matrix. To convert the aluminum into a high temperature phase, such as an intermetallic, infiltration through

Nickel aluminide powder was examined.

Reaction infiltration of Nickel aluminide powder preform with an Al-2Si-8Mg alloy yielded near dense composites with Ni_2Al_3, $NiAl_3$, AlN and residual Al as the microstructural constituents at very low processing temperatures. The microstructural evolution at different processing temperatures is better understood in relation to the peritectic reaction. Below the peritectic temperature, $NiAl_3$ and Ni_2Al_3 are stable phases, but diffusion of Al into the aluminide particles modifies the internal structure and composition. At temperatures above the peritectic, large $NiAl_3$ precipitates form due to dissolution and reprecipitation processes. The enhanced formation of AlN at low processing temperatures is attributed to the local exothermic effect and/or catalytic influence of Ni. The mechanical properties (both flexural strength and fracture toughness) of aluminide reinforced composites increase with decreasing process temperature. A maximum flexural strength and toughness values of 225 MPa and 10.35 $MPa\sqrt{m}$, respectively, were measured in composites processed at 750^oC. In principle, it is possible to entirely eliminate aluminum (low temperature phase) from the matrix by judicious choice of intermetallic composition and processing temperature.

References

[1] M. K. Aghajanian, J. T. Burke, D. R. White and A. S. Nagelberg, A new infiltration process for the fabrication of metal matrix composites, *SAMPE Q.*, **20** (1989) 43–46.

[2] V. Laurent, D. Chatain and N. Eustathopolous, Wettability of SiC by Aluminum and Al–Si alloys, *J. Mater. Sci.*, **22** (1987) 244–250.

[3] M. K. Aghajanian, M. A. Rocazella, J. T. Burke and S. D. Keck, Fabrication of metal matrix composites by a pressureless infiltration technique, *J. Mater. Sci.*, **26** (1991) 447–454.

[4] C. Toy and W. D. Scott, Ceramic-metal composite produced by melt inf iltration, *J. Am. Ceram. Soc.*, **73** (1990) 97–101.

[5] W. B. Hillig, Melt infiltration approach to ceramic matrix composites, *J. Am. Ceram. Soc.*, **71** (1988) C96–C99.

[6] K. A. Semlak and F. N. Rhines, Rate of infiltration of metals, *AIME Trans.*, **21** (1958) 325–331.

[7] A. A. Kurilko, C. A. Kurshev, V. A. Rudyuk and Y. V. Naidich, Kinetic laws of infiltration of porous Ti by Pb and In melt, *Proshk. Metall.*, **9** (1984) 35–38.

[8] G. H. Geiger and D. R. Poirier, *Transport Phenomena in Metallurgy*, Addison-Wesley, Reading, U.S.A. (1980) 18.

[9] M. J. Koczak and M. K. Premkumar, Emerging technologies for the in-situ production of MMC's, *J. Met.*, **45** (1993) 44–48.

[10] B. S. S. Daniel, V. S. R. Murthy and G. S. Murty, Metal–Ceramic composites via insitu methods, *J. Mater. Proces. Tech.*, (In press).

[11] H. Scholz and P. Greil, Nitridation reactions of molten Al–(Mg,Si) alloys, *J. Mater. Sci.*, **26** (1991) 669–677.

[12] B. S. S. Daniel and V. S. R. Murthy, Microstructure and Mechanical properties of SiC reinforced AlN/Al composites, *ISIJ Int.*, (communicated)

[13] H. Scholz, R. Günther, J. Rödel and P. Greil. Formation of Al_2O_3 fibre-reinforced AlN/Al-matrix composites by Al(Mg)-melt nitridation, *J. Mater. Sci. Lett.*, **12** (1993) 939–942.

[14] K. A. Philpot, Z. A. Munir and J. B. Holt, An investigation of the synthesis of nickel aluminides through gasless combustion, *J. Mater. Sci.*, **22** (1987) 159–169.

[15] K. Aoki and O. Izumi, Development of ductile intermetallic compound Ni_3Al, *Kinzoku*, **49**[10] (1979) 38–41.

[16] E. Breval, M. K. Aghajanian, J. P. Biel and S. Antolin, Aluminum nitride/Aluminum and Alumina/Aluminum composites produced by the directed oxidation of Aluminum, J. Am. Ceram. Soc., **76** (1993) 1865–1868.

[17] M. M. P. Janssen and G. D. Rieck, Reaction Diffusion and Kirkendall-effect in the Nickel–Aluminum system, *AIME Trans.*, **239** (1967) 1372–1385.

[18] B.S.S.Daniel, *Processing of MMC's/CMC's by directed melt nitridation*, M.E.(I) Thesis, I.I.Sc., Bangalore, June 1992.

[19] A.Guha and V.S.R.Murthy, Refinement of directed melt oxidized structures, *Bull. Mater. Sci.*, **19** (1996) 1117–1124.

[20] H. Ribes, M. Suery, G. L'Esperance and J. G. Legoux, Microscopic examination of interface region in 6061–Al/SiC composites reinforced with as-received and oxidized SiC particles, *Metall. Trans.*, **21A** (1990) 2489–2496.

[21] D. J. Lloyd, The solidification microstructure of particulate reinforced Aluminum/SiC composites, *Comp. Sci. Tech.*, **35** (1989) 159–179.

[22] S. Towata and S. Yamada, Interaction between SiC fibres and aluminum alloys, *J. Japan Inst. Metals*, **47**[2] (1983) 159–165.

[23] E. Manor, H. Ni, C. G. Levi and R. Mehrabian, Microstructure evolution of SiC/Al_2O_3/Al alloy composites produced by melt oxidation, *J. Am. Cer. Soc.*, **76** (1993) 1777–1787.

[24] V. S. R. Murthy and A. Deepak, Microstructure and mechanical properties of SiC–Al–Al_2O_3 composites prepared by directed melt infiltration, *Brit. Ceram. Trans.*, **95** (1996) 173–176.

[25] R. K. Everett, Deposition techniques for MMC fabrication, *Metal matrix composites: Processing and interfaces*, ed. R. K. Everett and R. J. Arsenault, Academic press, U.S.A. (1991) 103–119.

[26] K. K. Yee, Chemical vapour deposition of aluminum nitrides, *Intl. Metals Rev.*, **23** (1978) 19–27.

[27] M. G. Hocking, V. Vasantasree and P. S. Sidky, *Metallic and Ceramic coatings: Production, High-temperature properties and Applications*, Longman Scientific & Technical, New York, U.S.A. (1989) 115.

[28] M. W. Russel and E. P. Giannelis, in *Synthesis and Processing of Ceramics*, ed. W. E. Rhines, T. M. Shaw, R. J. Gottschall and Y. Chen, Elsevier, London, U.K. (1987), 207.

Chapter 6

Mathematical Modelling of Infiltration

6.1 Introduction

Liquid percolation through porous media, such as the movement of water in soils, has been the subject matter of considerable interest to Geologists and Civil Engineers. In recent years, metal matrix composites have been successfully produced by infiltrating molten metal through porous ceramic preforms [1, 2]. When the infiltrated metal solidifies, the resulting composite has the dual advantage of high reinforcement content and net-shape fabrication.

The prime obstacle to infiltration is the non-wetting nature of molten metals on ceramic substrates. The contact angle 'θ' serves as a good measure of *wettability*, which is expressed by the Young's equation as [3]:

$$\gamma_{lv} \cos \theta = \gamma_{sv} - \gamma_{ls} \qquad (6.1)$$
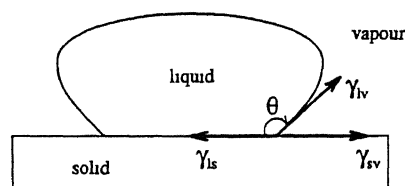
Figure 6.1: Schematic representation of liquid-solid-vapour interface depicting a non-wetting condition.

where γ_{lv}, γ_{sv} and γ_{ls} represent the liquid–vapour, solid–vapour and solid–liquid interfacial energies, respectively. The contact angle is usually measured by the Sessile drop technique, where measurements are made on a liquid droplet placed on the ceramic substrate after equilibrium has reached (Figure 6.1). When $\theta > 90°$ ($0 > \cos \theta \geq -1$), the liquid droplet

on the ceramic substrate shrinks and the condition is termed *non-wetting*. Under these conditions, metal penetration through preform pore channels is possible only when an external pressure is applied. On the contrary, when $\theta < 90°$ $(0 < \cos\theta \leq 1)$, spontaneous 'wetting' of the ceramic substrate occurs. The value of the contact angle is determined by the choice of alloy, substrate material, atmosphere and temperature. Further, the criteria for wetting are: (i) $\gamma_{sv} > \gamma_{ls}$ and/or (ii) some reaction takes place at the interface resulting in spontaneous spreading of the alloy. If either condition is satisfied, pressureless infiltration of a porous preform can occur. In this chapter, the mathematical modelling of the pressureless infiltration phenomenon is presented.

The initiative to mathematically model the infiltration phenomenon is derived from the necessity to qualify the various variables affecting the infiltration process and to quantify their influences. Such an effort will help in optimizing the process and bring down the number of sampling experiments usually undertaken. For instance, the preform alone can be characterized based on its surface chemistry, packing fraction, pore size and pore shape. Additional processing variables include, the alloy composition, reaction atmosphere, process temperature and time. An optimization of the process would necessitate a quantitative understanding of the inter-relationship between the process variables and the physical properties, such as the contact angle, density, viscosity, permeability and surface tension. The ideal model would relate the process fundamentals to the external processing variables and realistically predict the composite growth. Due to the large number of variables involved and the lack of data, the objective of the present work is confined to understanding the physical phenomenon and developing a realistic model based on the porous-bed approach.

6.2   Previous work on porous preform infiltration

Infiltration of porous ceramic preforms can be classified depending on whether or not an external pressure is applied to force the molten metal into the pore channels. In principle, it is possible to infiltrate both wetting and non-wetting alloys under an appropriate externally applied pressure. But to reduce porosity and improve interfacial bonding, which would in turn

enhance load bearing capability of the composite, a favourable contact angle in preferred [4]. Several investigations were carried out to study the effect of processing parameters such as pressure, temperature and alloy composition on the infiltration kinetics [5, 6]. Maxwell *et al.* [7] have mathematically modelled the pressure infiltration of aluminum into SiC particulate compacts based on the capillary model, which is described later in the text. Contrary to pressure infiltration, where the applied pressure has to overcome the surface tension force, in pressureless infiltration, due to the favourable contact angle the surface tension becomes the driving force. Two approaches are possible for the modelling of pressureless infiltration phenomenon, namely the capillary-tube-bundle model and the porous-bed model. Until now, no mathematical model has been developed based entirely on the porous-bed phenomenon. In the following sections, the models available in literature are discussed and their relative merits critically examined.

6.2.1   Capillary-tube-bundle model

The capillary tube bundle model is popular due to its simplicity and ability to predict fluid flow after certain modifications. The model equates the porous media with its intricate and random network of pores to a representative bundle of parallelly arranged capillary tubes. The equivalent pore radius and height of the representative capillary have to be calculated for the respective preform.

Flow through a porous media was first modelled as a liquid rise in a capillary by Washburn in 1921 [8]. Poiseuille's law [9] for flow through a cylindrical conduit expresses the volume rate of flow through a height h as:

$$\frac{dV}{dt} = \frac{\pi r^4 dp}{8\mu h} \tag{6.2}$$

where r is the capillary radius, μ is the viscosity and dp is the pressure difference driving the liquid through the capillary. The pressure difference experienced at the curved liquid meniscus can be expressed according to Kevins law as [10]:

$$dp = \frac{2\gamma_{lv} \cos \theta}{r} \tag{6.3}$$

For a narrow cylindrical capillary bore, $dV = \pi r^2 dh$. Equation 6.2 can be rewritten as:

$$\frac{dh}{dt} = \frac{r\gamma_{lv}\cos\theta}{4\mu h} \tag{6.4}$$

On integrating with respect to time and applying the limit, at time $t = 0$, $h = 0$, the infiltration height is expressed as:

$$h = \left[\left(\frac{r\gamma_{lv}\cos\theta}{2\mu}\right)t\right]^{\frac{1}{2}} \tag{6.5}$$

Washburn used water and mercury to experimentally validate the above expression, by predicting the liquid rise in capillary tubes of various bore diameters as a function of time.

Britten [11] was the first to develop the equation of motion for the advancement of the liquid front in a capillary tube. He identified the forces acting on the liquid column as the surface tension force, the gravitational force, Poiseuille's viscous drag force and the end drag force (Figure 6.2). These forces balance the liquid column and are expressed as follows:
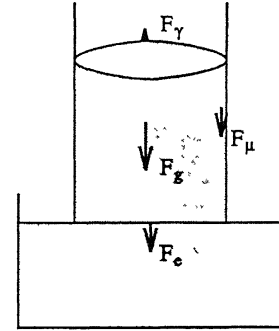
Figure 6.2: Schematic representation of forces acting on a liquid column.

$$F_\gamma = 2\pi r\gamma_{lv}\cos\theta \tag{6.6}$$

$$F_g = -\pi r^2 \rho g h \tag{6.7}$$

$$F_\mu = -8\pi\mu h\frac{dh}{dt} \tag{6.8}$$

$$F_e = -\frac{1}{4}\pi r^2 \rho\frac{dh}{dt} \tag{6.9}$$

The ensuing momentum balance is a second order non-linear differential equation, which may be represented as:

$$h\frac{d^2h}{dt^2} + \frac{5}{4}\left(\frac{dh}{dt}\right)^2 + Ah\frac{dh}{dt} + gh = B \tag{6.10}$$

where $A = \frac{8\mu}{\rho r^2}$ and $B = \frac{2\gamma_{lv}\cos\theta}{\rho r}$. Ligenza and Bernstien [12] arrived at a similar expression, but with additional terms accounting for the column of air displaced by the moving liquid

front. In assuming a narrow capillary bore and therefore low flow rates, the rate of change of momentum and the end-drag effect terms were neglected. The solution of the resulting first order differential equation approximates to the familiar Washburn equation (Equation 6.5).

Semlak and Rhines [13] extended the treatment to infiltration of molten metals, such as Cu, Ag and Pb into porous compacts of Cu and Fe. They approximated the pore channels to a chain of semi-circular paths, which increased the effective capillary length by a factor of $\frac{\pi}{2}$. Assuming the characteristic pore radius (R_c) to be one-fourth the inter-particle distance resulted in good predictions. The modified expression is:

$$h = \frac{2}{\pi} \left[\left(\frac{R_c \gamma_{lv} \cos \theta}{2\mu} \right) t \right]^{\frac{1}{2}} \tag{6.11}$$

Difficulties arose when attempts were made to use the above expression for metal infiltration through ceramic preforms. Hillig [14] accounted the over-estimate in infiltration height to the variation in the pore diameter along the pore channel. A simple assumption of the pore channel being made-up of narrow cusps of radius 'r_1' and length 'l_1' linking larger chambers of radius 'r_2' and length 'l_2', introduced a correction factor (Z_{cor}) to the Washburn's equation, such that,

$$h = \left[\left(\frac{R_c \gamma_{lv} \cos \theta}{2\mu Z_{cor}} \right) t \right]^{\frac{1}{2}} \tag{6.12}$$

where Z_{cor} is expressed as:

$$Z_{cor} = \left(\frac{l_2}{l_1} \right)^2 \left[1 + \left(\frac{P_2}{P_1} \right) \left(\frac{l_1}{l_2} \right) \left(\frac{r_2}{r_1} \right)^2 \right]$$

In the above expression, P_1 and P_2 are the volume fraction of the narrow and larger voids. Toy *et al.* [15] found good agreement with this model in their experiments of AlN preform infiltration with aluminum in Nitrogen atmosphere.

Further discrepancy in the model was detected by Muscat and Drew [16] while attempting to model the infiltration kinetics of aluminum into TiC. They accounted the variation as due to: (i) the complexity in the pore structure and (ii) the transient behaviour of the contact angle, 'θ'. The latter is due to reactions taking place at the metal–ceramic interface. An experimentally measurable parameter, *tortuosity* (T) was introduced to account for the

complexity in the pore structure. Additionally, the contact angle was expressed as a time dependent function. The modified expression for infiltration height is given as:

$$h = \left[\left(\frac{1}{T}\right) \frac{r\gamma_{lv} \cos\theta_o (1 - ae^{-ct^n})}{\mu} t \right]^{\frac{1}{2}} \tag{6.13}$$

where θ_o is the equilibrium contact angle, and a, c and n are constants to be determined experimentally.

Martin *et al.* [17] rewrote Brittin's equation of motion (Equation 6.10) in dimensionless form and were able to delineate the viscous and invisid flow conditions. They identified an infiltration parameter,

$$\Phi = \frac{r\gamma_{lv} \cos\theta}{2\mu} \tag{6.14}$$

which is also the constant term in Washburn's equation (Equation 6.5). The infiltration parameter was useful in comparing infiltration kinetics in different metal–ceramic systems. On the other hand, their prediction of infiltration rate of aluminum into a 10 μm SiC bore was much faster than in reality. No reason was provided for the overestimate.

Finally, it is noted that in predicting the liquid rise in a porous preform, the basic form of the Washburn equation for flow in a capillary tube is maintained. The corrections made by various authors at different stages were to account for: (i) the variation in the pore characteristics and (ii) the transient nature of the wetting phenomenon. It is mathematically impossible to describe the pore structure within the preform due to its inherent complexity and randomness. Additionally, the transient nature of the wetting phenomenon is further compounded by the moving growth front. A phenomenologically better approach is to model the metal rise in the preform as a flow through porous-bed.

6.2.2   Porous-bed model

The porous-bed model is based on the empirical relationship developed by Darcy for defining liquid flow through various sands [18]. The percolation rate (v) is related to the pressure

gradient according to the relation:

$$v = \frac{k}{\mu}\left(\frac{dp}{l}\right) \tag{6.15}$$

where k is the *permeability*, a single parameter which embodies all the physical characteristics of the pore structure. The advantage of Darcy's law is its amenability to independently characterize the preform at room temperature with a liquid of known viscosity.

In principle, permeability represents the resistance of the non-uniform pore structure to fluid flow. There is no general correlation between permeability and porosity, although several have been suggested. A useful relationship was derived by Scheiddegger [19] by considering the porous-bed as a bundle of parallel capillaries. The permeability is then expressed as:

$$k = \frac{\epsilon^3}{T\,S^2} \tag{6.16}$$

where S is the surface area and T is the tortuosity, which is defined as the ratio of the true path of fluid flow and the straight line path between two points. Muscat and Drew [16] had earlier used this expression for permeability in Darcy's equation to derive Equation 6.13. The details of the porous-bed model developed in the present work is provided later in the text.

6.3   The present work

6.3.1   Process description

The detailed description of the infiltration phenomenon through porous preform is given in chapter 5. The intermediate stages of composite growth are shown in Figure 6.3. When the crucible containing the preform material and the alloy is heated above the liquidus temperature, the metal experiences a volume expansion of $\sim$10 *vol.%*. This expansion forces the alloy to wet the filler material placed above. Once the preform surface is wetted, the alloy begins to rise through the pore channels due to capillarity. A dynamic equilibrium is maintained between the surface tension force and the preform resistance. The process of
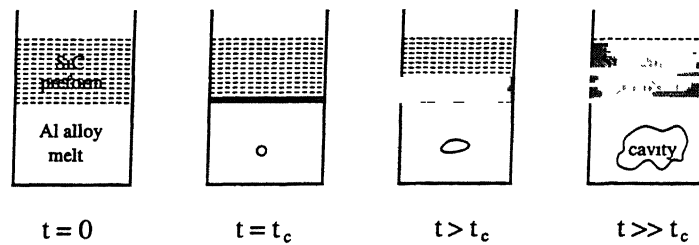
Figure 6.3: Schematic representation of stages of composite growth.

metal infiltration continues until either: (i) all the pores in the SiC preform are filled by the infiltrating metal or (ii) all the alloy in the reservoir has infiltrated into the preform. The displacement of molten metal from the reservoir to the preform appears as a growing cavity within the reservoir. The cavity could have nucleated from any blow hole within the cast alloy. Since Mg and Al are volatile species at the reaction temperature ($\sim 1000^{o}C$), equilibrium is quickly established at the gas–metal interface.

Thus, the preform infiltration is phenomenologically a porous-bed situation than a liquid rise through a bundle of parallel-arranged capillary tubes. To derive a mathematical model based on the porous-bed phenomenon, it is necessary to have a means to describe the fluid flow field within the porous media. The development and analysis of such a model is described in the following sections.

6.3.2   Assumptions in modelling

From a description of the process, it is obvious that metal infiltration through porous ceramic preform is a complex phenomenon. The Mg loss form the surface, AlN formation within the matrix and wettability, compounded with the lack of high-temperature data, make it an impossible task to simulate the process exactly form first principles. Therefore, to describe the process *via* a suitable mathematical model, the following simplifying assumptions were made.

1. Owing to axial symmetry, no variation in flow properties in the θ-direction has been assumed.

2. The transient infiltration phenomenon with the liquid growth front moving in the axial direction is approximated to a mobile planar surface.

3. The fluid flow is essentially laminar, incompressible and Newtonian.

4. The system is assumed to be isothermal. The effects of the furnace heat-up period, the exothermic heat generated due to chemical reaction and related buoyancy effects are negligible.

5. Thermo-mechanical properties of the fluid, such as ρ, μ and γ_{lv} are taken to be constant.

6. At time $t = 0$, the preform is wet by the alloy and the liquid-solid contact angle θ, is assumed to remain a constant.

7. The surface tension force is the driving force for infiltration, which overcomes the resistance due to preform and gravity.

6.3.3 Mathematical Formulation

Due to the cylindrical geometry of the crucible, the flow variables are expected to obey axial symmetry (Figure 6.4). Hence, the governing differential equations are set in 2-dimensional cylindrical polar coordinate as below:
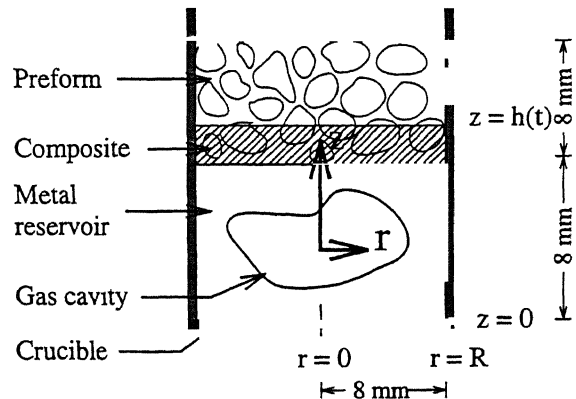
Figure 6.4: Schematic showing crucible configuration and co-ordinate axis.

Equation of continuity:

$$\frac{\partial u}{\partial z} + \frac{1}{r}\frac{\partial}{\partial r}(rv) = 0 \qquad (6.17)$$

Equation of motion in the axial direction:

$$\frac{\partial}{\partial t}(\rho u) + \frac{\partial}{\partial z}(\rho u u) + \frac{1}{r}\frac{\partial}{\partial r}(r\rho uv) = -\frac{\partial p}{\partial z} + \frac{\partial}{\partial z}\left(\mu\frac{\partial u}{\partial z}\right) + \frac{1}{r}\frac{\partial}{\partial r}\left(r\mu\frac{\partial u}{\partial r}\right) + S_u \qquad (6\ 18)$$

Equation of motion in the radial direction:

$$\frac{\partial}{\partial t}(\rho v) + \frac{\partial}{\partial z}(\rho u v) + \frac{1}{r}\frac{\partial}{\partial r}(r\rho v v) = -\frac{\partial p}{\partial r} + \frac{\partial}{\partial z}\left(\mu\frac{\partial v}{\partial z}\right) + \frac{1}{r}\frac{\partial}{\partial r}\left(r\mu\frac{\partial v}{\partial r}\right) - 2\mu\frac{v}{r^2} + S_v \quad (6.19)$$

where S_u and S_v are the source terms that embody body forces such as, the surface tension force, preform resistance, etc. S_u and S_v are zero within the metal reservoir, while at the liquid–gas interface and within the preform S_u and S_v assume finite non-zero values. Appropriate expressions for S_u and S_v are provided in Table 6.2.

An anisotropic permeability for the porous-media can be calculated according to Carman-Kozeny equation which states that [20]:

$$k = \frac{\epsilon^3}{D_l(1-\epsilon)^2} \quad (6.20)$$

where D_l depends on the morphology of the porous media. Although the exact value of D_l is still a matter of debate, Minakawa et al. [21] have experimentally estimated that,

$$D_l = \frac{180}{d^2} \quad (6.21)$$

where d is a constant of the order of 10^{-4}. The present work is unique in its attempt to model the fluid flow in the preform along with the alloy in the reservoir below.

Initial and Boundary conditions

The initial and boundary conditions used to solve the above second order non-linear partial differential equation are given below:

At time $t = 0$;

$$0 \leq r \leq R; \quad 0 \leq z \leq h(t=0); \qquad u = 0; \quad v = 0 \quad (6.22)$$

At time $t > 0$;

$$r = 0; \quad 0 \leq z \leq h(t); \qquad \frac{\partial u}{\partial r} = 0; \quad v = 0 \quad (6.23)$$

$$r = R; \quad 0 \leq z \leq h(t) \text{ and } z = 0; \quad 0 \leq r \leq R; \qquad u = 0; \quad v = 0 \quad (6.24)$$

$$z = h(t); \quad 0 \leq r \leq R; \qquad \qquad \frac{\partial u}{\partial z} = 0; \quad \frac{\partial v}{\partial z} = 0 \qquad (6.25)$$

Initially $(t = 0)$, the fluid is at rest within the computational domain (Figure 6.4). At $t > 0$, due to axial symmetry, the radial gradient of axial velocity and radial velocity are zero. Along the walls of the crucible a no-slip condition is prescribed. At the growth front $(z = h(t))$, the axial gradient of axial and radial velocity components are zero.

Numerical solution procedure

An actual laboratory scale experimental configuration has been used for the purpose of mathematical modelling (See Figure 6.4). As pointed out earlier, the differential equations together with the boundary conditions applied indicate that this is an unsteady state moving boundary problem. The governing flow equations for the above system configuration has been solved *via* a control volume based finite difference procedure, using the SIMPLE algorithm of Patankar and Spalding [22]. The flow vectors are computed using a fully implicit marching integration procedure.

Discretization equation: The discretization equation for a variable $\phi(u, v, p)$ at any grid point P is represented in terms of its neighbours $(E, W, N$ and $S)$ as:

$$A_P \phi_P = A_E \phi_E + A_W \phi_W + A_N \phi_N + A_S \phi_S + A_P^o \phi_P^o + S \qquad (6.26)$$

where A's represent the coefficient containing both the convection and diffusion terms of ϕ and S is the source term. ϕ_P is related to the previous time step through a weighing function, A_P^o. The linear discretization equations for all control volumes are solved using a line-by-line solution scheme incorporating the Tri-Diagonal Matrix Algorithm (TDMA).

Grid system: Keeping in mind the axi-symmetric cylindrical coordinate system, initially a variable $(NI \times NJ)$ grid is laid in the metal reservoir as shown in Figure 6.5. The moving boundary is accounted for by laying a fresh grid at the beginning of every time step. While there is no change in the number of grids in the
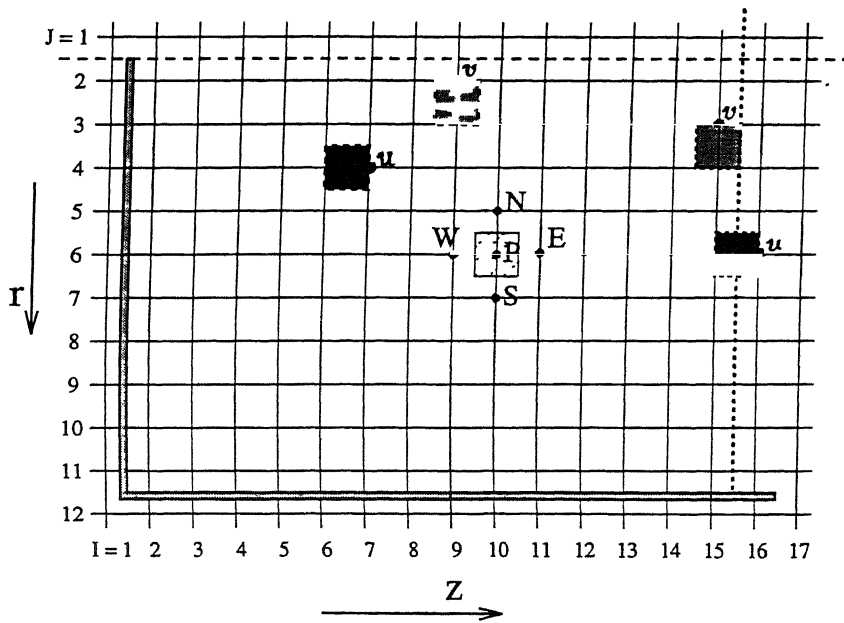
Figure 6.5: A representative 17 X 12 grid system showing relative positions of control volumes for pressure (hatched), u velocity (shaded dark) and v velocity (shaded light).

radial direction ($NJ = 12$, $\Delta r = 0$ for $t \geq 0$), additional grids are introduced in the axial direction, to include the preform domain infiltrated by the molten metal. At time $t = 0$, $NI = 17$. For the succeeding time steps, $NJ \geq 17$, with care being taken such that the grid spacings in the axial direction is not significantly altered.

Control volume: An enlarged portion of the 2-dimensional grid at time $t = 0$, is shown in Figure 6.6. For the gird point P,
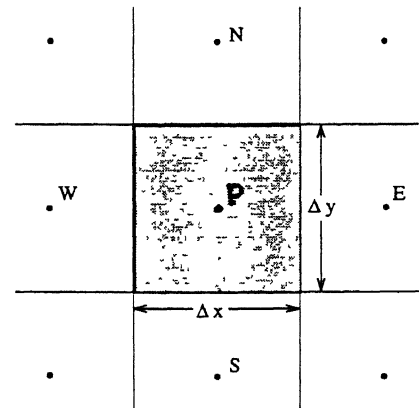
Figure 6.6: A representative control volume shown in relationship to its neighbours.

points E, W, N and S are the neighbours. The control volume represented by the point P is shown by dashed lines. The faces of the control volume lie mid-way between neighbouring grid points. The control volume has dimensions of ΔX and ΔY in the axial and radial direction, respectively. Due to the axial symmetry, the extent of the control volume along θ is one radian. To prevent situations where a wavy pressure field may be felt like a uniform

pressure field by the momentum equation, a staggered grid is employed for velocity calculations. This is accomplished by shifting the u and v velocity control volumes by half a grid in the axial and radial direction, respectively, as shown in Figure 6.5.

For the control volume lying within the the preform domain, the liquid can only occupy the space within the pores. To account for the void fraction in the macroscopic model, the coefficients in the discretization equation (A_E, A_W, A_N and A_S) were calculated in the normal way and then modified by multiplying by the void fraction (ϵ). In case of the velocity control volumes lying at the preform–metal interface, care was taken to modify only those faces and volume fraction that lie within the preform (Figure 6.5). To maintain internal consistency, it was essential that the adjacent control volume faces were modified the same way.

Time step factor: From the results of the capillary bundle model, the composite growth profile exhibits a parabolic behaviour [14]. To capture the rapid changes in axial velocity during the initial stages of growth, time is incremented in accordance to a geometric series, such as:

$$t_n = ar^n \tag{6.27}$$

where a is a constant and n is a positive integer, referring to the time step. In the present computation, $a = 10$ and $r = 3$, unless mentioned otherwise.

Surface tension force: The surface tension force embodied in the axial momentum equation, is actually not a body force. It is a function of the contact angle and acts along the liquid–solid–gas interface. The value of γ_{l_v} (N/m) at 1000^oC is calculated from the expression given by Rhee [23]:

$$\gamma_{l_v} = 0.948 - 0.202 \times 10^{-3}(T) \tag{6.28}$$

Since the present model is macroscopic and control volume based, the surface tension force was calculated for per unit cross-sectional area of the preform and incorporated as a body force in the surface control volumes as:

$$ST_{act} = \frac{3\pi(1 - \epsilon)}{2d}\gamma_{l_v}\cos\theta \tag{6.29}$$

where d is the diameter of the particle. This calculation is shown in Appendix A.

The surface tension force is a very large value compared to the other terms in the discretization equation. To prevent the computation from diverging, an under-relaxation for surface tension(ST) is employed such as:

$$ST = \alpha ST_{old} + (1-\alpha)ST_{act} \qquad (6.30)$$

where $\alpha = 0.95$ and ST_{act} is the actual value of Surface tension. At the end of every iteration, ST_{old} is augmented to the current value of ST. In employing the above under-relaxation function, initially the value of ST increases rapidly and gradually approaches ST_{act}. To simulate the condition of preform wetting in the initial time step, one control volume depth of the preform is treated as immersed in the liquid. Thus, the surface tension force is countered by the preform resistance to flow.

Outflow boundary condition: In the absence of a meaningful boundary condition for the axial velocity at the surface ($z = h(t)$), the overflow boundary condition is resorted to [24]. The boundary condition at the moving growth front is implemented by setting the diffusion coefficient(Γ_E) on the east wall of the boundary control volume as small (zero). This implies that the down-stream value (east of point P), has no influence on the calculation of u at P. Such an assumption is valid if the Peclet's number ($= \rho u \delta x / \Gamma$) is large, reflective of a one-way flow behaviour.

Convergence criterion: In the present numerical approach, the values of u, v and p at individual grid points are successively updated in each iteration. In such a numerical technique, convergence is supposed to have attained when the independent variables at individual grid points do not change with any further iteration. A more rigorous convergence criterion would be to minimize the sum of the absolute value of residual (Ω) in each control volume, which is expressed as:

$$\Omega = A_E \phi_E + A_W \phi_W + A_N \phi_N + A_S \phi_S - A_P \phi_P + S_u \qquad (6.31)$$

The mean mass of a control volume is $\sim 5 \times 10^{-6} kg$. In the present computation, a convergence criterion of $\leq 10^{-15} kg$ for the residual mass is employed.

Table 6.1: Compilation of Data used in the present model.

Sr. No.	Property	Value
1	Density (ρ)	$2700\ kg/m^3$
2	Surface tension (γ_{lv})	$0.691\ N/m$
3	Viscosity (μ)	$1.379 \times 10^{-3}\ P$
4	Contact angle (θ)	80°
5	Porosity (ϵ)	0.5
6	Particle diameter (d)	$50\ \mu m$
7	Permiability (k)	$7 \times 10^{-12} m^4$

6.4 Results and Discussion

The models developed to simulate infiltration behaviour accounts for the fluid flow within the metal reservoir and the preform domain. Based on the way the two domains are treated and linked, three different modelling approaches were considered and examined for their relative merits. Finally, the selected model is assessed in terms of its ability to give physically realistic results and compared with data obtained from controlled laboratory experiments. The constants used in the present work are listed in Table 6.1.

MODEL 1. Enhanced viscosity model: It is a common practice to set a high pseudo-viscosity value for domains representing solids or two phase flow in hydro-dynamic models. In keeping with this principle, flow through a stationary porous preform is represented as a highly viscous flow. The Navier-Stoke's equation for fluid flow (Equations 6.17–6.19), along with the appropriate boundary conditions (Equations 6.22–6.25) are solved within the computational domain. For the grid points lying within the preform, μ is set to a large value ($\sim 12\ P$), so as to match experimental flow rates. The advantage of this model is its simplicity.

MODEL 2. Superimposed porous-media model: In this model, the Navier-Stoke's equation (Equations 6.17–6.19) is solved within the computational domain, treating the entire computational space to be molten metal (preform is absent). The preform condition is superimposed through the Darcy's equation at the end of each iteration. The grid point

velocities in the axial and radial direction within the preform are accordingly amended as:

$$u = -\frac{k}{\mu}\left(\frac{\Delta P}{\Delta x} - \rho g\right)$$ (6.32)

$$v = -\frac{k}{\mu}\left(\frac{\Delta P}{\Delta y}\right)$$ (6.33)

The calculated flow velocities within the preform domain are linked to the Navier-Stoke's equation through the pressure term. The advantage of this model over enhanced viscosity model is in its proximity to reality by way of incorporation of Darcy's equation.

MODEL 3. Modified momentum equation model: In this model, the momentum equation of the Navier-Stoke's equation (Equations 6.18–6.19) are modified to incorporate a resistance term due to the viscous drag experienced by the liquid flowing through narrow pore channels. This preform resistance term is incorporated in the preform domain of the axial and radial momentum equation, by modifying the S_u and S_v terms as:

$$S_u = \frac{3\pi(1-\epsilon)}{2d}\gamma_{lv}\cos\theta - \frac{\mu}{k}u$$ (6.34)

$$S_v = -\frac{\mu}{k}v$$ (6.35)

where the surface tension term is applicable only at the top surface layer control volumes. The advantage of this model is its elegance from the computational stand point. The Source term values for the three models are listed in Table 6.2

Table 6.2: Source terms of the three models considered.

MODEL	Name	S_u	S_v	Remarks
1	Enhanced viscosity model	$\frac{3\pi(1-\epsilon)}{2d}\gamma_{lv}\cos\theta$	$-$	$\mu = 12$ Poise within preform
2	Superimposed porous media model	$\frac{3\pi(1-\epsilon)}{2d}\gamma_{lv}\cos\theta$	$-$	Darcy's equation is coupled
3	Modified momuntum model	$\frac{3\pi(1-\epsilon)}{2d}\gamma_{lv}\cos\theta - \frac{\mu}{k}u$	$-\frac{\mu}{k}v$	$-$

6.4.1   Analysis of model results

Computational schemes for all three models were successfully implemented. Numerically predicted flow patterns indicate that the flow vectors in the domain were predominantly aligned along the axial direction. For a 50 *vol.%* void fraction within the preform ($\epsilon = 0.5$), the magnitude of the flow vectors within the preform was approximately twice that within the liquid metal reservoir. The rate of infiltration of metal (growth profile), as predicted by the three different models are compared in Figure 6.7. For a superficially enhanced viscosity value of 12 Poise within the preform domain, MODEL 1 could accurately predict the composite growth in the the early stages ($< 2000\ s$) of composite growth. Whereas, MODEL 2 resulted in an overestimate of infiltration heights beyond $\sim$2000 s. A performance comparison of the three models are given in Table 6.3. For a particular surface tension value, MODEL 3 could
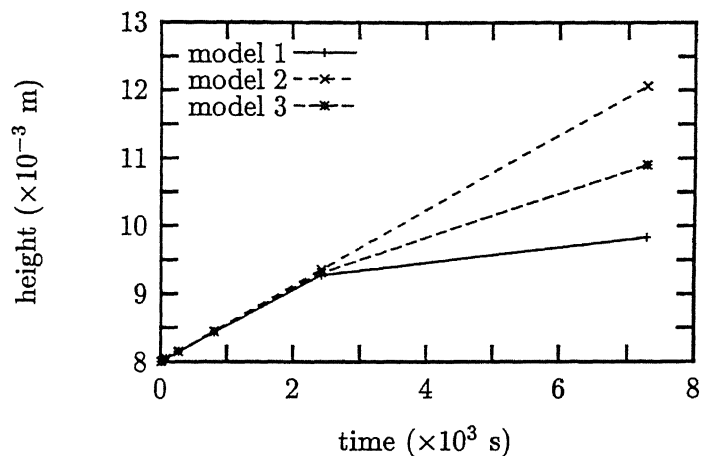
Figure 6.7: Infiltration profile comparison of the three models.

converge the fastest. For increasing values of surface tension, further under-relaxation was required for MODEL 1 and MODEL 2. This was achieved by increasing the value of 'α' in Equation 6.30, which in turn increased the number of iterations required for convergence. Variation in the surface tension and permeability value did not significantly affect the ability of MODEL 3 to converge. This is because the preform resistance force and the surface tension force appear within the axial momentum equation and effectively balance one another. On the other hand, they are linked through the pressure term in MODEL 2. Due to its faster convergence and relative numerical stability, the modified momentum model (MODEL 3) was selected for further analysis.

Table 6.3: Performance comparison of the three models.

Sr. No.	Criteria	Model 1	Model 2	Model 3
1	Convergence criteria (residual mass) $[kg/m^3]$	10^{-17}	10^{-15}	10^{-15}
2	No. iterations for convergence	~ 2000	~ 3000	~ 800
3	Max. ST force/m^2 before divergence occurred $[N/m^3]$	$\sim 10^2$	~ 10	$> 10^4$
4	Viscosity within preform, μ $[P]$	12	1.3x10^{-3}	1.3x10^{-3}
5	Preform permiability, k $[m^3]$	–	7×10^{-12}	7×10^{-12}

6.4.2 Model sensitivity tests

Having chosen the modified momentum model, the following tests were carried out to establish its computational stability of the model and reliability of the results.

TEST 1. Sensitivity to Preform depth immersed in Liquid: To verify the initial wetting hypothesis (Assumption No. 6), computations were repeated increasing the number of grids in the axial direction that were assumed to be immersed in the liquid alloy. With increasing number of grids immersed in the liquid, computationally it was observed that the initial infiltration rate decreases (Figure 6.8). This can be explained since the effective preform resistance to infiltration is greater with increasing depth, while the surface tension remains constant. The velocity of the infiltration front was found to stabilize to a constant value after ~ 2000 s.

TEST 2. Sensitivity to grid size distribution: So far, the results were obtained using a (17×12) grid system. To assess the influence of grid size on computation, additional grid configurations, (9×12) and (32×12) were tested. The resulting infiltration profiles are shown in Figure 6.9. An 8% increase in height for the finer grid and a 7% decrease in height for the coarser grid with respect to the (17×12) grid system are obtained. This difference arises because the surface tension force (which is acting only on the surface control volume) is balanced against a smaller preform resistance in case of the finer grid and *vice versa*. Here
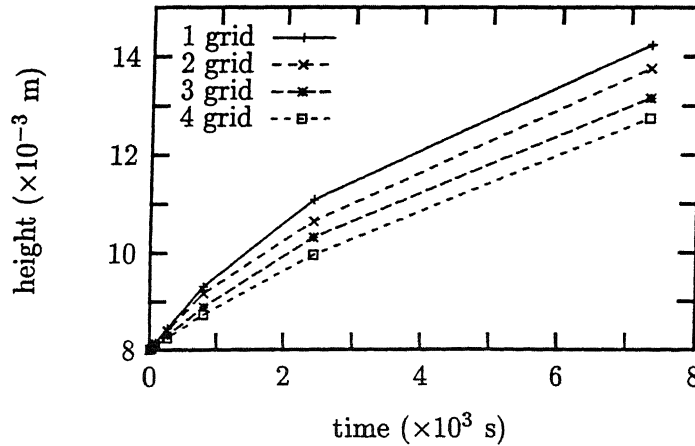
Figure 6.8: Infiltration profiles with increasing number of grids initially immersed in the metal.

again, the infiltration rate stabilizes to a constant value.
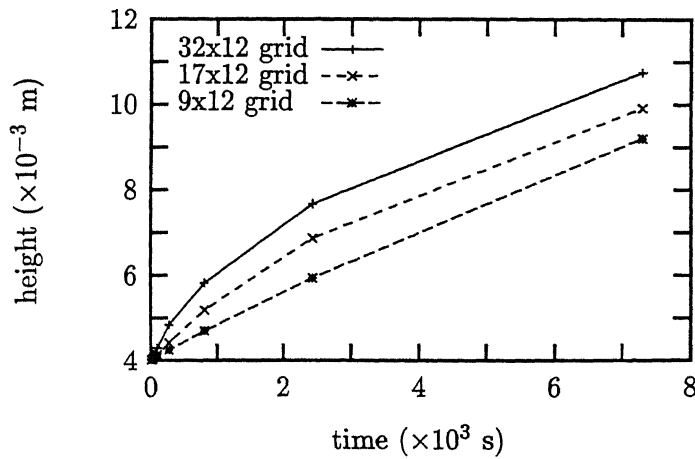
Figure 6.9: Infiltration profiles with varying grid spacings in the axial direction.

TEST 3. Sensitivity to time step factor: The unsteady state flow equations were solved by marching forward in time using a fully implicit numerical scheme. Consequently, the predicted results are expected to depend time step, Δt. In the present study, time step size was chosen in accordance with a geometric series (Equation 6.27). Figure 6.10 shows the infiltration profiles for various values of r. The infiltration profiles show no significant variation in growth kinetics for $r = 2$, 3 and 4. Therefore, the predicted results can be assumed to be independent of step height within the range applied.

Figure 6.10: Infiltration profiles with variation in time step factor.
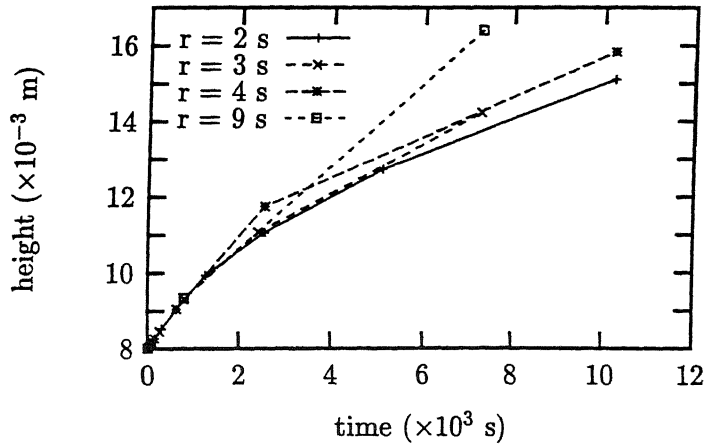
6.4.3 Sensitivity of predicted results to process parameters

Having established the sensitivity of the model, it is important to establish its reliability in predicting experimental results. For this purpose three different cases are examined and qualitatively compared with available experimental results. In examining these cases, a 17×12 grid with a time step factor of $r = 3$ is employed. These cases are described below in detail.

CASE 1. Packing fraction: It is possible to vary the packing fraction of the preform for a given powder particle size, by increasing the compaction pressure or prolonging the sintering schedule. 'Infiltration profiles for three void fractions, $\epsilon = 0.45$, 0.5 and 0.55 are shown in Figure 6.11. A variation in ϵ alters the surface tension force and preform permeability k, according to Equation 6.29 and 6.20, respectively. The model predicts a faster infiltration for the more permeable preform, which is in accordance with expectation and predictions by the capillary-bundle model [14].

CASE 2. Particle size: Varying the particulate size while maintaining the packing fraction constant is another possibility. Infiltration profiles for particulate diameters of 40, 50 and 60 μm are shown in Figure 6.12. With increasing particle size for a constant void fraction, the preform becomes more permeable and the infiltration rate is enhanced. This trend in results is again consistent with predictions by the capillary-bundle model and experimental
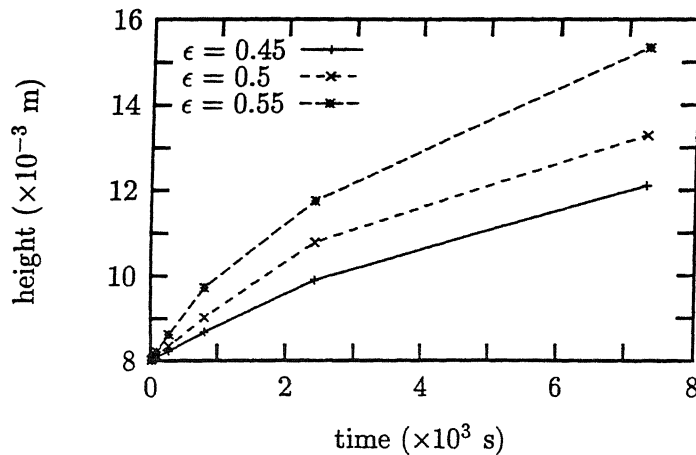
Figure 6.11: Infiltration profiles with variation in preform pore fraction.

observation in AlN particulate preform [15]. On the other hand, Aghajanian *et al.* [25] have reported the opposite behaviour for infiltration in fused Al_2O_3 preforms. It is possible that the spinel layer formation at the metal–ceramic interface is infiltration rate controlling. In which case, the surface area available for reaction increases with decrease in particulate size, augmenting infiltration.
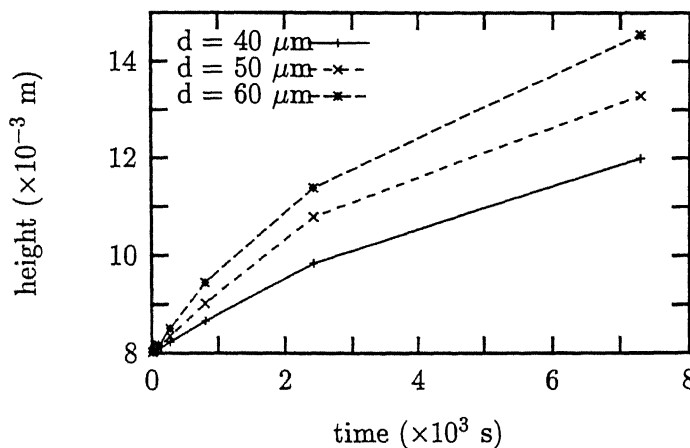
Figure 6.12: Infiltration profiles with variation in preform particulate size.

Recently, Tai *et al.* [26] have by visual means obtained the profiles of Borosilicate aided Al_2O_3 preform infiltration as a function of time (Figure 6.13). The application of a layer of Borosilicate almost entirely eliminates the incubation period and accelerated growth rates are obtained. The seemingly linear nature of infiltration profiles is probably because of the
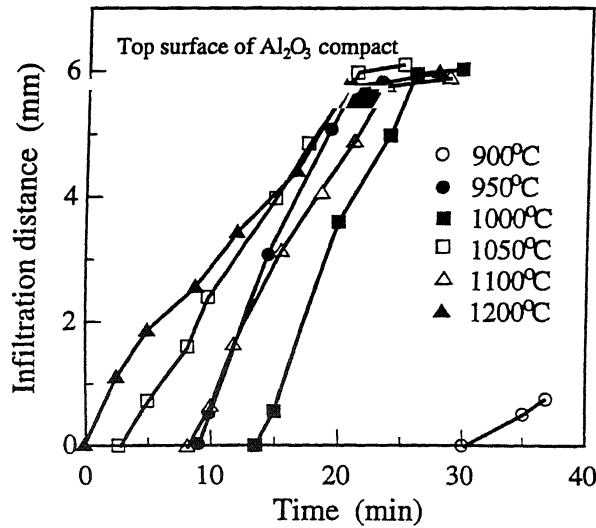
Figure 6.13: Infiltration profiles of Borosilicate aided aluminum infiltration through Al$_2$O$_3$ preform at different temperatures[26].

very short duration of infiltration observed.

CASE 3. Temperature: Temperature influences several process parameters. In this section, the effect of temperature on surface tension is studied in isolation. In the previous chapter on infiltration, an activation energy of 25 kJ/mol was obtained for infiltration through SiC preforms. This low value suggests a physical phenomena, such as surface tension or viscosity as rate controlling. To verify this, infiltration profiles for various surface tension values in the temperature range 900–1100$^o C$ were numerically computed. The value of γ_{l_v} corresponding to different process temperature was computed from Equation 6.28. The corresponding change in contact angle was estimated by the empirical relation developed by Asthana [27]:

$$\gamma_{l_v} \cos \theta = -0.001627 \gamma_{l_v}^2 + 1.7886 \gamma_{l_v} - 797.49 \qquad (6.36)$$

An activation energy of 18 kJ/mol is calculated for a surface tension dominant infiltration system (Figure 6.14). This value compares well with the experimentally obtained value, suggesting that the surface tension force is infiltration rate controlling.
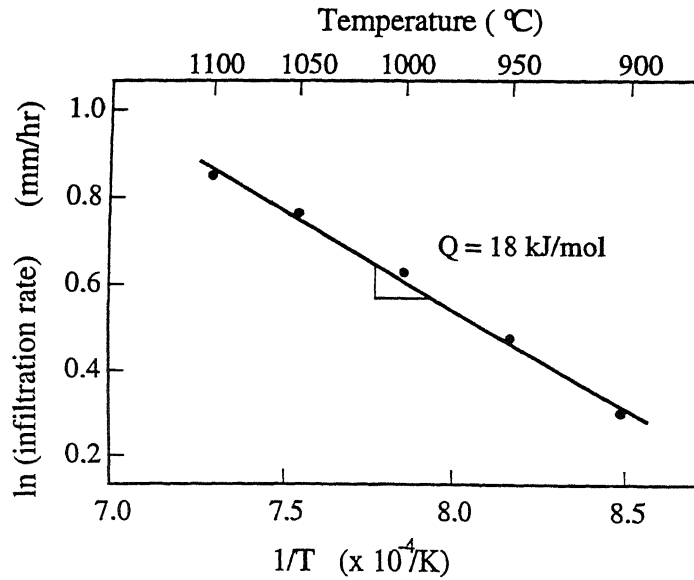
Figure 6.14: Computationally estimated Activation energy calculation for a surface tension dominant system.

6.5 Summary

Until recently, the mathematical modelling of metal infiltration have approximated the flow through through porous preforms to a flow through a bundle of capillary tubes. In contrast, for the first time, a flow through porous-bed approach, combining Navier–Stoke's and Darcy's equation has been applied. To this end, a transient, 2-dimensional, laminar flow model in cylindrical polar co-ordinate system was developed to simulate the flow behaviour. The aim of the theoretical model was to predict the overall growth of composite from a knowledge of the flow phenomenon.

Three different modelling approaches, based on an implicit scheme were considered and implemented in the numerical solution scheme to simulate the porous-bed phenomenon. This included, (1) Enhanced viscosity model, (2) Superimposed porous media model and (3) Modified momentum model. For a superficial viscosity value of 12 Poise within the preform domain, Model 1 could accurately simulate the infiltration phenomenon during the early stages of composite growth. On the contrary, Model 2 predicted an overestimate of infiltration heights beyond ~2000 seconds. The permeability of the porous preform for the

present experimental conditions was estimated to be $\sim 7\mathrm{x}10^{-12}m^2$. Of the three types o modelling approaches considered, the modified momentum model was preferred due to its faster convergence and relative numerical stability.

To validate the model, sensitivity of infiltration height predictions to various numerical approximations, such as initial preform immersion depth, grid size distribution and time step factor were numerically verified. To establish the reliability of the model, the sensitivity of predicted results to certain process parameters were examined. Infiltration through preforms of different packing fraction and particulate size were numerically evaluated. The trend in the results predicted by the modified momentum model were in accordance with predictions of the capillary bundle model and experimental observations reported in the literature. The computationally estimated surface tension dependent activation energy for infiltration of 18 kJ/mol is comparable to the experimentally determined value of 25 kJ/mol for SiC infiltration.

References

[1] M. S. Newkirk, A. W. Urquhart, H. R. Zwicker and E. Breval, Formation of Lanxide ceramic composite materials, *J. Mater. Res.*, **1** (1986) 81–89.

[2] D. K. Creber, S. D. Poste, M. K. Aghajanian and T. D. Claar, AlN composite growth by nitridation of aluminum alloys, *Ceram. Eng. Sci. Proc.*, **9** (1988) 975–982.

[3] T. Young. *Trans. Roy. Soc.*, **95** (1805) 65.

[4] L. Ackermann, J. Charbonnier, G. Desplanches and H. Koslowski, *5th Int. Conf. on Comp. Mater.*, San Diego, CA, TMS, Warrendale, PA, U.S.A., (1995) 687–698.

[5] T. W. Clyne, M. G. Bader, G. R. Cappleman and P. A. Hubert, The use of δ–Al_2O_3 fibre for metal-matrix composites, *J. Mater. Sci.*, **20** (1985), 85–96.

[6] F. M. Hosking and A. A. Netz, Liquid metal infiltration of an aluminum alloy into a packed column of B, C particles, Research report no. SAND-83-2573, Sandia National Laboratory, Albuquerque, NM, U.S.A., (1984).

[7] P. B. Maxwell, G. P. Martins, D. L. Olson and G. R. Edwards, The infiltration of aluminum into Silicon Carbide compacts, *Met. Trans.*, **21B** (1990) 475–485.

[8] E. W. Washburn, *J. Phys. Rev.*, **17** (1921), 273–283.

[9] R. Von Mises and R. O. Fredricks, *Fluid dynamics*, Springer-Verlag, New York, U.S.A. (1971).

[10] P. C. Hiemenz, *Principles of colloid and surface Chemistry*, 2nd ed., Marcel Deckker Inc., New York, U.S.A. (1986), 302.

[11] W. E. Britten, Liquid rise in a capillary tube, *J. Appl. Phy.*, **17** (1946) 37–44.

[12] J. R. Ligenza and R. B. Bernstein, The rate of rise of liquids in fine vertical capillaries, *J. Am. Chem. Soc.*, **73** (1951) 4636–4638.

[13] K. A. Semlak and F. N. Rhines, Rate of infiltration of metals, *AIME Trans.*, **21** (1958) 324–331.

[14] W. B. Hillig, Melt infiltration approach to ceramic matrix composites, *J. Am. Ceram. Soc.*, **71** (1988) C96–C99.

[15] C. Toy, Ceramic-metal composites produced by melt infiltration, *J. Am. Ceram. Soc.*, **73** (1990) 97–101.

[16] D. Muscat, and R. A. L. Drew, Modelling the infiltration of molten aluminum into porous titanium carbide, *Metall. Trans.*, **25A** (1994) 2357–2370.

[17] G. P. Martins, D. L. Olson and G. R. Edwards, Modelling of infiltration kinetics for liquid metal processing of composites, *Metall. Trans.*, **19B** (1988) 95–101.

[18] H. Darcy, Les Fontaines Publiques de la Ville de Dijon, Dalmont, Paris, (1856).

[19] A. E. Scheiddegger, *The physics of flow through porous media*, University of Toront press, Toronto, Canada, (1974).

[20] M. Reza Aboutalebi, M. Hasan and R. I. L. Guthrie, Coupled turbulent flow, heat and solute transport in continuous casting process, *Metall. Trans.*, **26**B (1995) 731–744.

[21] S. Minakawa, I. V. Samarasekera and F. Weinberg, Centerline porosity in plate castings, *Metall. Trans.*, **16**B (1988) 823–829.

[22] S. V. Patankar and D. B. Spalding, A calculation procedure for heat, mass and momentum transfer in three-dimensional parabolic flows, *Int. J. Heat Mass Transfer*, **15** (1972) 1787–1792.

[23] S. R. Rhee, Wetting of Ceramics by liquid Al, *J. Am. Ceram. Soc*, **53** (1970) 386–390.

[24] S. V. Patankar, *Numerical Heat Transfer and Fluid Flow*, Hemisphere, New York, U.S.A. (1980) 102.

[25] M. K. Aghajanian, M. A. Rocazella, J. T. Burke and S. D. Keck, J. Mater. Sci., **26**, (1991), 447–454.

[26] W.-P. Tai, T. Watari and T. Torikai, Fabrication of Al_2O_3–Al composites by reacted melt infiltration, *Am. Ceram. Soc. Bull.*, **76** (1997) 86–89.

[27] R. Asthana, An empirical correlation between contact angle and surface tension in some ceramic–metal systems, *Metall. Mater. Trans.*, **25**A (1994) 225–230.

Chapter 7

Conclusions

Based on the present study on processing, mechanical property and mathematical modelling aspects of melt infiltrated composites the following conclusions ensue.

1. The microstructural development during nitridation of binary alloys (i.e. Al–Mg, Al–Zn, Al–Si, Al–Na) is limited to the formation of a passivating surface nitride layer with no composite formation. On the other hand, several Al–Si–Mg alloys, particularly those with a high Mg/Si ratio consistently form bulk nitrided composites with an interconnected AlN/Al network.

2. The processing variables that are critical to nitride formation are the Mg/Si ratio, Oxygen partial pressure and processing temperature. By varying the alloy composition and process temperature, four different nitridation reaction mechanisms are identified. They are: (i) passivating surface nitride layer with no internal nitridation, (ii) predominantly surface nitride formation with diffusion controlled volume nitridation, (iii) bulk nitridation with extensive outward AlN/Al composite development and (iv) break-away nitridation with complete conversion to AlN.

3. The role of Mg and Si solute atoms on the nitridation of aluminum alloys are multifold. Mg serves as an Oxygen getter and improves wettability by promoting interfacial reactions. Small amounts of Si, along with Mg, improves the nitridation kinetics and alters the reaction mechanism to one of bulk composite formation. On the contrary, Si in

large quantities affects nitridation by decreasing the diffusivity and possibly solubility of Nitrogen in the alloy.

4. During nitridation of aluminum alloys, AlN having the wurtzite-type (hexagonal) structure is known to be the stable phase for reactions occurring at atmospheric pressure. For the first time in the present work, due to the combined influence of Mg and Zn in the case of Al–2Si–4Mg–4Zn alloy, AlN of the Sphalerite and NaCl-type cubic structures is found to be stable.

5. Among the Al–Si–Mg alloys examined, Al–2Si–8Mg alloy optimally combined both nitridation kinetics and infiltration rate of porous SiC preforms to produce nearly dense SiC/AlN/Al composites.

6. Infiltration through various SiC (particulate, platelet, short fibre and fibre) preforms was successfully demonstrated. In comparison to alloy nitridation, the improved conversion to AlN during infiltration is attributed to the reinforcement particle surface acting as sites for nucleation. The significance of surface chemistry is demonstrated by the nitridation behaviour in Nicalon and AVCO SiC fibres. The absence of nucleation of AlN on AVCO SVS–6 monofilaments is attributed to the presence of a C-rich surface layer.

7. In the case of SiC particulate preforms, the infiltration kinetics improves with increase in reinforcement particle size and process temperature. The residual porosity decrease with decrease in particle size. An activation energy of 25 kJ/mol is obtained for infiltration, which corresponds to a physical phenomenon, such as surface tension force, as rate controlling.

8. The lack of property improvement in fibre reinforced composites is attributed to fibre weakening caused by long exposure at high reaction temperatures. Maximum flexural and fracture toughness values of 250 MPa and 7.0 $MPa\sqrt{m}$, respectively, are measured for SiC particulate reinforced composites processed at 950^oC. The decrease in properties with increase in particulate size and process temperature observed in SiC

reinforced composites is a consequence of increase in porosity level. The environmenta degradation of the composite can be avoided by prior coating of particulates.

9. To eliminate the residual aluminum, infiltration through intermetallic preform was attempted. Reactive infiltration of Nickel aluminide preforms facilitates faster infiltration rates at temperatures as low as $750^\circ C$. Microstructure of infiltrated composites revealed interaction of Al with intermetallic particles forming intermediate phases by dissolution and reprecipitation reactions. The catalytic influence of Ni, along with the exothermic heat generated by intermetallic reactions causes an improved conversion of Al to AlN.

10. Retention of reinforcement particle morphology and a larger volume fraction of the high temperature intermetallic (Ni_2Al_3) phase, along with increased AlN formation leads to improved mechanical properties for composites processed at lower temperatures. Best flexural strength and fracture toughness values of 255 MPa and 10.35 $MPa\sqrt{m}$, respectively, are obtained for composites processed at $750^\circ C$.

11. A mathematical fluid flow model, based on flow through porous-bed phenomenon was developed in the 2-dimensional cylindrical polar coordinate system. Three different approaches were considered and numerically implemented to predict the composite growth behaviour. They include, (i) Enhanced viscosity model, (ii) Superimposed porous media model and (iii) Modified momentum model. It is shown that by artificially enhancing the viscosity (to about 12 Poise) the porous-bed phenomena can be realistically simulated. Of the three types of approaches considered, the modified momentum model was preferred due to its faster convergence and relative numerical stability.

12. The results predicted by the modified momentum model for variation in packing fraction and particle size was found to be physically realistic and consistent with experimental observations. The numerically estimated activation energy of 18 kJ/mol for a surface tension force dominant preform infiltration, is comparable to the experimentally obtained value.

Chapter 8

Scope for further work

In light of the present work, the following areas are of interest for further study.

1. Favourable wetting of the preform by the infiltrant is an essential criteria for pressureless infiltration. At present there is a dearth of contact angle data for various aluminum alloy/preform material combinations as a function of temperature in Nitrogen atmosphere. For qualitative comparison of infiltration rates in various systems, additional experimental work to estimate thermophysical constants, such as viscosity, surface tension, etc. is essential.

2. Prolonged holding at processing temperatures lead to both beneficial and undesired reinforcement/matrix interfacial reactions. In the case of SiC reinforcement, while the silica layer on SiC aids wetting, formation of moisture sensitive Al_4C_3 leads to progressive deterioration of mechanical properties. For this reason, it is necessary to further explore possible ways to suppress or altogether eliminate undesirable reactions.

3. The residual aluminum retained within the matrix limits the high-temperature applicability of these composites. In the present study, it is shown that the aluminum can be converted to a high-temperature phase by infiltrating through an intermetallic preform. It is further reasoned that by a judicious mix of SiC and Nickel aluminide or Nickel within the preform, aluminum can be eliminated from the composite. Furthermore, it is desirable to study the high-temperature mechanical behaviour of such

a composite and compare with conventional high-temperature materials.

4. The mathematical model developed in the present study, based on the flow through porous bed phenomenon, simulates the infiltration behaviour for variation in preform particle size and packing fraction. Further development is required to take into account additional factors, such as the interfacial reactions, AlN formation and transient wetting behaviour. Additionally, the influence of alloy composition, temperature and reaction gas composition on infiltration kinetics is yet to be modelled.

Appendix A

Calculation of Perimeter length

Let us assume that the randomly packed preform particulates have a uniform radius, R and a pore fraction of *epsilon*. The probability of finding a circle of radius r; $0 \leq r \leq R$, in a sphere of radius R is given as:

$$N(r) = \frac{r}{R\sqrt{R^2 - r^2}} \tag{A.1}$$

In a random cross-section of the preform, the area fraction occupied by the preform particulates may be expressed as:

$$C \int_0^R \frac{r}{R\sqrt{R^2 - r^2}} \pi r^2 dr = (1 - \epsilon) \tag{A.2}$$

where C is the scaling factor. On intergrating and applying the limits,

$$C = \frac{3}{2} \frac{(1 - \epsilon)}{\pi R^2} \tag{A.3}$$

Then, the length of the particulate perimeter per unit cross-sectional area (P) of the preform can be calculated as:

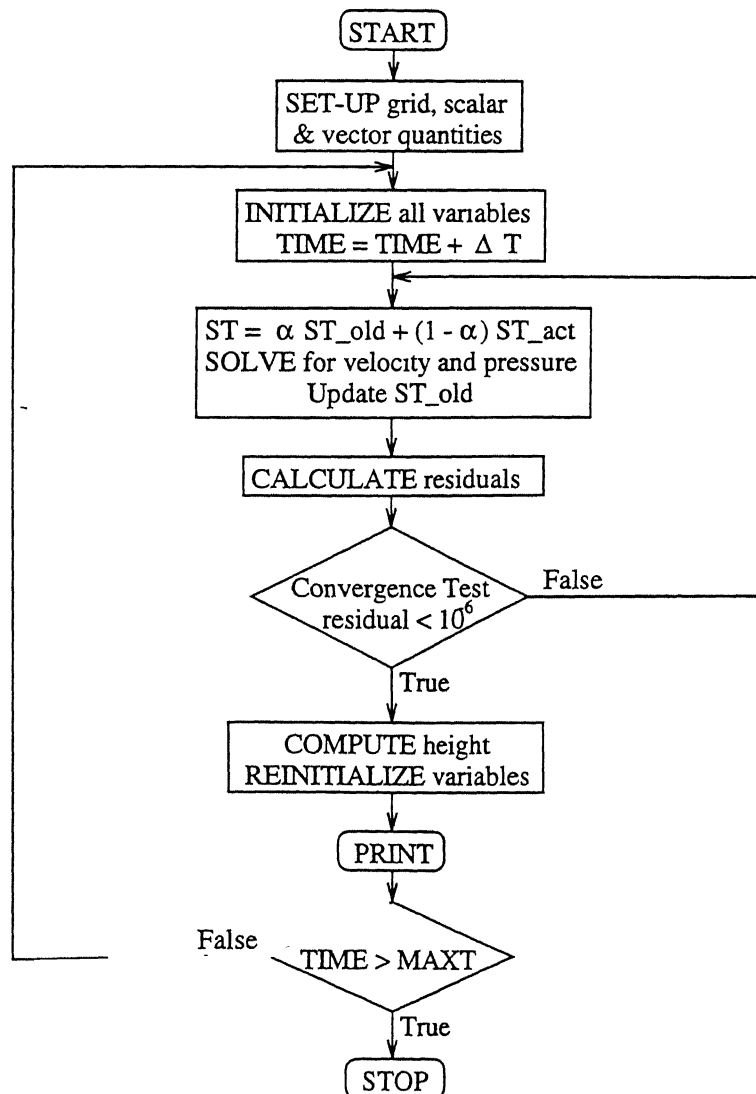$$P = C \int_0^R \frac{r}{R\sqrt{R^2 - r^2}} 2\pi r dr \tag{A.4}$$

On intergrating and applying the limits for r, and substituting $2R = d$, where d is the particle diameter,

$$P = \frac{3\pi}{2} \frac{(1 - \epsilon)}{d} \tag{A.5}$$

P is expressed in units of m^{-1}.

Appendix B

Flow diagram of computer model

List of Publications in Journals

1. Directed melt oxidation and nitridation of alloys: a comparison

   B.S.S.Daniel and V.S.R.Murthy, *Materials & Design* **16**[3] (1995) 155-161.

2. Metal matrix composites via insitu methods

   B.S.S.Daniel, V.S.R.Murthy and G.S.Murty, *Journal of Materials Processing Technology* (In press)

3. Microstructure and mechanical properties of SiC reinforced AlN/Al composites

   B.S.S.Daniel, V.S.R.Murthy and G.S.Murty, *ISIJ International* **37**[10] (1997).

4. Pressureless infiltration of Nickel Aluminide reinforced AlN/Al composites

   B.S.S.Daniel, V.S.R.Murthy and G.S.Murty, *Journal of Materials Science* (in preparation)

5. Mathematical modelling of Presureless Infiltration phenomenon

   B.S.S.Daniel, D.Mazumdar and V.S.R.Murthy, *Metallurgical Transactions B* (in preparation)

List of Publications in Conferences Proceedings

6. Microstructure and mechanical properties of directed melt nitridation composites

   B.S.S.Daniel, V.S.R.Murthy and G.S.Murty, MRSI Symposium, IIT Kharagpur, Feb. 1994.

7. Intermetallic reinforced AlN/Al composites

   B.S.S.Daniel, V.S.R.Murthy and ˙G.S.Murty, ADCOMP-'96, IISc, Bangalore, Dec. 1996.

8. Mathematical modelling of Infiltration phenomena through a porous ceramic preform

   B.S.S.Daniel, D.Mazumdar and V.S.R.Murthy, ICRAMP-'97, IISc, Bangalore, July 1997.

Date Slip

This book is to be returned on the
date last stamped.

MME- 1997-D- DAN- PRC